

University of Utrecht

Master Thesis

Space Weather Impact

The development of an ionospheric
electron density model for impact
assessment of Space Weather

Author:
Ing. D.R. (Damon) Peperkamp

Supervisor:
Ir. L. (Linda) Van der Ham
Ir. H. (Hester) Vermeiden
Dr. Ir. B. (Bert) Wouters

A thesis submitted in fulfillment of the requirements
for the Master degree in Climate Physics
at the Faculty of Science, Department of Physics

v2019 WP3 060.40580
Space Situational Awareness
Ministry of Defence
Military Operations | TNO

Military Operations | TNO

Oude Waalsdorperweg 9
2597 AK The Hague, NL
P.O. Box 96864
2509 JG The Hague, NL
+31 88 866 1000

Thesis

The development of an ionospheric electron density model
for impact assessment of Space Weather

Date	📅 September 9, 2021
Author	Ing. D.R. (Damon) Peperkamp Institute for Marine and Atmospheric Research (IMAU) 🏛️ Utrecht University
Supervisor(s)	Ir. L. (Linda) Van der Ham Military Operations TNO Ir. H. (Hester) Vermeiden Military Operations TNO Dr. Ir. B. (Bert) Wouters Institute for Marine and Atmospheric Research (IMAU) 🏛️ Utrecht University

nr. of pages	(incl. appendices)
nr. of appendices	-
Customer	Ministry of Defence
Project name	v2019 WP3 Space Situational Awareness
Project number	060.40580

All rights reserved.

No part of this publication may be reproduced and/or published by print, photoprint, microfilm or any other means without the previous written consent of TNO.

In case this report was drafted on instructions, the rights and obligations of contracting parties are subject to either the General Terms and Conditions for commissions to TNO, or the relevant agreement concluded between the contracting parties. Submitting the report for inspection to parties who have a direct interest is permitted.


If this report is issued, for the rights and obligations of client and contractor please refer to the General Conditions for TNO contracts, or the relevant agreement signed between the parties. It is permitted to give this TNO report to direct stakeholders for inspection.

©2021 Copyright TNO

Damon Peperkamp © 2021

The development of an ionospheric electron density model for impact assessment
of Space Weather


Institute for Marine and Atmospheric Research (IMAU)

 Utrecht University

Faculty of Science | Department of Physics

Princetonplein 5


3584 CC Utrecht

 The Netherlands

PO Box 80000


3508 TA Utrecht


 The Netherlands


 +31 (0)30 253 3284

 science.secretariat.phys@uu.nl


Supervisor(s):

 Ir. L. (Linda) Van der Ham

 Ir. H. (Hester) Vermeiden

 Dr. Ir. B. (Bert) Wouters

Location / time frame:

 March 2020 - January 2021

Acknowledgements

This thesis is dedicated to
my beloved mother, Christa Peperkamp,
my caring and loving partner, Marjolein Leijenhorst,
an observing saviour, Yo-Yi Pat.

Damon Peperkamp

Contents

Abstract	xi
Samenvatting	xiii
Acronyms	xv
chemistry	xvii
Symbols	xviii
Numbers	xxi
1 Introduction	1
1.1 Motivation – – – – –	2
1.2 Research Objective – – – – –	2
1.3 Outline of this thesis – – – – –	3
2 The atmosphere	4
2.1 Introduction to the atmosphere – – – – –	5
2.2 Atmospheric profile – – – – –	7
2.3 Atmospheric processes – – – – –	9
Summary of this chapter – – – – –	15
3 Radio waves	16
3.1 An introduction to radio waves – – – – –	17
3.2 Atmospheric effects on radio waves – – – – –	17
3.3 Ionospheric Forecast – – – – –	21
3.4 Quantifying disturbed radio waves – – – – –	22
3.5 Electron density variation – – – – –	24
Summary of this chapter – – – – –	28
4 Space Weather	29
4.1 Space Weather Events – – – – –	30
4.2 Effect of Space Weather Events – – – – –	32
4.3 Morphology of the Magnetosphere – – – – –	33
4.4 The origin of Space Weather Events – – – – –	35
Summary of this chapter – – – – –	38

5	Electron Density Model	39
5.1	Introduction of the model	40
5.2	General equations of the model	41
5.3	Dynamics of the model	43
5.4	Overview of other models	48
	Summary of this chapter	49
6	Results	50
6.1	Model results	51
6.2	Measurement data in Mali	58
6.3	Atmospheric effects on radio waves	64
	Summary of this chapter	66
7	Conclusions and recommendations	68
7.1	Reflecting on the objectives	69
7.2	Summary of findings	69
7.3	Recommendations for further research	71

Appendices

A Chemical reactions

B Photo ionization Cross sections

B.1	Matlab output figures	79
-----	-----------------------	----

C NOAA Scales

Bibliography

List of Figures

1.1	Artistic impression of Situational Space	1
2.1	Schematic of phenomena occurring in the ionosphere	4
2.2	Indicative figure of Single layer model for ground and space users	5
2.3	Structure profiles of the atmosphere	8
2.4	Distribution of atmospheric atoms and molecules	9
2.5	Production and loss of electrons in the ionosphere	9
2.6	Solar radiation depth as function of wavelength for Ionisation processes	12
2.7	Illustration showing the law of Ohm and Faraday	14
3.1	Examples of radio waves entering the ionosphere and being affected	16
3.2	Illustration of radio waves propagating in the ionosphere	19
3.3	Schematic of a Single Ionospheric Layer Geometry	22
3.4	Ionospheric structure and Electron Density Profile	25
3.5	The regions of geomagnetic latitude	25
3.6	Schematic showing the Dynamo Electric Field.	26
3.7	Trapped ion and electrons by the Geomagnetic field	27
3.8	Schematic showing the spread F	28
4.1	Impression of atmospheric processes	29
4.2	Global Signal fading due to scintillation in L band	32
4.3	Schematic showing a cross section of the Magnetosphere	33
4.4	Schematic of Earth's Magnetosphere	35
5.1	Schematic of the used Ionospheric ray tracing	39
6.1	NRLMSISE-00 atmosphere Model	51
6.2	Vertical distribution of modelled temperature of neutrals, ions and electrons	52
6.3	Model output of the proxy representable for the Solar Radio Flux Index	53
6.4	Ionization rate of ion species, as input for the Solar irradiance	54
6.5	Electron-impact cross section as function of temperature	55
6.6	Modelled Solar irradiance, or Solar Photon Flux	55
6.7	This figure shows the atmospheric species	56
6.8	This figure shows the ionized atmospheric species	57

6.9	This figure shows data of GPS satellite signals. It contains the S4, lock-time, azimuth angle, and elevation angle. Measurements where done at week number 1877 and time of week 345660 seconds. - - - - -	61
6.10	This figure shows data of GPS satellite signals. Measurements where done at week number 1877 and time of week 345660 seconds. - - - - -	62
6.11	Polar plot of the azimuth and elevation angle - - - - -	63
6.12	Analysis of TEC - - - - -	63
6.13	Absorption of the lower Thermosphere - - - - -	64
6.14	Modelled Ionospheric layers - - - - -	65
6.15	This figure shows the Ionospheric layer - - - - -	66
6.16	This figure shows the daily variation of the usable frequency - - -	67

List of Tables

5.1	Recombination rates, as input for the ionization balance	43
5.3	Overview of existing electron density models	48
6.1	Table shows the format of the output blocks of the Sceptentrio receiver	60
6.3	Table of satellite Carrier frequency	60

Abstract

This thesis facilitates an understanding of Space Weather and how the corresponding phenomena affect propagating radio waves. Focus lies on the applications (Military) Satellite Communication and positioning, navigation and timing. Measurement error occurs between Earth's surface and Ionosphere. Radiation and charged particles, emitted by the Sun, are causing continuous stress on Earth's atmosphere. The geomagnetic field is holding back the highly-energetic Solar Wind and is constant battle simultaneously against Space Weather Phenomena e.g. Coronal Mass Ejections, Geomagnetic storms and sub-storms. The objective of this thesis might be of (military) interest, as the results are used to assess the possibility of using local Scintillation measurements in a (short-term) forecast of atmospheric disturbances.

In the procedure to quantify the order of disturbance, multiple steps are required. Simplifying first, using geometric approach of lower Thermosphere layer for the first 80 km. And at least one Ionospheric layer, covering the D-layer 80 km to 100 km, E-layer 110 km to 130 km, F1-layer 130 km to 200 km, and the F2-layer 200 km to 400 km. A propagating radio wave through these layers would be absorbed and converted into heat via particle collision. Higher in the atmosphere starting around 80 km, the receiver image is distorted by a sharp density increase of charged particles. This second effect results from the different refraction index of the atmospheric layers, as the radio waves are bent slightly different, separating the radio wave in two frequency-dependent waves. This is named dispersion and results in a Phase advance and Group delay. However this can be corrected by dual frequency receivers. The third effect, Faraday Rotation, results from radio waves entering the anisotropic Ionosphere, taking into account some plasma physics. The two resulting radio waves are oriented by the direction of propagation and Earth's magnetic field, an ordinary (*O*) and extraordinary wave (*X*). These three effects were found to be expressible as the Appleton-Hartree equation, found by Sir Edward Appleton (Nobel prize, 1950).

To facilitate and solve the Appleton-Hartree equation, key input is the characterization of electron density. This was approached with an Electron Density model. The Electron Density varies on vertical, latitudinal, and temporal scale. Main ionization source is the Sun, as the Solar Wind contains impact atmospheric species by ionizing species. Main losses are recombination of charged and neutral species and diffusion. In addition, losses are plasma transport due to atmospheric winds and interaction with the geomagnetic field. In this thesis higher order Ionospheric effects are present, resulting in more radio wave disturbances, described

by Scintillation, Phase instability, and Decoherence. This can be summarized as varying Ionospheric electrons, as they are being produced, lost, and transported. And these are the same electrons which quantify radio wave disturbances.

When Earth is viewed from a different perspective, its atmosphere is largely characterized by specific behaviour, bound to temporal or latitudinal variations. Two examples are the Aurora (a spontaneous emission of wavelength-specific plasma of the Polar region), and the Equatorial fountain close to Earth's magnetic equator. Particular waves can be found at specific phenomena, as the source would be measurable by e.g. Plasma frequency or Cyclotron frequency. These waves are categorized and are the result of Space Weather. Connection between earlier described Ionospheric variations in Electron density could be observed, or predicted by geomagnetic pulsations of the Magnetosphere. Geomagnetic pulsations are caused by Space Weather, and result in Ionospheric variations. The Ionospheric variations are causing the disturbed radio waves we are originally interested in.

Goal of the project this thesis was a component to answer if there is a possibility of using local measurements in a forecast scheme, to forecast the effect of Space Weather on Satellite communication signals.

Keywords: Space Weather Impact (SWI), Space Situational Awareness (SSA) (SSA), Magnetohydrodynamics (MHD), Radio Wave Propagation, Total Electron Content (TEC), Ionospheric layer approximation

Samenvatting

Dit onderzoek draagt bij aan het begrip van weersomstandigheden in de ruimte en hoe gerelateerde fenomenen invloed hebben op radio golven. Aandacht ligt met name op de toepassing van (militaire) Satelliet Communicatie, positie, navigatie en tijdsbepaling. Meetfouten ontstaan tussen het aardoppervlak en de Ionosfeer. De straling en geladen deeltjes, afkomstig van de zon, zorgen voor een continue belasting van de atmosfeer van de aarde. Het geomagnetisch veld houdt de hoogenergetische zonnewind tegen en is constant in strijd met de weersomstandigheden in de ruimte. Bijvoorbeeld Coronaal Massa Ejecties, Geomagnetische stormen en sub stormen. Het doel van dit onderzoek is deels van militaire aard, aangezien het resultaat daar gebruikt kan worden. Namelijk bij het beantwoorden van de mogelijkheid van het gebruik van scintillatie metingen in een korte termijn voorspelling van atmosferische verstoringen.

In de procedure om de verstoringen te kwantificeren, zijn meerdere stappen benodigd. Ten eerste, een simplificatie, met gebruik van een geometrische benadering van de lagere Thermosfeer voor de eerste 80 km en ten minste een Ionosferische laag, namelijk de D-laag 80 – 110 km, E-laag 110 – 130 km, F1-laag 130 – 200 km en de F2-laag 200 – 400 km. Een radio golf die zich door deze lagen voortplant zal worden geabsorbeerd en omgezet worden in warmte door het botsen op deeltjes. Hoger in de atmosfeer (beginnend rond de 80 km), is het beeld van de ontvanger verstoord door een verandering van de concentratie geladen deeltjes. Dit tweede effect ontstaat door een verschil in de refractie index van de atmosferische lagen. Dit komt doordat de radio golven anders afgebogen worden. De radio golven splitsen zich in twee frequentie afhankelijke golven. Dit effect wordt dispersie genoemd en resulteert in een vooruitgang en vertraging van de fase en groep. Dit effect kan worden gecorrigeerd door het gebruik van dubbel-frequentie ontvangers. Het derde effect, Faraday rotatie, is afkomstig van radio golven die de anisotropische Ionosfeer binnendringen, met het in acht nemen van Plasma Theory. De twee resulterende radio golven zijn georiënteerd in de richting waarin deze zich voortplant en het magnetisch veld van de aarde. Dit zijn een normale en extranormale golf. Deze drie effecten zijn uit te drukken met de Appleton-Hartree vergelijking, gevonden door Sir Edward Appleton (Nobel prijs, 1950)

Om de Appleton-Hartree vergelijking op te lossen, is het nodig om de elektronen dichtheid te karakteriseren. Dit wordt gedaan met een Elektronen Dichtheid model. De elektronendichtheid varieert op hoogte, breedtegraad en tijdsschaal.

De voornaamste ionisatiebron is de zon. Doordat de zonnewind invloed uitoefent op de atmosferische deeltjes door deze te ioniseren. Het voornaamste verlies is afkomstig van recombinatie van geladen met neutrale deeltjes en diffusie. Toevoeging hierop is dat het verlies door plasma transport door atmosferische verstoringen, beschreven kan worden met scintillatie, fase instabiliteit en decoherentie. Dit kan samengevat worden als variërende elektronen in de Ionosfeer. Deze elektronen worden geproduceerd, gaan verloren en worden getransporteerd. Dit zijn dezelfde elektronen die de verstoringen van radio golven teweeg brengen.

Wanneer de aarde bekeken wordt vanuit een ander perspectief, is haar atmosfeer grotendeels te karakteriseren door bepaald gedrag, dat gebonden is aan tijd- en breedtegraad variaties. Twee voorbeelden zijn de Aurora (spontane golf lengte-afhankelijke-emissie van plasma in de poolgebieden) en een fontein effect rond de magnetische evenaar. Typerende frequenties van het plasma kunnen gevonden worden bij bepaalde fenomenen, doordat de bron meetbaar is met bijvoorbeeld de plasma frequentie of cyclotron frequentie. Deze frequenties zijn te categoriseren en zijn het resultaat van weersomstandigheden in de ruimte. Verbinden tussen eerder omschreven gedrag van Ionosferische variatie in elektronendichtheid kan worden geobserveerd, of voorspeld door magnetische pulsaties van de Magnetosfeer. Geomagnetische pulsaties worden veroorzaakt door weersomstandigheden in de ruimte en resulteren in Ionosferische variatie. De Ionosferische variatie zorgt voor de verstoorde radio golven waarin we geïnteresseerd zijn.

Doel van dit onderzoek is om de mogelijkheid van het gebruik van lokale metingen te onderzoeken in een voorspelling van weersomstandigheden in de ruimte bij het gebruik van satellietcommunicatie.

Keywords: SWI, SSA, MHD, Voortplanting van Radio Wave, *TEC*, benadering van Ionosferische lagen

Acronyms

Symbols | C | E | G | H | I | K | L | M | P | S | U | V

Symbols

TEC Total Electron Content

C

CDPS Cold Dense Plasma Sheet (CDPS)

CME Coronal Mass Ejections

E

EM Electromagnetic (EM)

EMF Electro Magnetic Force (EMF)

EUV Extreme Ultra Violet (EUV)

G

GNSS Global Navigation Satellite Systems (GNSS)

GPS Global Positioning System (GPS)

H

HE High-energy (HE)

HFA Hot Flow Anomaly (HFA)

HSS High-Speed Stream

I

IMF interplanetary magnetic field (IMF)

ISMR Ionospheric Scintillation Monitoring Records (ISMR)

K

KHI Kelvin-Helmholtz instability (KHI)

L

LUF Lowest Usable Frequency (LUF)

M

MHD Magnetohydrodynamics

MUF Maximum Usable Frequency (MUF)

P

PCA Polar Cap Absorption (PCA)

S

SID Sudden Ionospheric Disturbances (SID)

SSA Space Situational Awareness (SSA)

STEC Slant Total Electron Content (STEC)

SWF Wave Fadeout (SWF)

SWI Space Weather Impact

U

UV Ultra Violet (UV)

V

VTEC Vertical Total Electron Content (VTEC)

chemistry

Notation	Description	Symbol	Page List
N_2	Molecular Nitrogen	N_2	
	Ionized Molecular Nitrogen	N_2^+	
O_2	Molecular Oxygen	O_2	
	Ionized Molecular Oxygen	O_2^+	
He	Helium	He	
	Ionized Helium	He^+	
H	Hydrogen	H	
	Ionized Hydrogen	H^+	
NO	Nitroxigen	NO	
	Ionized Nitroxigen	NO^+	
N	Atomic Nitrogen	N	
	Ionized Atomic Nitrogen	N^+	
O	Atomic Oxygen	O	
	Ionized Atomic Oxygen	O^+	

This page intentionally left blank.

This page intentionally left blank.

Symbols

Q_x Heat flux Electron-Ion heat flux . Electron-neutral heat flux . Ion-electron heat flux . Ion specific heat flux . Ion-Neutral heat flux . Ion Heat flux . Photon-Electron heat flux .

δ_b^k Differential Code Bias for receiver

δ_b^k Differential Code Bias for satellite

$\int_{z_0}^{z_\infty}$ Integral with limits as atmosphere top and surface

ζ_4 Converting coefficient for delay

ζ_e Ionospheric delay caused by 1 TECU

$v.a$ Velocity-dependent collision term that prevents ions from becoming supersonic along the magnetic field

$v.j$ Velocity in other direction

$i4^k$ Combination of code observations

v_i Ion velocity

\vec{B} Geomagnetic Field (\vec{B}) Field aligned component of the Geomagnetic field (b_s)

D_{st} Linear Geomagnetic index

D Geomagnetic Field Declination angle

I Geomagnetic Field Inclination angle

\vec{E} Electric field vector (\vec{E})

E Magnetic flux density (E)

$F_{10.7}$ Solar radio flux 81-day average of the solar radio flux .

F Force

H_0 Scale Height

H Electric flux density

\vec{B} Magnetic field vector (\vec{B})
 I Solar Radiation Intensity
 J Electric current density (J)
 P Pressure Electron pressure (P_e) . Ion pressure (P_i) .
 T Temperature in units of K Neutral temperature . Electron temperature . Ion temperature .
 χ_{sza} Solar Zenith Angle
 δ_t^k Ionospheric delay
 λ wavelength in nm
 ∇ La place Operator
 ρ_0 Earth's surface Density
 ρ Mass density Electron mass density . Ion mass density .
 σ Conductivity (σ) Hall conductivity (σ_{Hall}) . Pederson conductivity (σ_{Ped}) .
 τ Optical Depth
 a_p Linear Geomagnetic index
 f Frequency in Hz Ratio of frequency over Plasma frequency . Carrier Frequency (MUF) . Code Frequency (MUF) . E-layer reflected frequencies . Critical frequency . Gyro frequency . Plasma Frequency . Ion-Ion Collision frequency . Ion-Neutral Collision frequency .
 g Gravitational force in $m s^{-2}$
 m Mass in kg Electron mass . Ion mass .
 n Number density Electron number density . Ion number density .
 $q_{component}$ Ionization due to a reaction rate or process Ionization due to Chemical reactions rate . Ionization due to collisions . Ionization due to Solar Radiation rate .
 q charge
 t Time in units of s
 u_n Neutral zonal wind velocity in $m s^{-1}$
 v_n Neutral wind velocity
 z Vertical height in m Earth's surface Height . Earth's atmospheric height .
 E_s Field aligned component of the electric field (E_s)

χ Electric susceptibility (χ)

χ_m Magnetic susceptibility (χ_m)

μ Permeability (μ)

ϵ Permittivity (ϵ)

κ_e Thermal conductivity of electrons (κ_e)

Numbers

Notation	Description	Symbol	Page List
C	Speed of light in $300\,000\,000\text{ m s}^{-1}$	C	
R_{earth}	Earth radius in m	R_{earth}	
e^-	Elementary Charge in C	e^-	
h	Planck constant in $6.63 \times 10^{-34}\text{ Js}$	h	
k_B	Boltzmann constant in $1.38 \times 10^{-23}\text{ JK}^{-1}$	k_B	

1 Introduction

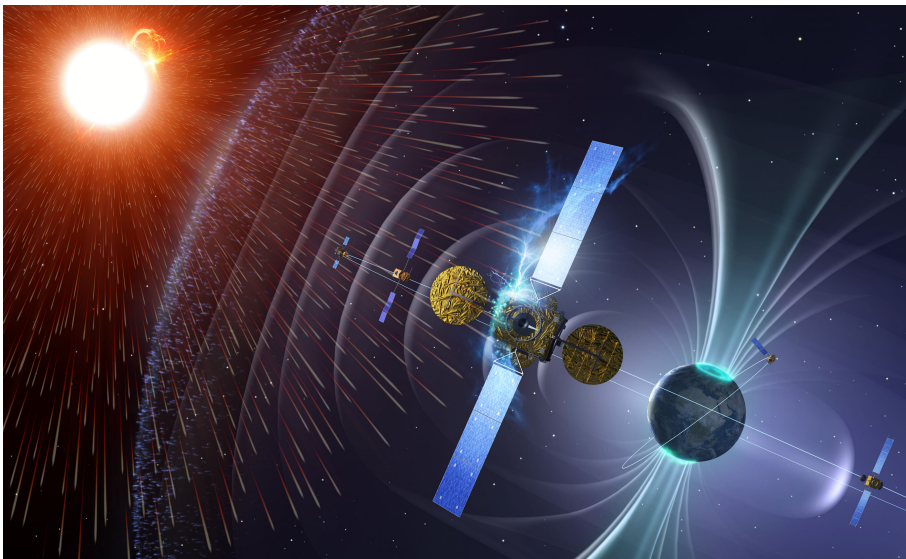


Figure 1.1: Artistic impression of Space Situational Awareness. The Solar radiation and the Sun in the upper-left corner in this figure are interacting with Earth's magnetic field. The satellite in this figure is having a hard time enduring the Solar radiation, but this satellite has a wonderful view out there to enjoy.[63]

Chapter objectives:

- Motivate this research
 - Explain the objectives
 - Introduce further chapters of this thesis
-

1.1 Motivation

The rapid development of satellite communication has led to the interest in Space Weather phenomena, together with a dependency of significant size on space based services. Defence, civil and, scientific applications are available to give insight in the consequences of space weather impact. Satellite communication has become a modern day topic and part of our daily life. There is an expectancy to bring more and more components into space or bring them down, all for different (intellectual) purposes. Satellites are used to communicate, observe, apply surveillance and navigate. In all cases communication by means of a signal propagating through the atmosphere is required. For civil and military applications there are possibilities of enhancing or disturbing the broadcast signal. Disturbance of this communication signal could have consequences in air flight, military operations or other positioning and navigation situations.

Communication between a satellite signal source and a receiver is possible due to the use of radio waves. Radio waves propagate through the atmosphere of the Earth to reach both the signal source as the receiver. In free space, a propagating wave would not be disturbed. In the real world as we know, radio waves are disturbed by physical processes. This can be observed as the wave changes in space and time. Examples of these characterised processes include reflection, diffraction, or scattering of the radio wave. Reflection is where a propagating wave is reflected on a surface at a certain angle. Refraction is when the reflection occurs with an object much larger compared to the wavelength of the radio wave. Refraction describes the radio wave to bend around obstacles or it diverges. Scattering is when the object is small compared to the radio wave. This results in the propagation of the radio wave to be reflected in multiple waves. The path a radio wave takes interferes with the wave. Other physical processes lead to a change in phase, which amplify or cause fading on the radio wave.

The atmosphere is an environment or medium in which the radio waves are propagating. The atmosphere is highly variable, as e.g. Pressure, Temperature in units of K, and concentration of atmospheric species are observable to vary. Different processes are interact with each other to form a dynamic atmosphere. A dynamic atmosphere has an influence on the propagating radio waves needed for satellite communication. Ionized atmospheric species, charged ions, and electrons are most prominent at a region called the ionosphere. The *TEC* is key to understand the changing atmosphere. The development of electron density modelling will be described in this thesis. With this model, the possibility of making an expectation or forecast on the disturbed radio waves is possible.

1.2 Research Objective

Below the primary research objectives are summarised:

- ✓ Realisation of an Electron Density Model to describe the total electron content to interpret and quantify Ionospheric effects on radio wave signal.
- ✓ Discuss and validate the model against other models and literature.

- ✓ Realization of a model forecasting scheme and describe the use of local measurements in the forecasting scheme.

1.3 Outline of this thesis

- chapter 1 This chapter gives a motivational introduction and the research level it has been performed on. After the goals and objectives were made clear. The thesis outline will guide you through this thesis.
- chapter 2 A foundation of fundamental physics will start at chapter 2. The atmosphere is introduced by presenting its profile. The Ionization balance will take you towards the ionosphere, where most of the action takes place.
- chapter 3 This chapter introduces Radio Waves and how they are affected by the atmosphere. The Atmospheric influence will be presented by deriving quantities to better grasp the actual effect. Electron Density variations are explained afterwards, where the variation in vertical structure, and latitudinal direction of the ionosphere are shown.
- chapter 4 The morphology of Earth's magnetosphere and its relation to the Ionospheric Electron Density variations is covered in this chapter. It shall give a feeling for Space Weather as a response of the Solar wind - Magnetosphere - Geomagnetic field-system, which causes the Ionospheric Electron Density variations we are interested in. Space Weather Phenomena are presented, with their characterizing behaviour and their disturbing effect on Radio Waves.
- chapter 5 With the quantified variables of chapter 3 and gathered knowledge, a model is presented. The first section introduces the input parameters, after which the approach is shown, with a section on validation of the Model. The chapter ends by giving an overview of other Space Weather and Electron Density Models.
- chapter 6 This chapter shows the results of the electron density model of chapter 5.
- chapter 7 An outlook of the research is given in this chapter. A summary will centralize the approach, methodology, and results, after which recommendations and final conclusions shall end this story.

This page intentionally left blank.

2 The atmosphere

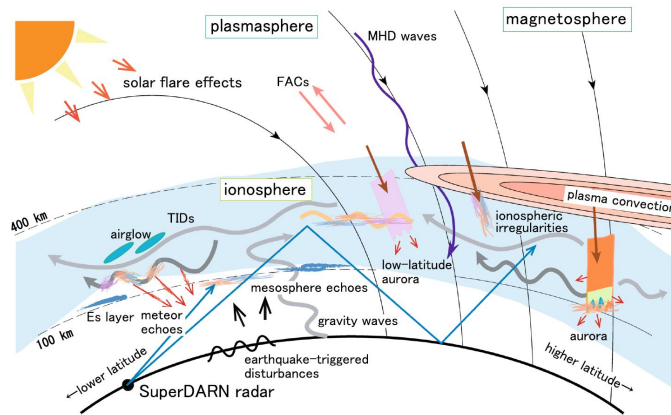


Figure 2.1: Schematic of phenomena occurring in the ionosphere. The phenomena shown in this figure are having an effect on waves propagating through the atmospheric layers. [26]

“ A theoretical framework is needed to proceed to build a forecasting model. The content of this chapter builds upon the literature review which was done during this thesis and gives explicit statements or assumptions, guiding us towards key variables and initial details of the model. The chapter starts with a few concepts of physics in an atmosphere. The density of e.g. Atomic Oxygen, Molecular Oxygen and (Atomic Nitrogen, Molecular Nitrogen) varies on multiple scales e.g. vertical, latitudinal, and temporal. The derivation of the Solar irradiance is shown in the first section. The balance of ionized ionosphere this robin, resulting in ρ_e . Details on Electrodynamics are described next. Figure 2.1 depicts the phenomena occurring on different scales. ”

Chapter objectives:

- Provide theoretical background on the atmosphere
 - Explain the main atmospheric processes and their purpose
-

2.1 Introduction to the atmosphere

This section provides background information and serves as a bridge for understanding later presented new, or unfamiliar, concepts in this study, mainly described in section 2.3, chapter 3, and chapter 4. The use of satellite signals for navigation, positioning and communication, is being affected by distortion. There is a delay in a propagating radio wave between a source (at Earth's surface) and receiver (at a height of several 100 km). At the low region of the atmosphere, signal absorption causes a delay due to the neutral species that are present. In the ionosphere, where there are charged particles due to photoionization processes, the effect on radio waves is even larger. When satellites only have one receiver, the effect needs to be considered. When there are two useable frequencies (dual-frequency) at the receiver, ionospheric delay can be eliminated by the combination of signals.[52]

A correction of ionospheric effects originates from [7], which assumes a single ionospheric layer within the line of sight of the source, and the receiver. A relation between a slanted and vertical propagation path can be mapped. A mapping function is used for quantifying the radio wave signal delay.[7]

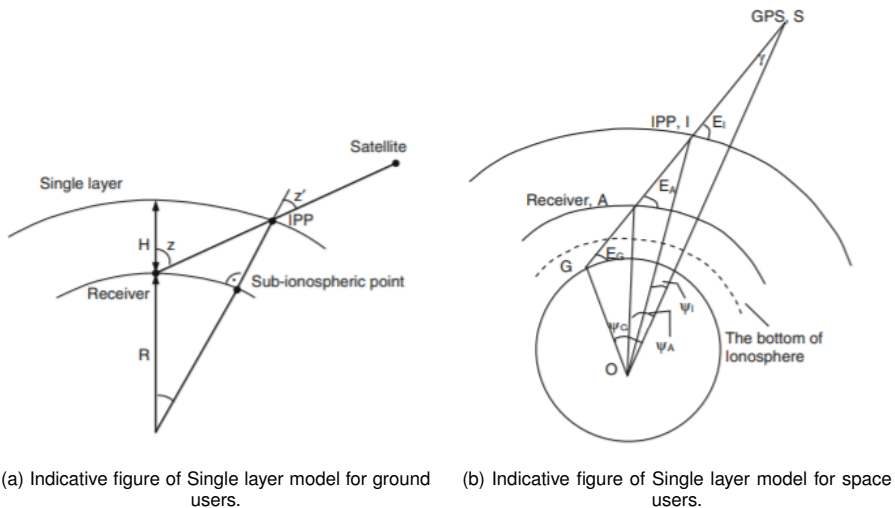


Figure 2.2: Indicative figure of Single layer model for ground and space users. [52]

A steady atmosphere can be described with literature, while the dynamic version of this atmosphere is influenced by some instabilities known and recognized as the weather. The weather in this thesis is Space Weather.[58]

Bursts of charged particles, ejected by the magnetic field of the Sun's atmosphere, are the main source of Space Weather. The Sun is continuously emitting solar radiation and charged particles, which interact with geomagnetic field (\vec{B}). All this energy enters Earth's atmosphere via an oval region at the poles where the well-known Auroras (Northern and Southern lights) occur. The term atmosphere

is sometimes misinterpreted because of her different layers. The atmosphere can be interpreted as all these layers, where the ionized D-, E-, F1-, and F2-layer form the ionosphere, starting at a height of 90 km, extending several hundred kilometres. Charged particles are flying around in the ionosphere at different velocities, sometimes even close to the speed of light. A relativistic velocity is nearly the Speed of light (C).

2.2 Atmospheric profile

The atmosphere is described in this section using the (2.2), scale height (H_0), and Equation 2.4. The distribution of neutral species can be assumed with the (2.2) and the (2.1)

Ideal gas law

The pressure (P) of a gas is described ideal when:

$$P \equiv nk_B T \quad (2.1)$$

Where number density (n), Boltzmann constant (k_B), and temperature (T) are used.

Hydrostatic equation

The Hydrostatic equation can be used to find a relation for the atmospheric mass density (ρ).[5, 38]

$$\frac{dP}{dz} \equiv -\rho g \equiv -nmg \quad (2.2)$$

Where gravity (g) is used. To find the relation ρ equals nm .

Scale Height

The H_0 represents the vertical distance which decreases exponentially and is an important parameter in atmospheric science.

$$H_0 = \frac{k_B T}{mg} \quad (2.3)$$

Atmospheric Thickness

The function which describes the atmospheric thickness (dZ) can be calculated as the integration between the Earth's atmospheric height (z_∞) and Earth's surface Height (z_0). The atmosphere is assumed to be spherical. The atmospheric thickness is then written as:

$$\int_{z_0}^{z_\infty} \rho dz = \int_{z_0}^{z_\infty} \frac{\rho_0 H_0}{e^{-h}} dz \quad (2.4)$$

Where the Plank constant (h) is used ($h = \frac{1}{2} \cos \chi_{sza} s^2$). The radius of Earth (R_{earth}) is 6.38×10^3 m and represents the height in vertical direction. To find Earth's surface Density (ρ_0), it is used that $\rho_0 = \frac{k_B T}{H_0 g}$.

$$dz = \frac{\rho_0}{\cos \chi_{sza}} \exp -s \frac{\cos \chi_{sza}}{z_0} \quad (2.5)$$

Where the height (z) is a function of s and the solar zenith angle (χ_{sza}). Here we have neglected the term $2s^2 R_{earth}$. Since it does not make a difference for an angle below 85 deg.[5]

Atmospheric structure

The absorption of ozone causes an increase of T_n increase at around 10 km altitude. This region is the Tropopause and indicates where the Stratosphere begins. Solar Ultra Violet (UV) radiation causes an increased Temperature in units of K which maximizes at 50 km altitude. The electron temperature and ion temperature will be explained later in this thesis. Radiative cooling reverses the Temperature in units of K at around 90 km. For heights above the altitude of minimal Temperature in units of K (Mesopause), there is an increase due to Solar Radiation absorption [See 38] Especially High-energy (HE) (HE) Solar Radiation like Ultra Violet (UV) and Extreme Ultra Violet (EUV) There is enough energy to ionize the neutral atmosphere. The figure below presents the profile of the atmospheric layers.

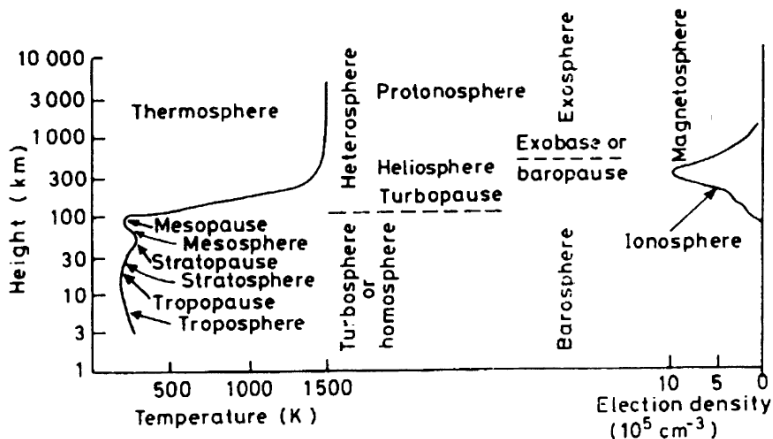


Figure 2.3: Structure profiles of the atmosphere, with its layers, T , and Electron number density shown.[1]

The most prominent species are N_2^+ , O^+ , and O_2^+ at low altitude (below 200 km) and atomic ions at high altitude (above 200 km). Belehaki, Stanislawski, and Lilienstein also present the fact that N^+ is created by dissociative ionization of N_2^+ and H^+ by charge exchange reactions between O^+ and H. The NO^+ arises from chemical recombination with neutrals. A major ion in the E-layer is NO^+ , although it is not before ionized. The E-layer will be explained later in this thesis with other regions of the ionosphere. This is also illustrated below.

At night time ionized O is sustained due to different recombination rates with electron (e^+) than with ions. Fast chemical reactions occurring are In [27] a distinction of positive and negative ions is made by looking at the subsequent ion chemistry and ionisation in a mixed neutral atmosphere. At higher altitudes photons are expected to dominate, resulting in $O + \text{coulomb} \rightarrow O^+$ The O^+ plasma (ions and e^- often survives the night at higher altitudes.[38]

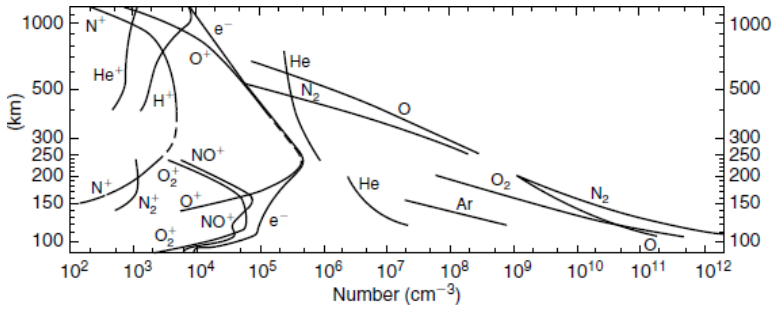


Figure 2.4: Distribution of atmospheric atoms and molecules.[38][1]

2.3 Atmospheric processes

The ionosphere exists due to the production and losses of charged particles. This can be seen in (2.6) below. Ions are continuously being produced and lost against their neutral version and coulomb, as is described in subsection 2.3. When a volume of particles starts to move due to their net concentration, this is called diffusion or Electron drift. Because of the presence of Ions and e^- , the ionosphere is a medium that disturbs the propagation of radio waves, which will be discussed in chapter 3.

$$\frac{\partial n_i}{\partial t} + \nabla \cdot (n_i v_i) = q(z, t) - l(z, t) \quad (2.6)$$

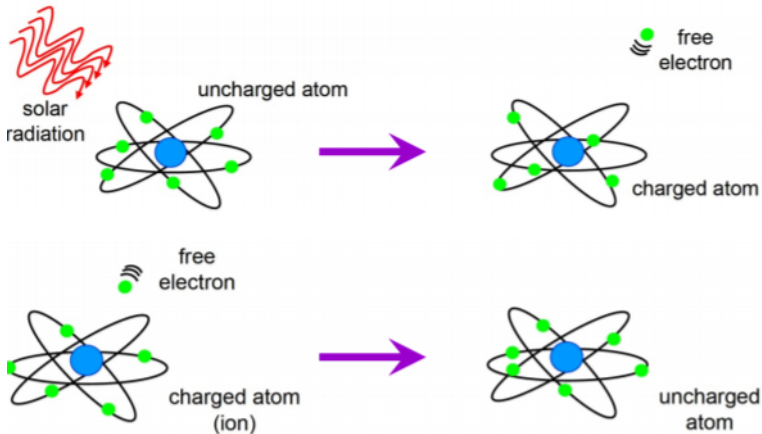


Figure 2.5: Production and loss of Elementary Charge in C (e^-) in the ionosphere

Photo Ionisation mechanism

There is a balance of ionisation between production and losses of ions, e^- , and neutrals. The total ionization production is the sum of:

(1) Ionization due to Solar Radiation rate (2) Ionization due to collisions with e^- , neutrals, and other ions. And, (3) Ionization due to Chemical reactions rate. Loss rates are due to recombination, loss of ionization due to collisions, and loss of ionization due to Chemical reactions rate. Recombination can occur as recombination of ion species: (1) Radiative recombination, (2) Dissociative recombination, and (3) ion-ion recombination. The production ($q(z, t)$) and loss rate ($L(z, t)$) can be expressed as:

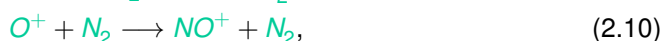
$$q(z, t) = q_{photo}(z) + q_{coll}(z) + q_{chem}(z, t) \quad (2.7)$$

$$L(z, t) = I_{rec}(z) - q_{coll}(z) - q_{coll}(z, t) \quad (2.8)$$

Ionization by absorption

Ionization by absorption is not the only source of plasma (ions and electrons) in the ionosphere. Ionization by energetic particle impact on the neutral gas is important at high latitudes. Visible light is emitted when these particles strike the atmosphere, creating the visible aurora. The typical nightly auroral electron energy is 310 keV, and its impact is the dominant ionization source. This energy range results in large plasma production in the E-layer, $10 \times$ higher than during daytime. This results in E-layer production.[38]

Ionization in ionospheric layers are mainly due to the production of electrons in the F1-layer. These are ejected from O_2 , O, and N_2 . While there is a preference for stable reactions, the most likely reactions to occur are O^+ and N_2^+ reacting with neutral species to form NO^+



The E- and F1-layer contains the highest concentration of O_2^+ and NO^+ . At lower heights, there is also the production of NO^+ by the reaction shown below. In the D-layer, water vapour and NO^+ form H^+ and other higher hydrated ions, but are bound by certain heights due to the availability of water.



Dissociative Recombination

Recombination is when ionized ions recombine to neutrals. When this happens, there is a release of energy to kinetic energy or released as radiated light, causing unstable fast-moving particles. The light which is possible to occur is mainly visible in green and red, due to the presence of O^+ in the reactions. The phenomena are named airglow, or Aurora Borealis is one of these results. The most dominant reactions are shown below.



Radiative and Direct Recombination

Radiative and direct recombination is of less importance, due to the fact these mechanisms do not occur often or need strict conditions to occur, so it is not discussed here.

Balance of ionisation

The Beer-Lambert law below shows its use to calculate the solar radiation intensity (I). Before this is possible, optical depth (τ) is needed. This is shown in the definition of τ below.

The Law of Beer-Lambert

This law relates the absorption of light with the properties, concentration and τ of the medium it propagates through.

$$I(\lambda, z) = I(\lambda, z_\infty) \exp[-\tau(\lambda, z)] \quad (2.20)$$

Where the I is defined with (λ, r) and $(\lambda, r(end))$, the I at the top of the atmosphere.[9]

Optical depth

The τ , can be calculated for each species and is given below. Note here that it also includes the χ_{sza} previously introduced in Figure 1.3.

The area on which the photoelectron collides has a cross-section specific for each atmospheric species. This is named the photoabsorption cross-section. The ion production rate due to ionization can be calculated by summing over all species. The profiles of species number densities can be calculated with the right cross-sections and Solar Flux Spectrum:[12, 5]

After the ion production rate has been calculated, ρ_e can be derived assuming steady-state electron transport. This photochemical equilibrium is defined as ionization due to Solar Radiation rate(z, t) = $L(z, t)$. It can be assumed that $\frac{dn_e}{dt} = 0$, so the production rate equals the e^- loss rate to hold Photochemical equilibrium: [8, 49]

$$\frac{\partial n_e}{\partial t} = q(z, t) - L(z, t) \quad (2.21)$$

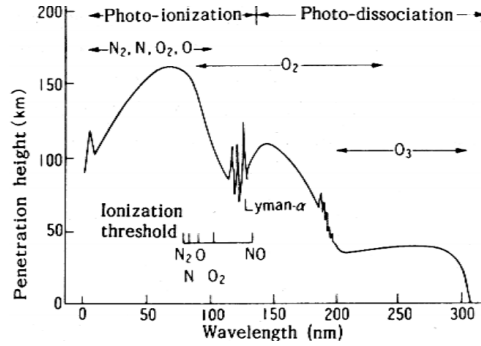


Figure 2.6: Solar radiation depth as function of wavelength in nm for Ionization processes.[38]

Atmospheric Chemistry

Chemical reaction rates

The chemical production and loss rates of a reaction can be described by e.g. $A^+ + B \rightarrow C^+ + D$, where A and C are ionized species and B and D neutrals. The time evolution of A and C can be defined as [38, 9]

$$\frac{\partial q_{C^+}}{\partial t} = R[A^+][B], \quad \frac{\partial I_{A^+}}{\partial t} = -R[A^+][B] \quad (2.22)$$

In these equations, C^+ is produced and A^+ is being lost at the same rate. If the density of an ionized species is not changing over time, it is said to be in a steady-state, or a photochemical equilibrium $\frac{\partial I_{A^+}}{\partial t} = 0$. The concentration of atmospheric species can then be said to stay constant, so the production and loss rate are equal, production equals Losses. Under steady-state conditions, the total amount of ions, coulomb and ions can be calculated by taking all the reactions into account.

$$n_i = \sum_{\text{species}} n_i \quad (2.23)$$

Particle collision

The interaction of neutral species interaction with ions occurs at a certain f_{gyro} . The opposite, so when ions interact with neutrals, can be expressed with n times the ion-neutral collision rate coefficient. The relation of f_{gyro} and the ion-neutral collision frequency indicates if ions are most affected by the neutral wind ($< f_{ion-neutral}$) or \vec{B} ($> f_{ion-neutral}$). A balance of the two causes a mixed influence of both neutral wind and \vec{B} . When this is happening, an Electric field vector (\vec{E}) is created, due to the electric current, caused by the moving of ions and Elementary Charge in C . This Electric field vector (\vec{E}) is then affecting the motion of ions and coulomb again, called drifting of the charged particle. Much simplified can be said that the Geomagnetic Field (\vec{B}) causes to be affected as moving in a circular motion around the magnetic field lines, named plasma drift. The divergence of the continuity equation can be calculated with the drift velocity of the Ion. The full equations can be found in [49].

Magnetohydrodynamics (MHD)

The describes magnetic fields, moving conductors and their interaction, it can be seen as an evolved version of electrodynamics. Electrodynamics consist of at least a Geomagnetic Field (\vec{B}) and a neutral zonal wind velocity (u_n). Their interaction is characterized by Faradays Law and Amperes Law. This is due to the Lorentz force being present and induces a current.

Electromotive force:

this results from Faradays law of induction. 1. The force is caused by the movement of a conducting fluid and Geomagnetic Field (\vec{B}), on the order of $|U \times \vec{B}|$. 2. J adds conductivity to this order, becoming the J : results in another Geomagnetic Field (\vec{B}), described by Amperes law. The Geomagnetic Field (\vec{B}) can be added and the change appears as being dragged by the fluid. The total Geomagnetic Field (\vec{B}): results in the Lorentz force, when it interacts with the induced Electric current density (J). The Lorentz force $J \times \vec{B}$ is acting on the conductor and is directed in similar direction as the fluid and the Geomagnetic Field (\vec{B}).

A description of the Coulomb force, Ohms law, Amperes law, and the Lorentz force is given. Below in Figure 2.7a Ohms law is shown, and Faradays law in Figure 2.7b.

Coulomb force

For stationary conductors

$$F = q\vec{E} \quad (2.24)$$

can be written. Where the charge and Electric field vector (\vec{E}) are used.

Ohm's law

For stationary conductors, the Electric current density (J) is expressed with the Conductivity (σ) and Electric field vector (\vec{E}) as $J = \sigma\vec{E}$. When the conductor is moving in an Magnetic flux density (E), $J = \sigma(\vec{E} + u_n \times \vec{B})$.

The electromagnetic force per unit charge (+) is characterized by Faradays law. Which says if the conductor is the result of a time-dependent Geomagnetic Field (\vec{B}), or the motion within.

Ampere's law

This law describes a Geomagnetic Field (\vec{B}), which is acting with an Electric current density (J). This is written as $\int \vec{B} \bullet dl = \mu \int J \bullet dS$

$$\nabla \times \vec{B} = \frac{\delta H}{\delta t} + J \quad (2.25)$$

Lorentz force

This force acts on all conductors with a Electric current density (J) in the Geomagnetic Field (\vec{B}), as a result of the individual charges.

$$F = J \times \vec{B} = q(\vec{E} + u \times \vec{B}) \quad (2.26)$$

Pelletier has shown us two examples, one of a medium that is highly conducting, resulting in elastic oscillations, with a characterizing Frequency in Hz, v_α/l .

And one which is a poorly conductor, resulting in an induction of the imposed field, simplifying the Lorentz force and Ohms law.[29]

Maxwell equations

The Maxwell equations are used. Which were used in the derivation for the wave propagation. The equations below contains Gauss law and Faraday's law. With the relations introduced earlier the Maxwell equations can be completed. Gauss law written here as

$$\nabla \cdot \vec{E} = \frac{\rho}{\epsilon} \tag{2.27}$$

Where ρ is the total charge density divided by the permittivity of free space. And Faraday's law, as shown below

$$\nabla \times \vec{E} = -\frac{\delta \vec{B}}{\delta t} \tag{2.28}$$

And Gauss' law for magnetism as follows

$$\nabla \cdot \vec{B} = 0 \tag{2.29}$$

With Equation 2.29, and the relations shown, the Electric field vector (\vec{E}) and Magnetic field vector (\vec{B}) can be described.

The relations introduced in this paragraph are used with the permittivity and susceptibility. $H = \epsilon \vec{E}$, $E = \mu \vec{B}$, Where a separation of the ϵ , χ in vacuum can be made. Namely with ϵ in $\epsilon_0 + \epsilon \chi$, and μ in $\mu_0 + \mu \chi_m$

It was shown in [59] that to find a solution for the wave solution in the troposphere, the troposphere can be assumed as an isotropic, non-conducting, and neutral medium.[59] This implies the Electric current density (J) and to be zero and the use of Conductivity (σ) and dielectric coefficient Permittivity (ϵ) as tensor notation, to find Plasma Frequency, Gyro frequency, and electron collision frequencies. These three parameters are then used to find a tensor of Conductivity (σ) and the dielectric tensor Permittivity (ϵ). Plasma can be treated neutrally in the scale length is greater than the Debye length. The Debye length is the distance over which the Coulomb force between charged particles can be observed.[9] Another expression for the Debye length is how far into the plasma the effect of the electrons can be observed.

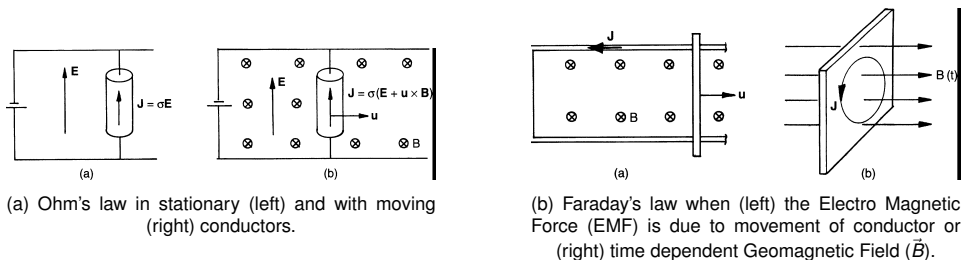


Figure 2.7: Illustration showing the law of Ohm and Faraday.[29]

Conductivity

Pedersen and Hall conductivity

The Electric current density (J), can be defined as $\sigma(\vec{E} + \mathbf{V} + \vec{B})$, where Conductivity (σ) has a component parallel (\parallel) and perpendicular (\perp) on the Electric field vector (\vec{E}), named after Pedersen and Hall, respectively. The equation below shows its definition, where the ratio $(f/f_{gyro}) = (m_i v_{i,n})/\vec{B}$ has been used in the calculation of

$$\sigma_{Hall} = \sigma_{Ped}(f/f_{gyro}) = \sigma_{Ped} \frac{n_i e^- (f/f_{gyro})}{\vec{B}(1 + (f/f_{gyro})^2)} \quad (2.30)$$

$$\sigma_{Ped} = \frac{n_i e^- (f/f_{gyro})}{\vec{B}(1 + (f/f_{gyro})^2)} \quad (2.31)$$

Summary of this chapter

This chapter has shown the theoretical literature of the atmosphere. Next, in chapter 3, an introduction to radio wave propagation and atmospheric effects on radio waves will be given. Then the Electron mass density variations on the vertical and latitudinal scale will be shown. In the next chapter 4, events of Space Weather, responses to Space Weather phenomena, and the morphology of the Magnetosphere will be presented.

This page intentionally left blank.

3 Radio waves

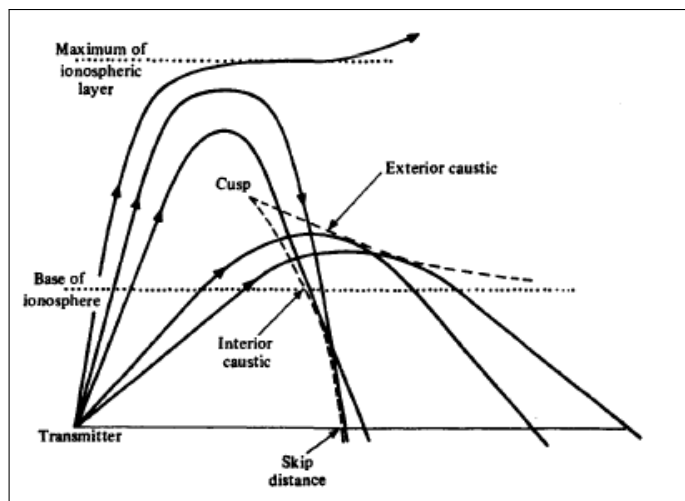


Figure 3.1: Examples of radio waves entering the ionosphere and being affected.[4]

“ This chapter briefly introduces wave propagation and the atmospheric effects on these waves. The effects which are discussed include refraction subsection 3.2, Ionospheric delay and Faraday Rotation. A distinction is made between the troposphere and ionosphere, and different orders of disturbances are converged into quantities to interpret them later on with the Scintillation, which is presented in chapter 4. The ρ_e variations are the cause of a varying disturbance. The Ionospheric ρ_e varies on the vertical and latitudinal scale, resulting in affected radio waves. The variations on the latitudinal scale are focused on Polar and High latitudes and the Equatorial region. Ionospheric instabilities originate from Space Weather, which will be introduced in chapter 4. The Space Weather Phenomena results in distortion of radio waves propagating in the ionosphere. ”

Chapter objectives:

- Explain radio waves in the atmosphere
 - Identify methods to quantify radio wave disturbances
 - Identify electron density variations in the atmosphere
-

3.1 An introduction to radio waves

When operating in the radio-frequency band, the challenge is to determine the propagation velocity. If a wave propagates through a vacuum, the travelled distance would be the light speed in vacuum with the Time in units of s between source and receiver. When a wave travels through a magnetized plasma, like the ionosphere, the propagation phase speed accelerates and the propagation group velocity is slowed down by atmospheric effects.[59]

Radio waves are effected by errors related to the satellite, atmospheric, and receiver. The atmospheric related errors vary due to Space Weather and makes it more difficult then to model satellite receiver related errors. The Ionospheric effect results in a delay of a radio wave propagating through. This delay is caused by fluctuations of the Electron number density. The Tropospheric effects result also in a delay, where Molecular Oxygen and water vapour are drivers of this effect. Locally, there is thermal noise, interference, and there are multipath effects. A clock error rises due to non-perfect orbit determination and time synchronisation.

3.2 Atmospheric effects on radio waves

Refraction

The refraction index is found to be complex, where the imaginary part describes energy absorption of the wave.[59] This is called the extinction coefficient. Wave refraction dissipates energy of the wave into heat, through particle collisions.[59]

For frequency-dependent refraction, the real part results in refraction and the imaginary part results in absorption (signal damping or attenuation) of the radio wave. The Tropospheric absorption coefficient can be found $\alpha = r\pi f N_c(f)/C$. Absorption does not have a direct effect on the signal delay, as it affects the low elevation propagation pathway.[59] This can be thought of like the radio wave taking a longer propagation pathway in the Troposphere, resulting in more absorption. The longer pathway is then argued to be caused by a low elevation angle. The dielectric tensor Permittivity (ϵ), presented in subsection 2.3, can be used with the Equation 2.29 of the same section, to find the Ionospheric refraction index vector $n \times (n \vec{E}) = -\epsilon \vec{E}$. This has the Appleton-Hartree equation as the solution, where is complex, where the distinction coefficient results in a longitudinal and component, oriented between propagation direction and Geomagnetic Field (\vec{B}).

Refraction can be explained as a ray of light that is bending when propagating between mediums. This is also the case for different wavelength in nm , which explains why white light turns out to cause a rainbow effect after it has been separated by a certain medium. It can be defined with a refractive index $n_r = \frac{c}{v}$ and the Maxwell equations to derive a plasma wave solution, this has been done in [5]. The refractive index in a plasma (cold, homogeneous, no collisions) was found to be:

$$n_p^2 = 1 - \frac{f_p^2}{f^2} \quad (3.1)$$

With f_p , the f_p Plasma frequency: $f_p^2 = 1 - \frac{n_e e^2}{4\pi^2 m_e \epsilon_0}$

It was shown that a maximum Frequency in Hz exists, where reflection is not possible. This is named Critical frequency and occurs at the height of maximum Electron number density.[57] This Critical frequency is related to the ordinary and extraordinary wave introduced in section 3.1.

$$f_{crit}(o) = f_p(\max(n_e)) \quad (3.2)$$

$$f_{crit}(x) = f_{crit}(o) + \frac{1}{2} f_{gyro} \quad (3.3)$$

The height at which the wave is reflected has physically two options. A virtual reflection height and a real reflection height. The virtual reflection height is shown below. It is the height at which a wave would be reflected if it would travel at the Speed of light in $300\,000\,000 \text{ m s}^{-1}$.[57]

$$h(f) = \int_0^z ndz \quad (3.4)$$

$$h_g(f) = \frac{Ct(f)}{2} = \int_0^z n_g dz \quad (3.5)$$

Where t is here the Time in units of s needed between source, receiver and reflection height.

Appleton-Hartree equation

The phase n_{ion}^{phase} and group n^{group} refractive index are found to be derived from a series expansion of the Appleton-Hartree formula. ¹. The first, second, and third-order effect describes the refractive index for radio wave propagation in our Ionospheric plasma.[5, 4]

$$n = 1 - \underbrace{\frac{f_p^2}{2f^2}}_{\text{first}} \pm \underbrace{\frac{f_p f_{gyro} \cos(\theta)}{2f^3}}_{\text{second}} \pm \underbrace{\frac{f_p^2}{4f^2} \left[\frac{f_p^2}{2} + f_{gyro}^2 (1 + \cos^2(\theta)) \right]}_{\text{third}} \quad (3.6)$$

Where the Plasma Frequency and Gyro frequency are used, as shown below in (3.7) and (3.8).

$$f_p = \frac{n_e (e^-)^2}{4\pi^2 \epsilon_0 m}, \quad (3.7)$$

$$f_{gyro} = \frac{e\vec{B}}{2\pi m} \quad (3.8)$$

In the next section, it will be explained that Phase advance and Group delay occur when $n_{phase} < 1$ and $n_{phase} > 1$. The Tropospheric refraction was found to have a dry and wet (water vapour) atmosphere effect. The dry component causes 90 percent of Tropospheric refraction error and was found to have a value of **2.30 m** on average in [39].

¹ Derivation explained here: [https://gssc.esa.int/navipedia/index.php/Ionospheric\\$_\\$_Delay](https://gssc.esa.int/navipedia/index.php/Ionospheric$_$_Delay)

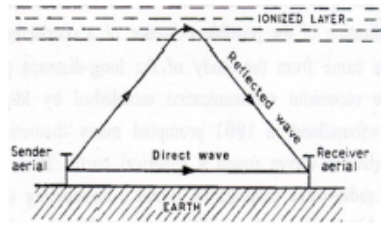


Figure 3.2: Illustration of radio waves propagating in the ionosphere, as has Appleton shown in his Nobel lecture. [78]

Ionospheric Delay

Dispersive, resulting in wave refraction in a phase and group velocity, where the refractive index is frequency-dependent. The Dispersion effect, shown later, causes a Phase advance and Group delay and can be corrected using Dual Frequency Receiver.[36]

A relation for phase n_{ion}^{phase} and group n_{ion}^{group} delay can be found by integrating over the refraction index. This group delay $\delta^{group,f}$ accounts for 99.9 % Usually the 2nd and higher-order terms are neglected.[22] This Phase velocity of the carrier signal, increases when more Elementary Charge in C are present. This causes the signal to arrive earlier at the receiver i. e.Phase Advance. At the same time, a modulated signal can be delayed by superposition of slightly different frequencies i. e.Group delay.[5, 7] The phase and group delay as:

$$\varphi^{phase,f} = -40.3 \frac{n_e}{f^2} \int_{z_0}^{z_{\infty}} n_e dh, \quad \varphi^{group,f} = +40.3 \frac{n_e}{f^2} \int_{z_0}^{z_{\infty}} n_e dh \quad (3.9)$$

Total Electron Content

The combination is used to calculate the First order Ionospheric effect, shown in Equation 3.10 below. The Ionospheric electron density variations are the cause of refraction, allowing the upper atmosphere to be used as a mirror.[5]. There is a Maximum Usable Frequency (MUF) $(MUF)^2$ when $\sec(\Psi_i) = \max$. Some literature suggests the MUF does not exceed 40 MHz or 25 MHz to 30 MHz during low solar activity. With the reflection height h it is possible to find maximum distance a radio wave travels (maximum skip distance) $d = 2\sqrt{(2a_e h)}$, and maximum angle $\tan(\Phi_i) = \frac{1}{2} \frac{h}{d}$. [77]

$$TEC = \int_{z_0}^{z_{\infty}} n_e dh \quad (3.10)$$

Faraday Rotation and Doppler effect

The anisotropic property of the ionosphere results in propagating waves, which enter the ionosphere, to split into two waves. These are oriented by their direction of propagation and the Geomagnetic Field (\vec{B}). The waves are named an ordinary

²Which can be used as $MUF = 9\sqrt{(\max(n_e))\sec(\Phi_i)}$ plane interface between the ionospheric layers.

(*O*) and extraordinary wave (*X*). The ordinary and extraordinary waves are rotating in different directions due to them being reflected and their polarisation. This behaviour is discussed in subsection 3.2, as it is named Faraday rotation. The Frequency in Hz of a received radio wave is altered due to movement of atmospheric layers. This is named Doppler effect, also shown in subsection 3.2.

The Faraday rotation describes the change of polarization of the radio wave. The ionosphere is anisotropic, meaning it causes radio waves to split when entering the ionosphere as an ordinary (*O*) and extraordinary wave (*X*), which recombine after penetrating the Ionospheric layer. This splitting-wave-phenomena is named Birefringenc. This is simply said just double refracted. When the waves are recombining, they have a different plane of polarization, caused by the e^- moving due to the Geomagnetic Field (\vec{B}). This effect is named the Faraday Rotation.

The plasma and cyclotron frequency ($f_p^2 = \frac{n_e^2}{m\epsilon_0}$ and f_{gyro}) can be used with an expression of the Geomagnetic Field (\vec{B}), and polarization vector $P = n_e e^- r$, to obtain a wave equation for the Electric field vector (\vec{E}). The solution is a constant of (*O*) and *X* wave propagation, resulting in a circularly wave propagation and cause fading by cancelling out (destructive) or amplify each other (constructive). The propagation constant, and Faraday rotation, can be defined over a distance d travelled, as is shown in the equation below.[32, 31, 33, 37]

The waves combined, which have constructive and destructive effect due to ordinary (*O*) and extraordinary wave (*X*), are named *Multipath fading*, as it can be characterized by amplitude, Phase delay, Time delay, and Phase rate of change. The Phase rate of change is called Doppler fading, as it represents the relative Doppler frequency change between direct and Multipath.[39]

$$k_f = \frac{k_{ordinary} + k_{-extraordinary}}{2}, \quad \theta_f = d \frac{k_{ordinary} + k_{-extraordinary}}{2} \quad (3.11)$$

3.3 Ionospheric Forecast

When a propagating radio wave is absorbed by the atmosphere, it is most likely to be absorbed in the D-layer, and would not have happened if the Frequency in Hz would have been higher. If the Frequency in Hz of the wave is in fact higher, the wave is reflected or refracted at a higher region, namely the E- or F-layer. If the Frequency in Hz is too high, the radio wave will be refracted, but not directed at Earth. The upper and lower frequencies are characterized as the MUF and Lowest Usable Frequency (LUF) (LUF). Determination of the MUF can be found to be vertically reflected frequencies multiplied by a distance factor, and addition of $\frac{1}{2}f_{gyro}$. The vertically reflected frequency depend on the E- and F-layer, solar activity and temporal. Determination of the upper radio wave frequency when reflected by the E-layer is a distance factor multiplied with E-layer reflected frequencies. The f_E is a monthly average. Determination of the LUF can be estima To calculate the loss in a pathway, the Tropospheric absorption and Ionospheric absorption due to particle collision are taken.

3.4 Quantifying disturbed radio waves

This section shows a step by step process of how to quantify the disturbance of radio waves due to atmospheric origin. A literature based example was found to be [7], who showed a simple method to present the disturbances. [20] has shown the derivation of coordinates of the Ionospheric piercing point, computed from receiver coordinates (φ, λ) in (3.13), Zenith and Azimuth angle (z, a) to be.

$$\varphi = \arcsin(\sin(\varphi)\cos(z - z') + \cos(\varphi)\sin(z - z')\cos(a)), \quad (3.12)$$

$$\lambda = \lambda + \arcsin\left(\frac{\sin(z - z')\cos(a)}{\cos(\varphi)}\right) \quad (3.13)$$

- The First order effect can be attributed to the transparency (or Opacity) of the plasma at Frequency in Hz below its critical Plasma Frequency.
- Second-order effects are characterized by Refraction, Dispersion, and Faraday rotation, described in section subsection 3.2 and subsection 3.2.
- Third-order effects originates from a disturbed ionosphere. This results in information loss to the surrounding (Scintillation, Phase instability, and Decoherence), image distortion (Variable refraction) and change of position (Phase stability).
- Fourth-order effects, can be interpret as the radiation of the ionosphere, i. e. Bremsstrahlung (radiation of a particle when accelerating) or the plasma frequency (Plasma Frequency).

All Ionospheric effects (Refraction, Polarisation, Path length, and Absorption) are in the order of $\frac{1}{f^2}$, except the phase change, which is in the order of $\frac{1}{f}$.

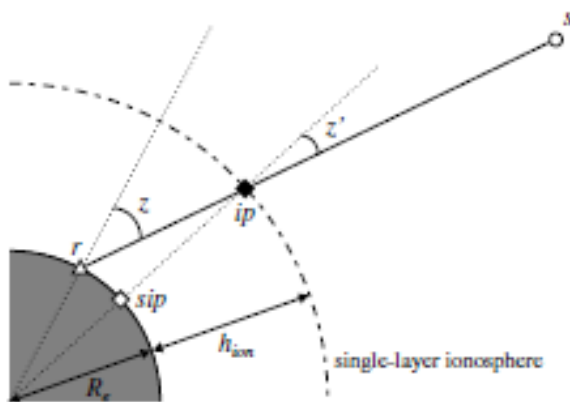


Figure 3.3: Schematic of a Single Ionospheric Layer Geometry, shown by [20]

Ionospheric delay

Ionospheric delay to the first Frequency in Hz, as has been found in [25], as shown

in (3.14). The relationship of Total Electron Content and Ionospheric delay is used later for an absolute Total Electron Content determination. The Ionospheric delay can be expressed as:

$$\delta_t^k = \frac{i4^k - c(\delta_b^k + \delta_b^k)}{\zeta_4} \quad (3.14)$$

$$\delta_t^k = \pm \frac{1}{2} C_x TEC f_1^2 = \zeta_4 TEC \quad (3.15)$$

With Proportionality factor $\frac{1}{2} C_x = 40.3 \times 10^{16}$ per TEC units, and the ionospheric delay caused by 1 TECU on the first Frequency in Hz is ζ_e .

Single layer Mapping function

In the mapping function to convert Slant Total Electron Content (STEC) (STEC) to Vertical Total Electron Content (VTEC) (VTEC), H , the height of STEC, is used.[25]

$$F(z) = \sqrt{1 - \frac{R_{earth} \cos(90 - \chi_{sza})}{R_{earth} - H}} \quad (3.16)$$

With the mapping function, the VTEC values at Ionospheric pierce points can be calculated.

Correction method: Dual Frequency Receivers

The use of Dual Frequency Receivers can compensate for the first order effect. The group delay or phase advance can be corrected for.[5, 4] This is possible due to the combination of signals.³

$$\varphi_{lon-free} = \frac{f_1^2}{f_1^2 - f_2^2} \equiv_{L1} - f_2^2 f_1^2 - f_2^2 \equiv_{L2}, \quad (3.17)$$

$$R_{lon-free} = \frac{f_1^2}{f_1^2 - f_2^2} R_{L1} - \frac{f_1^2}{f_1^2 - f_2^2} R_{L2} \quad (3.18)$$

³As been presented by: <https://gssc.esa.int/navipedia/index.php/>

3.5 Electron density variation

It can be seen that the disturbance on radio wave propagation is mainly caused by the variation of ρ_e . The ionosphere hold most of the e^- and will be discussed further.

Vertical structure of the ionosphere

The ρ_e increases with increasing height, up to a certain point of maximum density. The region above and below are named the topside and bottomside profile. The profile comes from a balance of ionisation described earlier. During daytime, four layers can be observed in the ionosphere as has been described below and shown in Figure 3.4.

- **D (50 km to 90 km)**: This region absorbs much energy due to the high collision frequencies and presence of neutrals. This results at most in reduced signal strength of the wave, although a summary from [7] in [44] indicates to measurable effects. The free e^- disappear completely during the night when O_2^+ recombines back to neutral, this is when radio waves penetrate the layer.
- **E (90 km to 140 km)**: Radio wave refraction. During day and night, a thin layer forms sporadically, this is called the Sporadic E-layer. Species NO^+ , O_2^+ are dominant, N_2^+ , and O^+ secondary.
- **F1 (140 km to 210 km)**: Refraction of radio waves. Only present during the day as a result of solar radiation.[5] Combined with the E-layer it can account for 10 percent of Ionospheric time delay. [44] Species NO^+ , O_2^+ dominant, N_2^+ , and O^+ secondary.
- **F2 (210 km)**: The recombination is lower and persists during the night. This layer is most important for refraction, continuous presence and long communication paths. This layer has the highest density, resulting in the most effecting layer. Species O^+ dominant, H^+ , and He^+ secondary.

At sunrise, electron production increases due to Extreme Ultra Violet (EUV) (EUV) radiation. The E- and F1-layer are sustained by this and are going during the night. Solar activity is varying and can be described by the sunspot number, and Solar radio flux $F_{10.7}$. [6]

Latitudinal Variations of the Ionosphere

The ionosphere is not stable, its variations depend on multiple parameters. Examples of common Ionospheric irregularities are shown in (4). [69] To clearly summarize phenomena, polar-high latitude regions ($60 \text{ deg} \leq \theta < 90 \text{ deg}$) and equatorial-low latitude region ($20 \text{ deg} \leq \theta < 60 \text{ deg}$) are presented. Where θ is defined as the geomagnetic latitude. The mid-latitude is not complex compared with the other two regions, so this region will not be addressed in this thesis. Vertically propagating waves, gravity waves, can amplify strong winds moving in horizontal and

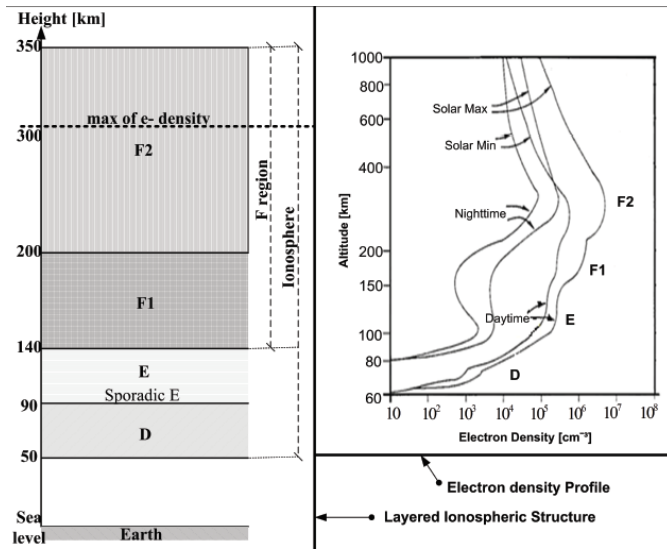


Figure 3.4: Ionospheric structure and Electron Density Profile. [48]

vertical directions and alter magnetic field lines, resulting in local changed of Electron Density in the E-layer, sporadic E.

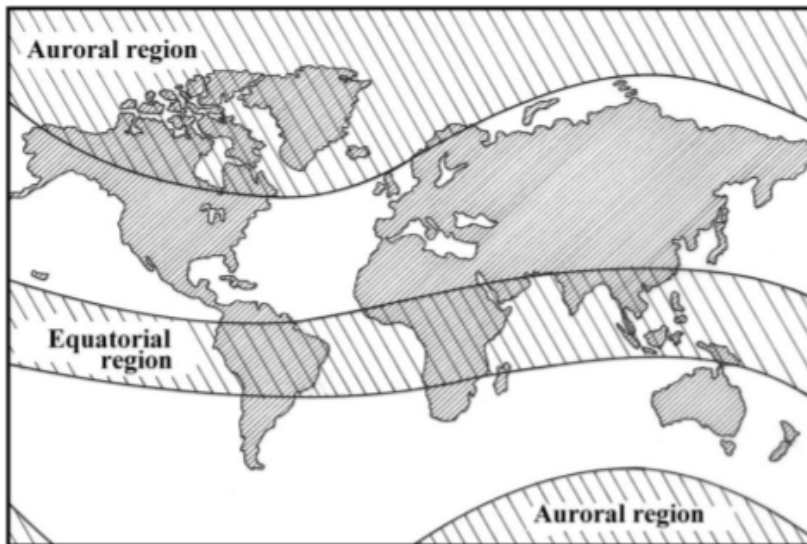


Figure 3.5: The regions of geomagnetic latitude.

Equatorial region

The generation of dynamo electric field has been described by [43]. The plasma moves perpendicular in $\vec{E} \times \vec{B}$ direction, and because the electric conductivity is E-layer $>$ F-layer during daytime, the electric field acting on F-layer plasma can be reduced there. Charge neutrality on timescale $\tau \simeq \frac{\epsilon_0}{\sigma} < 1 \times 10^6$ s. In the charge conservation equation, the time derivative can be assumed zero too:

$$\frac{\partial \rho}{\partial t} + \nabla \cdot \mathbf{J} = 0 \tag{3.19}$$

The currents of the electric field fluctuate locally, so that the total current density ($\mathbf{J}_{tot} = \mathbf{J} + \sigma \vec{E}$) becomes divergence free $\nabla \cdot \mathbf{J}_{tot}$. The wind resulting from this effect is in the direction perpendicular to Magnetic field vector (\vec{B}). To make the divergence zero, an electric field must made.[51] The ionization at F2-layer and

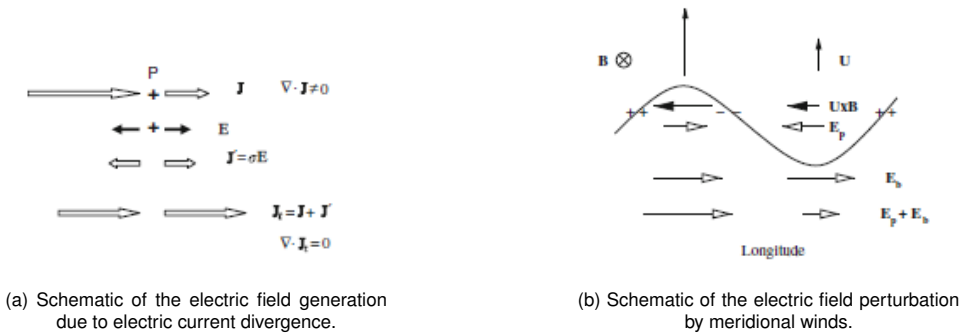


Figure 3.6: Schematic showing the Dynamo Electric Field. [43]

higher is mainly going downward by the vertical diffusion, as described in previous chapter. The ions are bound to move along Geomagnetic Field (\vec{B}), which is oriented between magnetic North and South pole. This results in the effect that vertical diffusion is held back in this region and not determined by chemical reactions.[38] The Equatorial anomaly in this region has been describes with *Equatorial electrodynamics*. Here a fountain affect causes an increased density, which form bubbles at the F-layer, as can be seen in Figure 3.7. The F2-layer peaks at around 20 deg North/South from geomagnetic equator. These bubbles move upwards during sunset and become unstable plumes of plasma. Belehaki, Stanislawski, and Liliensten also indicates there are smaller density patches, with a lifetime of 2 h to 8 hrs. This last phenomena actually is an effect of the ionosphere itself. A time evolution of this anomaly can be seen in Figure 3.8.

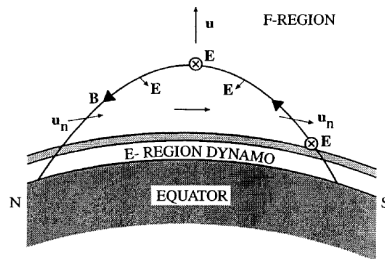


Figure 3.7: The ions and electrons are trapped by Geomagnetic Field (\vec{B}). The combination of upward $E \times \vec{B}$ plasma drift and downward diffusion causes a fountain like effect of plasma motion. Found on both sides of the magnetic equator, sometimes called the Appleton anomaly. [26]

Polar and High latitude region

At high-latitudes, occurring phenomena are for example Polar Cap Absorption (PCA) (PCA). During this phenomena energetic particles are blown by the sun during a solar proton event. The particles enter the ionosphere via Geomagnetic Field (\vec{B}) lines at high-latitude from the Magnetosphere. Note that this also increases the TEC in the ionosphere at lower latitudes, causing the reflective effect happening at lower than normal latitudes.[36] Another example is solar flares. Solar flares eject High-energy (HE) (HE) protons that enter the Magnetosphere directed along field lines into the polar D-layer, increasing ionisation. This event is called a PCA event. In [67], the results of a radar network is presented, located in high- and mid-latitude regions. Nishitani, Ruohoniemi, Lester, and Baker subtracted results into Convection, Ionospheric irregularities, Propagation analysis, Ion-neutral interactions, and MHD waves. For later research, the build-up of ionized metallic ions

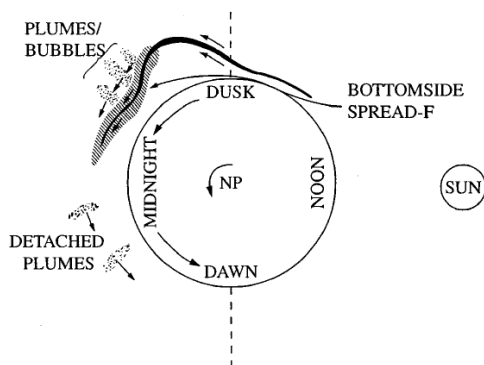


Figure 3.8: Schematic showing the evolution of density anomaly (spread F) into plasma bubbles and plumes. [26]

most likely originated from meteorites, as found in literature. Sodium, Magnesium and, Potassium resulting in temporarily disrupted radio signals.

Summary of this chapter

This chapter 3 has introduced radio wave propagation and the atmospheric effects on radio waves. Then the ρ_e variations on vertical and latitudinal scale were shown. In the next chapter 4, events of Space Weather, responses to Space Weather phenomena, and the morphology of the Magnetosphere will be given.

4 Space Weather

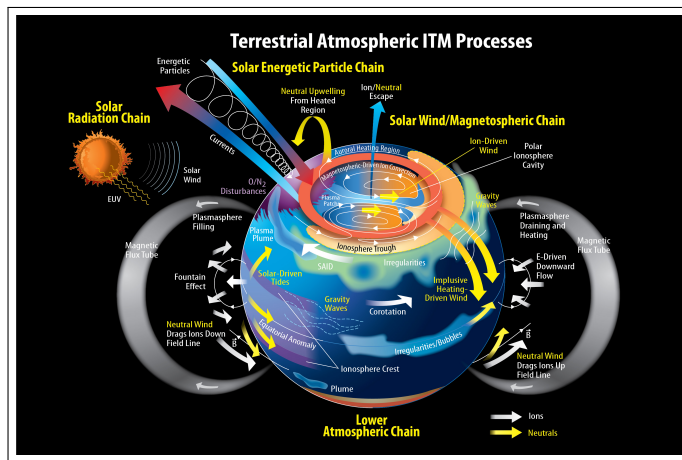


Figure 4.1: Artistic impression showing an overview of Atmospheric processes related to Space Weather. [72]

“ Space Weather phenomena are geomagnetic activity, caused as a result of the active responses of the Magnetosphere. They are affecting the propagating radio waves in the Ionosphere we are interested in. Four events of Space Weather are given in the first section. The next sections relate Magnetospheric responses to Space Weather phenomena, and gives the morphology of the Magnetosphere. The main components of Space Weather are: Solar Radiation (Energetic particles), Solar Flares, and Coronal Mass Ejections. ”

Chapter objectives:

- Identify Space Weather Events and their effect
 - Explain the morphology of the Magnetosphere
 - Identify Space Weather phenomena
-

4.1 Space Weather Events

Space weather events cause significant effect on radio wave propagation, because of their relation with electron density. The events below result in disturbances of the Ionosphere, which affect propagating radio waves in this medium. In this section the main Space Weather Events are discussed.

Ionospheric storms

Ionospheric storms, as described in subsection 4.4, affect radio waves at all latitudes. This can happen suddenly, during an Sudden Ionospheric Disturbances (SID) (SID), and causes a fadeout (referred to as Wave Fadeout (SWF) (SWF), happening suddenly or gradually). A sudden surge of energetic photons, following a solar flare, for instance, leads to an increase in the ion and electron concentrations and in the warming up of the Thermosphere, which results in the dilatation of atmospheric gas. The ions and the e^- recombine chemically, either between themselves or with neutral atoms and molecules. These reactions are rapid and balance out production so that, on the night side, the Ionosphere empties suddenly and almost completely.[36]

Solar Radiation

Electromagnetic (EM) radiation, described by the Solar constant, determines the Climate and structure of the atmosphere. During solar maximum, the fluctuations in the Ionospheric layers are amplified. The Solar wind and interplanetary magnetic field (IMF) (IMF) are having an effect on Earth's magnetic field, together forming the Magnetosphere. According to Pieper, the energy density of solar wind is six order of magnitude smaller than Electromagnetic (EM) (EM) radiation of the sun, but causes a stronger effect due to ionization of the atmosphere.

Solar Flares

Solar flares contain high-energetic UV and X-ray, which mainly ionise the Ionospheric D-layer. An increase of the ionisation and density results in a higher absorption of the propagating signal.[36] suggests that the intense radiation of X-ray are a possible indication of Solar Flares in a more frequent occurrence of SWF during solar maximum. Solar flares cause SID's and by changing the atmosphere they also increase drag on satellites in a low altitude orbit. Travel time from the Sun to Earth is 8 minutes for light, so solar flares effects start quite fast after a flare has been emitted. Hours after a solar flare, the first energetic particles arrive at Earth, ionizing and interacting with the atmosphere.

Coronal Mass Ejections

Coronal Mass Ejections are driven by internal shock waves inside the Sun, they cause geomagnetic disturbances, occurring up to three days after a solar flare.

Both the Coronal Mass Ejections (CME) and shock wave transfer energy to the Magnetosphere. This energy transfer results and accelerating energetic particles moving into the Ionosphere via the poles and auroral activity.

4.2 Effect of Space Weather Events

Scintillation

Scintillation can result in signal loss and can be seen as degradation of the image of the receiver. The Refraction causes distortion of this image. The Ionospheric Scintillation has an Equatorial and Auroral component, which are driven by the Solar EUV output, and Geomagnetic activity, respectively.[69]

Auroral activity is related to Phase Scintillation. Phase Scintillation is characterized by the standard deviation of the signal phase.[39]

According to the Australian Bureau of Meteorology quantify Weak $S_4 < 0.3$, and Strong Amplitude Scintillation $0.3 > S_4 > 0.6$, based on the fact that a value of $S_4 \geq 0.6$ can cause a *Loss of lock* on a GPS signal and 0.3 the starting value for when effects starts to occur, according to the Australian Bureau of Meteorology. To characterise Amplitude Scintillation, which is used later to quantify the results, the equation below is used. [39] Amplitude Scintillation is related to Plasma bubbles. Plasma bubbles are shown previously in Figure 3.8.

$$S_4 = \sqrt{\frac{\langle I^2 \rangle - \langle I \rangle^2}{\langle I \rangle^2}} \tag{4.1}$$

Where I is the intensity of the signal. Aarons explained equatorial irregularities as signal fading due to scintillation. [3]. A modern version of this figure was made by [55] and is shown in Figure 4.2. Figure 4.2 shows global fading due to Scintillation, in the L band. The article of Aarons and a more recent article, [55], found largest fading in the frequency range of 1 to 2 GHz (L band) to occur at maximum solar period at night time, near the magnetic equator [55].

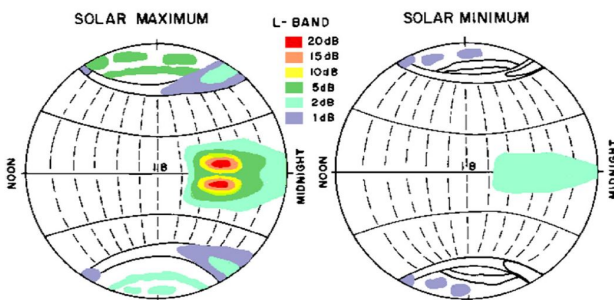


Figure 4.2: Global Signal fading due to scintillation in the frequency range of 1 to 2 GHz (L band). [55]

4.3 Morphology of the Magnetosphere

The global dynamics and structure of the Magnetosphere can largely be explained by three regions: the bow shock, Magnetopause and Magnetotail. The main controlling parameters are presented. The IMF, from the solar wind, is controlling the structure of the bow shock and has a responsive action in the form of high speed jets in the Magnetosheath. Energy storage and release in magnetic storms and substorms is strongly controlled by the orientation when the Solar wind is entering the geomagnetic field. This is shown in figure 4.3 below.

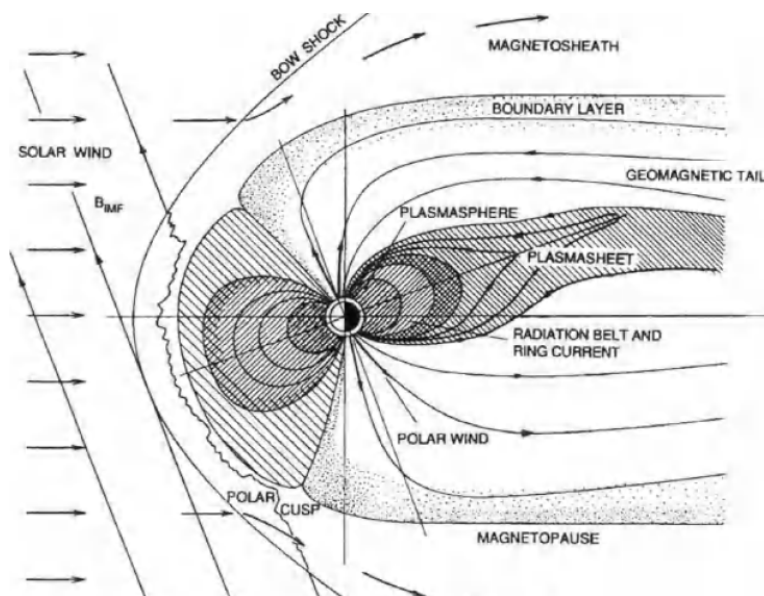


Figure 4.3: Schematic showing a cross section of the Magnetosphere. [1]

The bow shock

The solar wind transfers plasma and energy into the Magnetosphere, and sets up a global convection of plasma in the Magnetosphere. This convection is important for the transport of plasma, energizing plasma, driving waves in the plasmas, and for exhausting plasma out of the Magnetosphere.[62] It can be seen that the orienting of the IMF determines the structure of the bow shock. The bow shock heats, compresses and deflects plasma flow.

Magnetopause

The Magnetopause marks the outer boundary which balances solar wind with the Magnetospheric plasma. On low and high latitudes the boundary layer consists of a plasma and is called the plasma Mantle. The Magnetopause can be both

open or closed, implying mass transport. These are plasma jets and are directed along the Magnetopause, which might be enhanced depending on the orientation of the IMF. Thermosphere, the neutral atmosphere's upper region ($> 85\text{km}$), has an ionized portion, named the Ionosphere. There are features in Earth's magnetic field where solar-wind plasma can penetrate into the Magnetosphere along the magnetic-field lines. These are cusps and can be seen as the two intrusions of into the Magnetosphere.[62] The Magnetopause is not impermeable, and in reality solar wind plasma will cross the Magnetopause onto closed Magnetospheric field lines. This will extend the basic structure of the low latitude boundary layer described before. Both the Magnetopause and the LLBL strongly depend on the IMF and plasma conditions.

The Magnetotail

With the compression of solar wind, the Earth's Magnetosphere is compressed on the dark side, creating the Magnetotail. Within the Magnetotail two important hot plasmas reside: the ion and electron plasma sheet. The global pattern of convection in the Magnetosphere is from nightside to dayside (opposite to the direction of the solar-wind flow), and is delivering plasma into the Magnetosphere from the nightside. The Magnetotail is a reservoir of magnetic energy that powers several Magnetospheric processes. The global instabilities might produce surges of Earthward convection that occur a few times per day (Substorms), of which the occurrence is the downward ejection of magnetized plasma.[62] The magnetic flux of the tail lobes are connected to the Earth and return plasma on closed field lines towards the Earth. This forms the plasma sheet and closer to Earth, the plasma sphere and radiation belts. This is the inner Magnetosphere.

Inner Magnetosphere: Ring current and the radiation belts

The inner Magnetosphere is defined by magnetic signatures of a cold ($T_e = 1\text{ eV}$) but dense ($n_e = 5 * 10^2\text{ cm}^{-3}$) plasma and corresponds to a toroid shaped electric current that flows westwards around the Earth. During Magnetospheric storms, the particles that contribute substantially to the total current density are mainly trapped ions in energy range of **10 to 500 keV** that originate in the solar wind (He^+), the Plasmasphere and the Ionosphere (O^+).[19] During low activity periods, a weaker airglow is produced by proton impact (from the plasma sheet) on the atmosphere at latitudes slightly lower than the electron aurora. An aurora represent a dissipation of energy from the Magnetosphere. Most aurora are produced by electron impact from the electron plasma sheet. [62]

The radiation belts contain High-energy (HE) (He) ions/ e^- , which are trapped in geomagnetic field lines. The production and losses are in the Magnetotail, upper atmosphere/Ionosphere (through collisions), and in the Magnetosphere (by diffusive EM waves). The particle transport depends on EM field perturbations and is controlled by magnetic (sub)storms. The radiation belts extend from **100 to 65 000 km** and consist primarily of electrons up to a few **MeV** energy and protons of up to several hundred **MeV** energy.[62]

The *Proton belt* generally has one maximum. This Proton belt maximum corresponds to a parameter which decreases with increasing energy. The *electron belt*

has two, giving rise to the *Van Allen radiation belt*. The Van Allen radiation belt has an internal and external (or inner and outer) electron belt, with an energy close to 1 MeV.[56] Wave-particle interaction is related to various modes of plasma waves and Van Allen radiation belt relativistic e^- . Two types of plasma waves, chorus and Magnetosonic (MS) wave (also known as equatorial noise), can efficiently accelerate electrons relativistic. [56] The ring current, radiation belts and Plasmasphere partially overlap. For instance at $L = 3$, the density of the cold plasma is 1000 times higher than energetic protons (> 100 keV) whereat the protons dominated by a factor 1000. The interaction between singly charged energetic ions and the cold neutral hydrogen of the geocorona results in energetic neutral atoms, which then result in H^+ and O^+ charge exchange, having an energy between a few eV and a few hundred keV. They are not affected by magnetic or electric field forces, and therefore leave the interaction region in ballistic orbits. [19]

4.4 The origin of Space Weather Events

This section gives an overview of active responses in the Solar Wind - Magnetosphere system resulting in the phenomena of Space Weather introduced before. Detailed information can be found in [1] and is shown schematically in Figure 4.4.

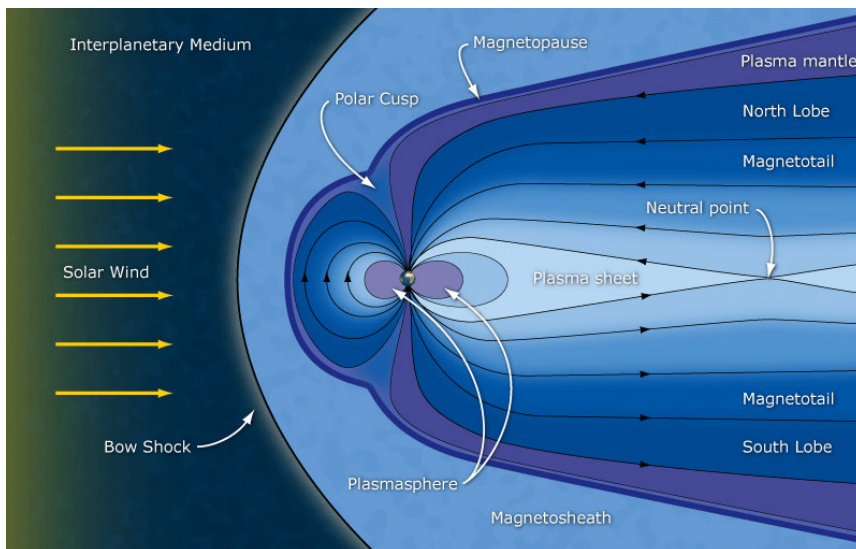


Figure 4.4: Schematic of Earth's Magnetosphere. [42]

The bow shock

Hot Flow Anomaly (HFA): The interaction of IMF discontinuity with the bow shock might generate Hot Flow Anomaly (HFA). The edge regions of plasma density and magnetic field are enhanced, the core region has reduced plasma density, which typically contains hot plasma; $T_i \sim 100\text{keV}$, accompanied by a deflecting plasma flow. According to Eastwood, Hietala, Toth, Phan, and Fujimoto, HFA lasts a few minutes, and in dramatically disrupting the solar wind dynamic pressure, they have been observed to cause changes of more than 5 Earth radii (RE) in the Magnetopause location. [54]

Shock-Bow Shock interaction: The interaction between an interplanetary shock and the bow shock leading to strong particle acceleration. This phenomenon remains largely unexplained, but there has been an event: Recently, the collision of an interplanetary shock with the Earth's bow shock on 10 August 1998 was identified as one of the rare events where detailed in situ observations of the different acceleration phases could be made. As cited from [54].

High speed Jets: The plasma regions in the Magnetosheath exhibit dynamic ion pressure (P_i), kinetic energy and/or particle fluxes. This plasma region can be amplified by its surrounding. Eastwood, Hietala, Toth, Phan, and Fujimoto found relevant parameters for the ripple-based jet formation. The distribution of known ripples (i.e. a wavelength of $1 R_{earth}$ and an amplitude of $0.1 R_{earth}$) are having a dominant amplitude to wavelength ratio. [54]

Magnetopause

Magnetic reconnection: Magnetic reconnection enables open field line formation, connected to Earth and the solar wind in both directions. There is release of magnetic energy when the field lines are reconnecting, this creates a plasma heated jet. An empirical model of Eastwood, Hietala, Toth, Phan, and Fujimoto predicts that due to solar wind, undetectable electron heating $> 1\text{keV}$ is expected. In the Magnetotail, typical values are 1keV . There is also evidence of time dependent reconnection and generation of structures, like the Flux Transfer Event, which are thought of as propagating bulges along the Magnetopause.

The Kelvin-Helmholtz instability (KHI), describes fast solar wind on the Magnetopause sides, creating velocity shear that could lead to Kelvin-Helmholtz instability (KHI). Eastwood, Hietala, Toth, Phan, and Fujimoto also shows observations providing evidence KHI could play a major role in solar wind plasma transport (from the flanks during northward IMF and when reconnection is expected to be inefficient).

Diffusive entry: In collisionless plasma, diffusion is extremely weak and would have minimal impact on transfer across the Magnetopause. However, wave-particle interactions due to instabilities could lead to diffusion, creating certain boundary layers¹.

¹ Diffusive entry of the Magnetopause could create certain boundary layers: (1) Boundary layer flows tangential to the Magnetopause, both aligned with the shocked solar wind flow on the other side. (2) Smoothly varying boundary layer velocity and density profiles. (3) Increasing boundary layer thickness with increasing distance from the subsolar point. (4) Boundary layer located on closed field lines.

Earths Magnetotail: Southward IMF

The properties of the Earth's Magnetotail depend on the solar wind [46] and references therein. In particular, the density of the plasma sheet is correlated with the solar wind density: the temperature correlates with solar wind speed, and Geomagnetic Field (\vec{B}) correlates with Geomagnetic Field (\vec{B}) in solar wind. The IMF penetration is the effect of reconnection and might exert a torque on the internal lobes, such that the northern lobe twists towards dawn or dusk, for respectively positive and negatively torque.

Magnetospheric convection: Magnetic reconnection between closed Magnetospheric field and IMF changes the magnetic conductions. It leads to the formation of open field lines. Via solar wind, and unbending of kinked magnetic field, plasma is transported poleward, through the cusps and into the Magnetotail. This leads to the accumulation of magnetic flux on open field lines in the tail, the basic convection pattern is known as Dungey cycle.

Substorms: Continued dayside reconnection during southward IMF leads to an accumulation of open flux in the Magnetotail, and storage of energy in the lobe magnetic field. This accumulated undergoes release as Magnetospheric substorms.[54] also finds that:

1. This process involves the formation of a second neutral line closer to Earth.
2. The formation results in Earthward plasma injection of and leads to bright auroral displays and associated disturbances to ground based magnetometer the auroral substorms.
3. This open field area, the polar cap, varies between flux rates on day- and nightside (expanding/Contracting Polar Cap paradigm).
4. Polar cap size and location of the open/closed field line are approximated by the auroral oval.

Storms: Storms are characterised by energization of the radiations belts and enhanced particle fluxes, which cause a depression in the equatorial magnetic field, measured by the geomagnetic index (Dst). Storms result from plasma convection into the inner Magnetosphere. Corresponding solar wind conditions create solar wind structure, such as **CME** (Responsible for large geomagnetic disturbances, depending on solar wind speed, field strength and southward IMF) and interaction regions. Note that the connection between storms and substorms is not straightforward, in the sense that a storm does not necessarily consist of a series of elemental substorms, and in fact the di-polarization of the Magnetotail by the enhanced ring current may inhibit substorm onset. [54]

Earths Magnetotail: Northward IMF

During intervals of low geomagnetic activity, observations show that the plasma sheet can become significantly colder and denser. This so called Cold Dense Plasma Sheet (CDPS) (CDPS) has densities of 1 cm^{-3} , and temperatures $<1\text{ keV}$ and is found on closed field lines, with larger densities nearer the flanks than in the Magnetotail center. The CDPS does not contain cold O^+ ions and so is not thought to be sourced from the Ionosphere.[54] In fact, the plasma content of the CDPS increases during intervals of northward IMF with the best correlation

occurring when the IMF parameters are averaged *9hrs* before the plasma sheet observations. As such, the CDPS is caused by solar wind plasma entering under northward IMF conditions. In a case study examining the response of the Magnetosphere to more than *32hrs* of northward IMF, the CDPS was observed for more than *30hrs*. [54]

Summary of this chapter

This chapter 4 has shown events and responses to Space Weather phenomena, and has given the morphology of the Magnetosphere. In chapter 5 an Electron density model is presented. In chapter 7 an outlook, recommendations, and conclusions are given.

5 Electron Density Model

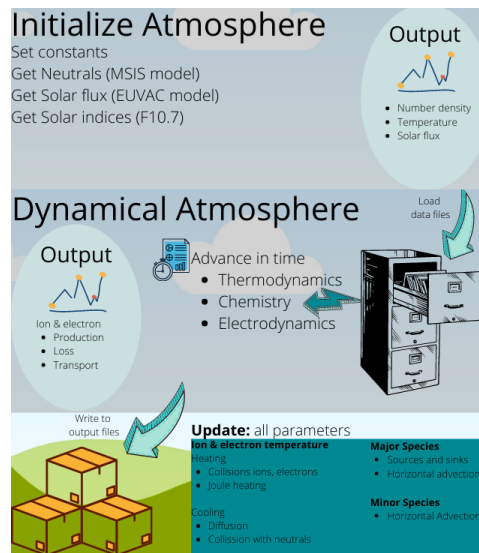


Figure 5.1: Schematic of the used Ionospheric ray tracing.

“This chapter presents details on the model, which is a physics-based electron density model to describe the evolution of electron density in Earth’s atmosphere and the interaction of Solar radiation to Earth’s atmosphere. section 5.1 introduces the model, after which general equations are shown in section 5.2. Key parameters and boundary conditions are shown in section 5.3. These are used as input for the model. section 5.1 expresses the desired output and constraints on the model. A review and validation against other models is given in section 5.4.”

Chapter objectives:

- To refresh memory about variables and formulas used in the model
 - Explain the main components of the model
 - Identify other Space Weather and Electron Density models
-

5.1 Introduction of the model

This chapter shall describe the model in a functional way, building upon earlier described theories or refers to literature. The objective of an electron density model is finding an expression for Electron number density and its change over time. With Electron number density, the delay and distortion of radio waves can be found. This is described in section 6.3, where geometric ray tracing is used.

The physical processes which drive the dynamics of the atmosphere is the Sun. Solar irradiance from the Sun ionises atmospheric species mainly in the EUV spectrum. The neutral composition of atomic and molecular species is changed by Solar radiation and the geomagnetic field, which are present continuously. Thus, the main drivers which are needed are shown below. This also requires a numerical approach to solve the equations.

1. A neutral composition of the atmosphere
2. Solar radiation
3. Electrodynamics ($\vec{E} \times \vec{B}$ drift of ionospheric plasma)
4. Chemical reactions

To build an electron density model, local thermodynamic equilibrium and Hydrostatic equilibrium are assumed. Both are used with the ideal gas law. Hydrostatic equilibrium describes a force balance of gravity and a vertical pressure gradient, as introduced in Equation 2.2 and explained in subsection 6.1. The model uses atomic and molecular species, as listed below. E. g. Helium is shown as He and He^+ , where He^+ is the ionized state of He.

- **Atomic:** H, He, N, O, and their ionized state: H^+ , He^+ , N^+ , O^+ .
- **Molecular:** N_2 , NO, N_2 , O_2 , and their ionized state: N_2^+ , NO^+ , N_2^+ , O_2^+ .

No existing model covers a full detailed description of SWI, atmospheric effects, and also provide a short-term forecast. Multiple literature sources are needed to cover all components. Focus lies on describing an electron density model and how it can be used in a short-term forecast. In addition the main components are described in detail, and validated against existing literature. Advantages and disadvantages are shown in section 5.4

5.2 General equations of the model

The model is mainly based on the continuity, momentum, and thermodynamic equation, these are presented in the next sections. These are conservative equations for the ions and electrons.

Conservation of mass (Continuity equation)

Continuity equation

The continuity equation describes the time rate of change of Number density. It consists of a production rate (photo ionization and chemistry) and loss rate (chemistry).

$$\frac{\partial n_i}{\partial t} + \nabla \cdot (n_i v_i) = \text{Production} - n_i \text{Loss} \quad (5.1)$$

Conservation of momentum (Momentum equation)

Ion momentum equation

$$\frac{\partial v_i}{\partial t} + v_i \cdot \nabla v_i = -\frac{1}{\rho_i} \nabla P_i + \frac{e}{m_i} E_s + \frac{e}{m_i C} v_i \times \vec{B} + g \quad (5.2)$$

$$-v_{i,n}(v_i - v_n) - \sum_j v_{i,j}(v_i - v_j) - v_a(V_{i,\parallel})V_{i,\parallel} \quad (5.3)$$

Electron momentum equation (along \vec{B})

$$0 = -\frac{1}{n_e m_e} b_s \frac{\partial P_e}{\partial S} + \frac{e}{m_e C} E_s \quad (5.4)$$

Conservation of energy (Thermodynamic equation)

The thermodynamic equation describes the change of temperature (T) over time (t), written as $\frac{\partial T}{\partial t}$. The components in the equations below contain on the left the time rate of change and thermal conductivity. On the right side of the equation shows the heat flux components.

The components of the heat flux of the ions and electrons both consists of three components. The ion heat flux consists of Ion-Neutral heat flux (Q_{in}), Ion specific heat flux (Q_{ij}), and Ion-electron heat flux (Q_{ie}). The electron heat flux consists of Electron-neutral heat flux (Q_{en}), Electron-Ion heat flux (Q_{ei}), and Photon-Electron heat flux (Q_{phe}).

The ion and electron thermodynamic equations are shown below.

Ion thermodynamic equation

$$\frac{\partial T_i}{\partial t} + v_i \cdot \nabla T_i + \frac{2}{3} T_i \nabla \cdot v_i + \frac{2}{3} \frac{1}{n_i \kappa_e} \nabla \cdot Q_i = \underbrace{Q_{in} + Q_{ij} + Q_{ie}}_{\text{ionheatflux}} \quad (5.5)$$

Where the ion temperature is in thermal balance for H, He, O and e^- .

Electron thermodynamic equation

$$\frac{\partial T_e}{\partial t} - \frac{2}{3} \frac{1}{n_e k_B} b_s^2 \frac{\partial}{\partial S} \kappa_e \frac{\partial T_e}{\partial S} = \underbrace{Q_{en} + Q_{ei} + Q_{phe}}_{\text{electron heat flux}} \quad (5.6)$$

Transport (motion of the plasma)

The Electric field vector (\vec{E}): in [15] it is assumed that the Electric field vector (\vec{E}) is solvable with Pedersen-Hall. Pedersen-Hall = Neutral winds - gravity. Model Geomagnetic Field (\vec{B}), including $\vec{E} \times \vec{B}$ drift in longitude and altitude.

To solve dynamics with a numerical scheme by a forward/backward time stepping method. Huba, J. D. and Joyce, G. and Fedder, J. A. first calculates the plasma motion parallel (\parallel), then perpendicular (\perp) alongside \vec{B} ((1) motion along \vec{B} , (2) motion transverse to \vec{B}). This is advection and diffusion and the corresponding formulas can be found in [50].

Transport of O^+ , described by the number density, ambipolar diffusion and $E \times \vec{B}$ drift to find the ion velocity.

Mean molecular weight

A mean molecular weight for the species can be found by using the molecular weight of each species and the Ion number density.

$$M = \sum \frac{M_i n_i}{n_i} \quad (5.7)$$

The rate of loss of ionized species, as they recombine to neutral species, are listed in the table below. The recombination coefficients rates are taken from [2].

Table 5.1: Recombination rates for molecular ions, as input for the ionization balance.

Chemical reaction	Reaction rate [$cm^3 s^{-1}$]
$H^+ + e^- \rightarrow H$	$4.43 \times 10^{-12} / T_e^{0.7}$
$He^+ + e^- \rightarrow He$	$4.43 \times 10^{-12} / T_e^{0.7}$
$N_2^+ + e^- \rightarrow N_2$	$4.43 \times 10^{-12} / T_e^{0.7}$
$O^+ + e^- \rightarrow O$	$4.43 \times 10^{-12} / T_e^{0.7}$
$N_2^+ + e^- \rightarrow N_2$	$1.80 \times 10^{-7} / T_e^{0.39}$
$NO^+ + e^- \rightarrow NO$	$4.20 \times 10^{-7} / T_e^{0.85}$
$O_2^+ + e^- \rightarrow O_2$	$1.60 \times 10^{-7} / T_e^{0.55}$

5.3 Dynamics of the model

This section first introduces solar and geomagnetic input of the model, then atmospheric related input. To capture the solar spectrum and the solar cycle variation, an index for the solar radio flux and Solar irradiance are needed. Ionisation of the atmosphere is primarily due to Solar radiation in the EUV spectrum. Next, the solar proxy are shown and which is used in our model.

Geomagnetic activity results of the solar cycle. The geomagnetic index used to represent the activity are a_p and its linearised version. The a_p is derived of observed geomagnetic activity every 3 hrs between specific latitudes (48 deg and 63 deg). The D_{st} is used in modelling geomagnetic storms as it represents the strength of a Magnetospheric current.[30]

Difference in daytime and night-time of atmospheric density explains the diurnal and polar characteristics. There is a downward vertical velocity causing light species to be present in upper regions, and heavier species more downward.

Between 90 and 125×10^3 m altitude, there is a significant amount of diffusion present. This is due to density variations caused by the Solar, geomagnetic, and time-based variations like the diurnal profile. Using the Hydrostatic equilibrium, a corrected temperature and density is derived. When the 24 hrs rotation of the Earth is taken into account, with highest Solar Zenith Angle at around Noon, the diurnal variation can be estimated. There also is a semi-annual variation, which is most likely an effect of Solar radiation, Joule heating, and winds on macroscale i. e.(meridional transport).

Solar input

Solar irradiance measurements are useful in modelling e.g.atmospheric Electron number density and Geomagnetic storms, as the index is shown useable.[30]. The solar spectrum is broad, covering e.g.X-ray (1 – 170 Angstroms) and EUV (170 – 1750 Angstrom). In the EUV spectrum, there is enough energy to ionize neutral

species in the atmosphere. [50] A proxy is derived from measurements. Proxy used in other research are shown in the overview of other models in section 5.4.

In our model, the proxy $F_{10.7}$ is used. This proxy describes the solar radio index $F_{10.7}$ and has strong correlation with the solar cycle variations. The $F_{10.7}$ represents the EUV spectrum, which is the spectrum most relevant for ionisation. The physical units of $F_{10.7}$ are $\text{W m}^{-2} \text{Hz}^{-1}$, or in solar flux units, where $1 \text{ sfu} = 1 \times 10^{22} \text{ W m}^{-2} \text{Hz}^{-1}$. The $F_{10.7}$ is also an output parameter of the NRLMSIS-00 model.

Besides the proxy $F_{10.7}$, there are others. The $S_{10.7}$ covers solar chromospheric EUV emission (Thermosphere and O_2 absorption). The $M_{10.7}$ covers far Ultra Violet (UV) (UV) photospheric emission in the Schumann-Runge spectrum (lower thermosphere and O absorption). The $Y_{10.7}$ covers X-ray and *Lyman* – α (Mesosphere). The solar radio index $F_{10.7}$ is derived of Solar irradiance measurements.

In [2], the spectrum was divided into 37 wavelength bins, of which 17 specific spectral lines, and 20 wavelength bins (5 to 105 nm). The Cross sections for ionization and absorption processes of atomic and molecular Oxygen and Nitrogen are shown in the tables at the appendix. When the absorption and ionization cross sections are used, shown in Appendix B. The resulting Solar Flux values are based on the EUVAC model.[12].

The ionization and absorption cross sections is essential for plasma calculations, or more precisely, for electron-impact ionization. This cross section has a direct and indirect component, where the direct component takes electron ejection into account and indirect is ionization of the atom or molecule shells to an unstable state, where it emits or ejects a photon or electron, respectively. The online database[74] of the Physical Measurement Laboratory [75] shows details atmospheric species. The cross sections of molecular ions cover the electron-impact ionization for a broad range of molecules and atoms. [16] it is not used in this research, but suggests recommendations for further research on data standardization. The standardization used by them is based on their Binary-Encounter-Bethe model, which offers a simple equation for the ionization cross sections of molecular species, and provides reliable output for low- and high-energy impacts. They introduce the topic of high-energy impact of e^- on molecules and atoms. They also are often used as reference for their cross sections data on Incident electron energy, which can be searched in their database [74] as Incident energy (Temperature) in eV. This is like answering the question "Which cross sections has particle X at a Temperature of 14 eV?" Their database can be found online. [73]

The Solar reference spectrum ($f(\lambda)$) is calculated by using a modified reference flux (f_{ref})

$$f(\lambda) = f_{ref} \left(1 + A(\lambda) \left(\frac{F_{10.7+} + \langle F_{10.7} \rangle}{2} - 80 \right) \right) \quad (5.8)$$

Where $\langle F_{10.7} \rangle$ is an 81-day average of the daily Solar Radio flux index ($F_{10.7}$). Furthermore, a scaling factor $A(\lambda)$ is used. The Lambert Beer law, chapter 2, (2.20), is then used to calculate the Solar flux spectrum (Intensity I) in each spectral interval at each height level. Calculate the **Optical Depth**: As light from the sun passes through the earth's atmosphere, some of the solar radiation is absorbed.

Solar time

To model the hourly values of the Solar irradiance, the position of the Sun is assumed to start at its zenith at Noon (12 O'clock) The term *zenith* is one of the terms for an observer. The zenith is the direction pointing upward, as the horizon is the direction pointing straight ahead.

To correct for the location and local meridian. The declination (δ) angle, the latitude (ϕ), and the *hour angle* (ω) are used to calculate the elevation angle (α) of the Sun at the current time. Where the hour angle describes the rotation of the earth between current solar time and solar noon. The Solar declination angle (δ) is describes an orbit related to Earth and its axial tilt, as it is the angle of the sun relative to the earth's equatorial plane and a given day of the year (d). This angle varies between 0° (autumnal equinoxes), and 23.45° (summer solstice).

$$\delta = \sin^{-1}(\sin(23.45) \sin(\frac{360}{365}(d - 81))) \quad (5.9)$$

$$\alpha = \sin^{-1}(\sin \delta \sin \phi + \cos \delta \cos \phi \cos \omega) \quad (5.10)$$

The time (τ), at which the sunrise and sunset are occurring (in Standard Time) uses the sun's declination and local latitude.

$$\tau_{sunrise} = 12 - \frac{\cos^{-1}(-\tan \phi \tan \delta)}{15^\circ} - \frac{TC}{60} \quad (5.11)$$

$$\tau_{sunset} = 12 + \frac{\cos^{-1}(-\tan \phi \tan \delta)}{15^\circ} - \frac{TC}{60} \quad (5.12)$$

Atmospheric input

Atmospheric input captures the concentration of atmospheric species with the number density. The n and T are introduced below. Atmospheric chemistry are based on the information shown in [9], where a clear explanation is given. The reaction scheme of major sources and sinks (N_2^+ NO^+ O_2^+) are shown schematically in the appendix (Figure A.1). Atmospheric winds are based on the HWM model. The HWM model describes variation of diurnal to semi-diurnal scale in the Thermosphere, and a transition from summer to winter above 140 km. [40, 53, 13] The model provides zonal and meridional winds, where it has latitude, longitude, altitude, time, and 3 hrs a_P index as input. Further below are the NRLMSIS model and International Geomagnetic Reference Field (IGRF) introduced.

The ionospheric parameters are derived using SAMI2 model Huba, J. D. and Joyce, G. and Fedder, J. A. and Abdu. The Hydrostatic equation (introduced in Equation 2.2), together with the divergence free Electric current density (J) can be used in the Continuity equation for the ions, to find a steady state velocity.

$$\frac{\partial n_i}{\partial t} + \nabla \cdot (n_i u_n) = -A n_i - B n_i \quad (5.13)$$

$$\nabla J = e^- \nabla \cdot |n_i (u_i - u_e)| = 0 \quad (5.14)$$

The plasma is assumed to be charge neutral ($n_i = n_e$). The chemical loss and production effects are retained via an effective recombination. (5.13) and (5.14) are then solved numerically.

The Ion number density is derived, similar as in [17, 28, 60]. The Ionospheric Electron number density at the top is $O^+ + H^+$. [24, 41]. The electron motion is assumed in a steady state, meaning the electrons are neither acceleration or slowing down. Charge neutrality assumes the total electrons and ion charges to be zero. The Ion velocity is no longer needed as $J \times \vec{B}$ equals the Ion velocity terms.

$$J \times \vec{B} - \rho_i v_{i,n}(U - V) - \rho_e v_{en}(U_e - V) = 0 \quad (5.15)$$

Where the term $\rho_e / \rho_n v_{en}(U_e - V)$ may be neglected because the density of e^- is significantly smaller than the density of neutrals ($\rho_e \ll \rho_n$). The continuity eq are calculated for the most dominant species (O, O_2, N_2) A mixing ratio of the species is used ($\chi_i = \frac{n_i}{den}$) in the calculation of the diffusion term. All other ion species are calculated without this term, which results in a transport effect.

NRLMSIS-00

The n and T are calculated with the NRLMSIS-00 (Mass Spectrometer Incoherent Scatter) model. As cited from their description: "*The Mass-Spectrometer-Incoherent-Scatter model describes the neutral temperature and concentration as number density of He, O, N₂, O₂, Ar, H, and N. The model is based on earlier work of [21]*". NRLMSIS-00 is an empirical model:

1. Below 72.5 km the model is mainly based on zonal average temperature and pressure.
2. Below 20 km, this model is based on averages from National Meteorological Center (NMC) and pitot tube, falling sphere, and grenade sounder rocket measurements.
3. Above 72.5 km, this model is based on data derived from space shuttle flights and newer incoherent scatter results.

More information on the MSIS model can be found online. [68] It is also given that the MSIS model uses the indices $F_{10.7}$ and a_p . The calculation of atmospheric density is divided in a lower region (between 90 km and 105 km) and upper region (above 105 km). A semiannual density variation is described in the Thermosphere, where heat and energy due to Solar Radiation above 120km are the cause. Turbulent mixing is assumed to predominate, and diffusion dominates at higher altitudes.[30]

International Geomagnetic Reference Field (IGRF)

The magnetic field is defined by the D , Horizontal Intensity (H), Total Intensity (F), D , and I . [70], [71]

Since geomagnetic field is a vector field, at least three elements (components) are necessary to represent the field. The elements describing the direction of the field, D and I , are measured in units of degrees. The D is the angle between magnetic north and true north, positive when the angle measured is east of true north and negative when west. The I is the angle between the horizontal plane and the

total field vector. Elements describing the field intensity is the total intensity (F), horizontal component (H), vertical component (Z), and the north (X) and east (Y) components of the horizontal intensity. These elements are generally expressed in units of nanoTesla (10^{-9} Tesla / 10^{-5} Gauss or 1 Gamma in CGS). Combinations of the three elements frequently used in geomagnetism are HDZ, XYZ and FDI.

Principal equations relating the values of the elements are as follows:

$$F = \sqrt{X^2 + Y^2 + Z^2} = \sqrt{H^2 + Z^2}, \quad (5.16)$$

$$H = F * \cos(I), \quad Z = F * \sin(I), \quad X = H * \cos(D), \quad Y = H * \sin(D) \quad (5.17)$$

Table 5.3: Overview of existing electron density model input and output

Model	:	Input	Output
SAMI	:	ion species, $F_{10.7}$	n_e, n_i
NeQuick	:		TEC
IRI	:	$F_{10.7}$, geomagnetic indices	n_e, n_i, T_e, T_i
TIEGCM	:	30 fields	

5.4 Overview of other models

This section lists other known electron density and Space Weather models. Both theoretical and empirical models are discussed in this section.

Theoretical models are based on physics. An understanding of the processes will be easier with these models. Empirical models based on observations need an analysis of data instead of a theoretical approach. An understanding of the real atmosphere might be more difficult, but it is expected that empirical models produce an acceptable model quicker. A combination of both is a semi-empirical model and should be able to couple different components.

The section presents first an overview of existing electron density models in table 5.3. Then other models will be described in more detail. In [44] details of choices are shown when modelling Ionospheric effects on radio waves. Belehaki, Stanislawski, and Liliensten has made an overview of Ionosphere-Thermosphere models in his article. [36]

SAMI SAMI2/3 solves the continuity, momentum and thermodynamic equations for ions and e^- in an offset, tilted magnetic dipole coordinate system.[15, 14, 35, 34, 50, 64] The SAMI2/3 model has its chemistry presented there and are used to solve the continuity equation.

NeQuick The NeQuick model calculates the TEC with a bottom side and top side value, and five semi-Epstein layers. Output of NeQuick is as a function of height, up to 20.000km, latitude, longitude, solar activity, month and in local time.[36]

IRI IRI gives a description of the monthly averages of electron density, electron temperature, ion temperature and ion composition in the altitude range 50 – 2000km for the Earth[10, 11]. Its output depends on the spatial and temporal coverage, which is retrieved from databases, which are used modular, giving IRI the possibility turning certain effects on or off. <http://nssdc.gsfc.nasa.gov/space/model/models/iri.html> The International Reference Ionosphere, where contact person would be a familiar name, Dieter Bilitza. This Empirical standard model of the Ionosphere, based on all available data sources, as is described here, uses only the current date and time as model input. Model output would be the electron and

ion densities, *TEC*, ion and neutral temperatures, equatorial vertical ion drift and some other variables.[36]

TIEGCM On the domain of Global circulation model, semi empirical and its output has 30 fields.[36, 47, 65]

Solar model

In Table 2 of [23], NRLEUV is validated against other Solar EUV irradiance models, namely EUVAC (also used in this model), and SOLAR2000. The NRLEUV Solar EUV model is explained detailed in [18], it ranges between 5 – 120 nm in an almost continuum 1474 bin size. The EUVAC model, used in this thesis, originates of [12]. For future research these different Solar EUV models can be compared.

Summary of this chapter

This chapter 5 has presented the input and output of the electron density model. In the last section, other Space Weather models are listed. In chapter 7 an outlook, recommendations, and conclusions are given.

This page intentionally left blank.

6 Results

“This chapter presents the modelled neutral atmosphere and Solar model in section 6.1. Scintillation measurements done by the Netherlands Armed Forces during one of their missions is shown in section 6.2. Both will be used in section 6.3, where atmospheric effects of the Troposphere and Ionosphere are shown.”

Chapter objectives:

- Provide highlights of the results of the the electron density model
 - Provide highlights of the scintillation measurements
 - Provide atmospheric effects and operational frequency conditions
-

6.1 Model results

The main drivers of section 5.1 are modelled in this section. The two figures of subsection 6.1 cover the neutral atmosphere in hydrostatic equilibrium. These show the Number density and the Temperature in units of K of electrons, neutral and ionized atmospheric species, T_e , T_n , and ions T_i , respectively.

Next, subsection 6.1 shows the Solar radio flux index over 4 years in Figure 6.3. Solar radiation is shown in a global plot in Figure 6.6. The change in time of atmospheric species are shown in subsection 6.1. The results are shown to give a better understanding of how the model results and measurement data are compared in section 6.3.

Hydrostatic equation

In Figure 6.1 the modelled Number density of the neutral atmospheric species are shown. The value of NO has been calculated with O_2 , N_2 , and T , as has been done before.[13] The Number density values are comparable to those found in

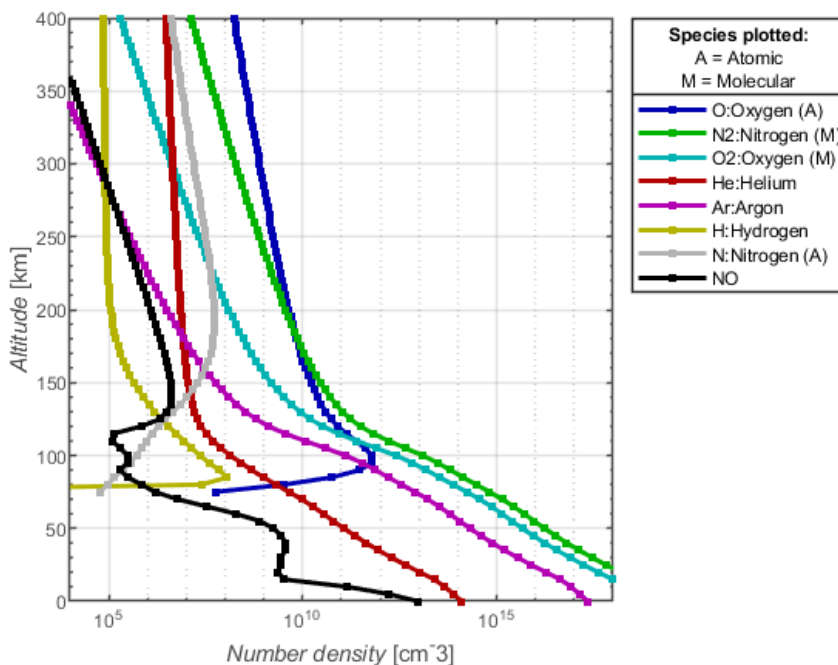


Figure 6.1: The vertical distribution of the number density of atmospheric species are shown. The measurement data of the NRLMSISE-00 atmosphere Model are used as input. [68]

literature are shown, e. g. Figure 2.4. These values can be used as a starting point for the next few steps.

Figure 6.2 shows atmospheric Temperature in units of K for neutral species, ions, and electrons as function of the height. The Ion temperature is seen to

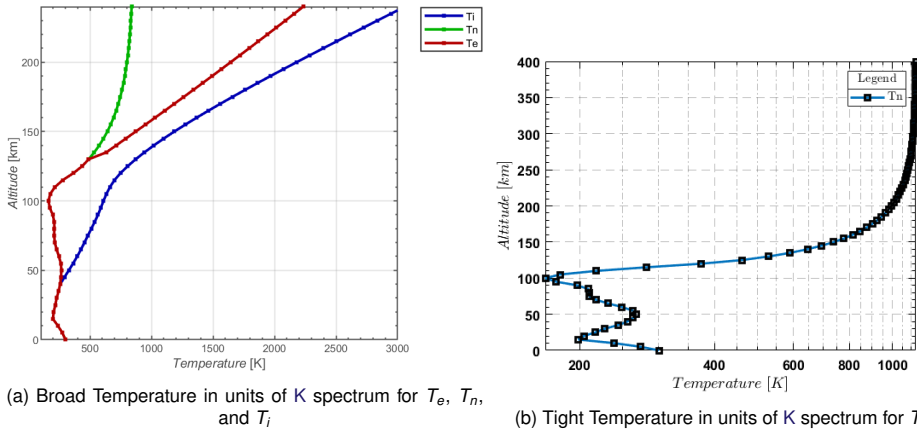


Figure 6.2: This figure shows the vertical distribution of modelled temperature of neutral and ionized atmospheric species and electrons.

be at a higher value than Electron temperature, especially at lower altitudes. The Electron temperature is following the T until it reaches a higher altitude. The figure shows values comparable to those found in literature, e.g. Figure 2.3. The dent at the Mesosphere and Mesopause of Figure 2.3 is visible for Neutral temperature and Electron temperature.

Initialisation of the Solar EUV model

This section first shows the proxy $F_{10.7}$ representable for solar radio flux in Figure 6.3 and how this is used in the ionization of atmospheric species, Figure 6.4. The Figure 6.5 shows the cross section of O , O_2 , N , and N_2 when an Elementary Charge in C ionizes them by impact. The global Solar irradiance is shown in Figure 6.6.

Before the Solar radio flux index is shown in Figure 6.3, a brief recap of subsection 5.3 on the dynamics of the modelled Solar irradiance. This proxy Solar radio flux is derived of Solar irradiance measurements and is representable for the EUV spectrum. The Solar irradiance spectrum was divided into 37 spectral wavelength bins. These bins contain 20 wavelength in nm bins (5 nm to 105 nm) and 17 specific spectral lines. The absorption and ionization cross sections for the atmospheric species are used in the Solar irradiance calculation. The $\langle F_{10.7} \rangle$

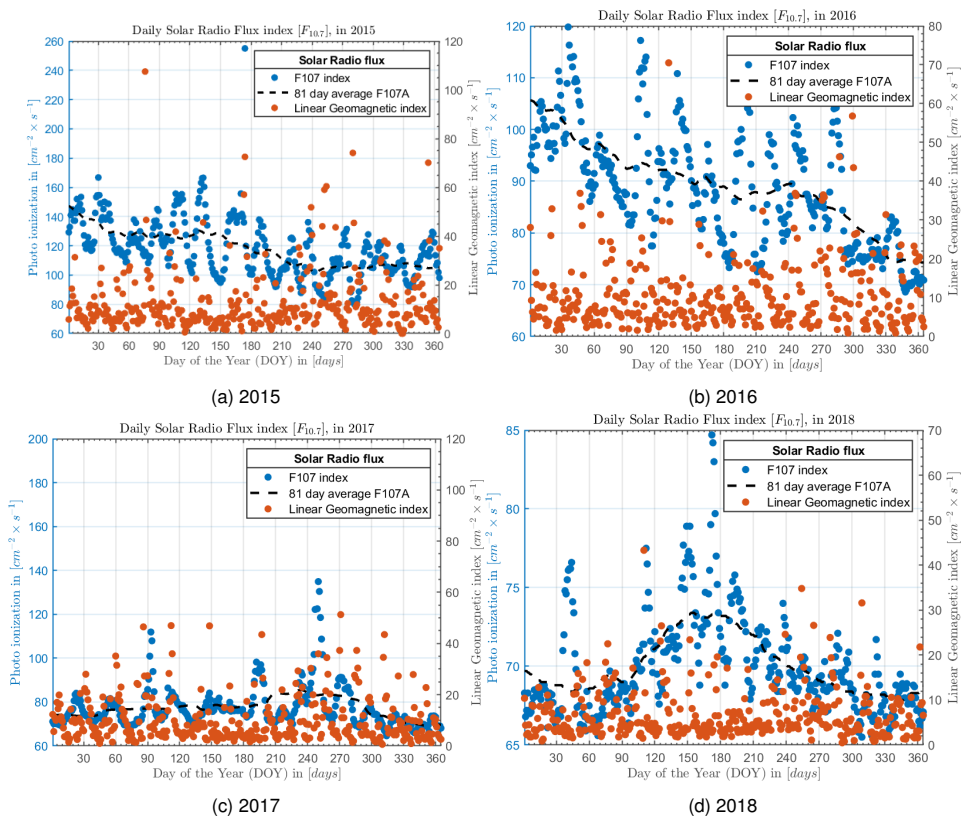


Figure 6.3: This figure shows the modelled proxy representable for the Solar Radio Flux Index. Each figure represents a full year of Solar radio flux and Linear Geomagnetic index, with their values on the left and right y-axes, respectively. The 81 day average of $F_{10.7}$ is shown by $\langle F_{10.7} \rangle$.

81 day average and $F_{10.7}$ are fluctuation in each year, where 2020 and 2020 show

relatively high and low values in. The $F_{10.7}$ and Linear Geomagnetic index have not been evaluated against other variables.

The ionization rate due to Solar irradiance is shown in figure 6.4. The ionization

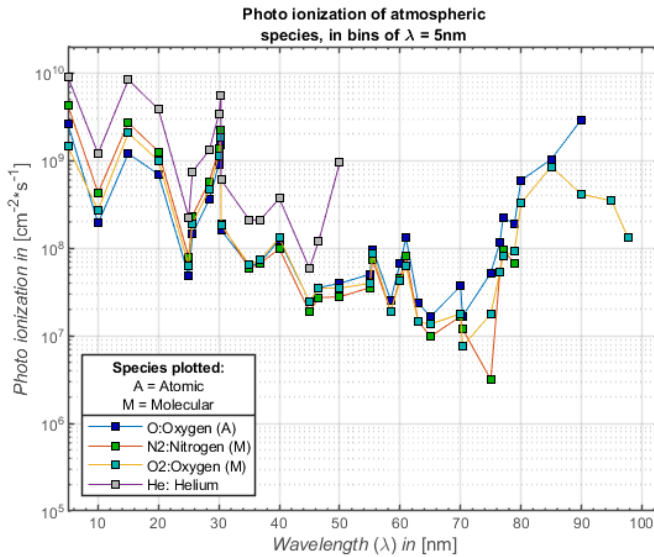


Figure 6.4: Ionization rate of atmospheric species as function of wavelength in nm in the EUV spectrum. This builds upon the atmospheric number density and Solar radio flux shown previously.

rate of Atomic Oxygen, Molecular Oxygen, Molecular Nitrogen, and Helium shows a decrease when the wavelength in nm reaches the region of 60-70 nm. This indicates that a peak of maximum photo ionization occurs at this region due to absorption of Solar irradiance. The modelled Solar irradiance covers the EUV spectrum, with peak absorption at 60 to 70, which is what would be expected. In Figure 2.6 the Solar radiation depth is shown up until 300×10^9 m, with photo ionization at 0-125 nm. The penetration height of this region has its maximum at 60-80 nm, which makes an agreement with our modelled wavelength in nm region.

The ionization cross section is shown for different Temperature in units of K values in Figure 6.5 for O, O₂, N, and N₂. Peak values are found at Temperature in units of K values around 100 eV for all plotted species. The molecular ions show higher cross sections compared to atomic ions of the same species. Which is what would be expected as molecules are normally larger than atom.

In Figure 6.6 the modelled global Solar irradiance in 2020 is shown. A world map has been used as bottom layer for this fancy plot. Contour lines of the Solar flux are shown with a jet-spectrum between low (blue) and high (red) Solar flux values. The figure actually is a capture of a frame, as it has been used for a gif-file. The diurnal variation can be seen by the maximum spot, in Figure 6.6. The next frame would change as the Solar time changes. The Solar time is introduced in 5.3.

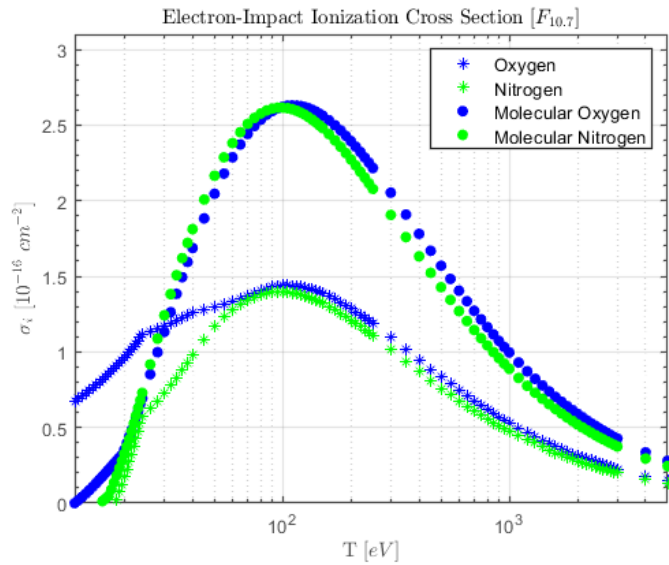


Figure 6.5: This figure shows the electron-impact cross section of atmospheric species as function of Temperature in units of K.

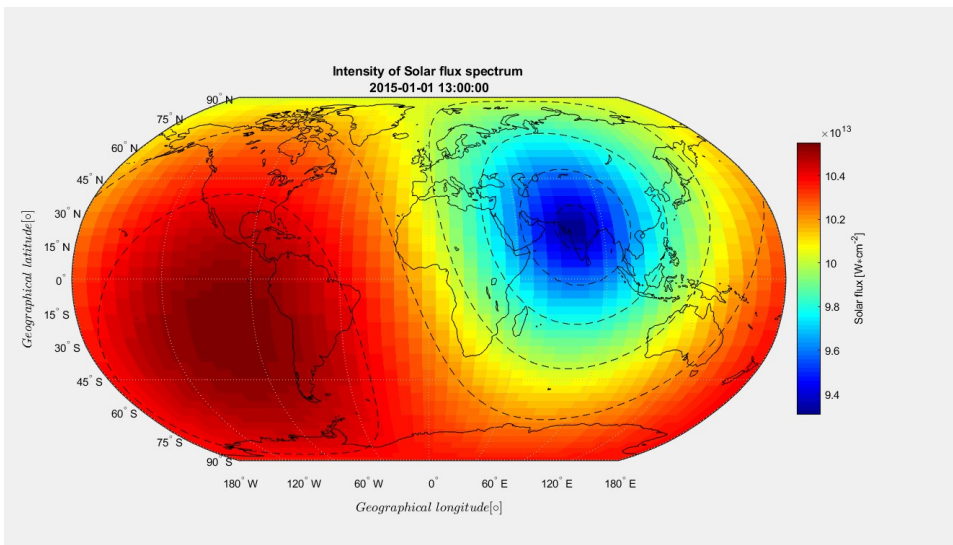


Figure 6.6: Figure shows the modelled Solar irradiance. The irradiance covers EUV spectrum as the proxy of the Solar radio flux was used. The photo ionization cross sections of atmospheric species are combined with up-to-date Solar radio index.

Atmospheric species

In Figure 6.7 and Figure 6.8 the modelled neutral and ionized atmospheric species are shown.

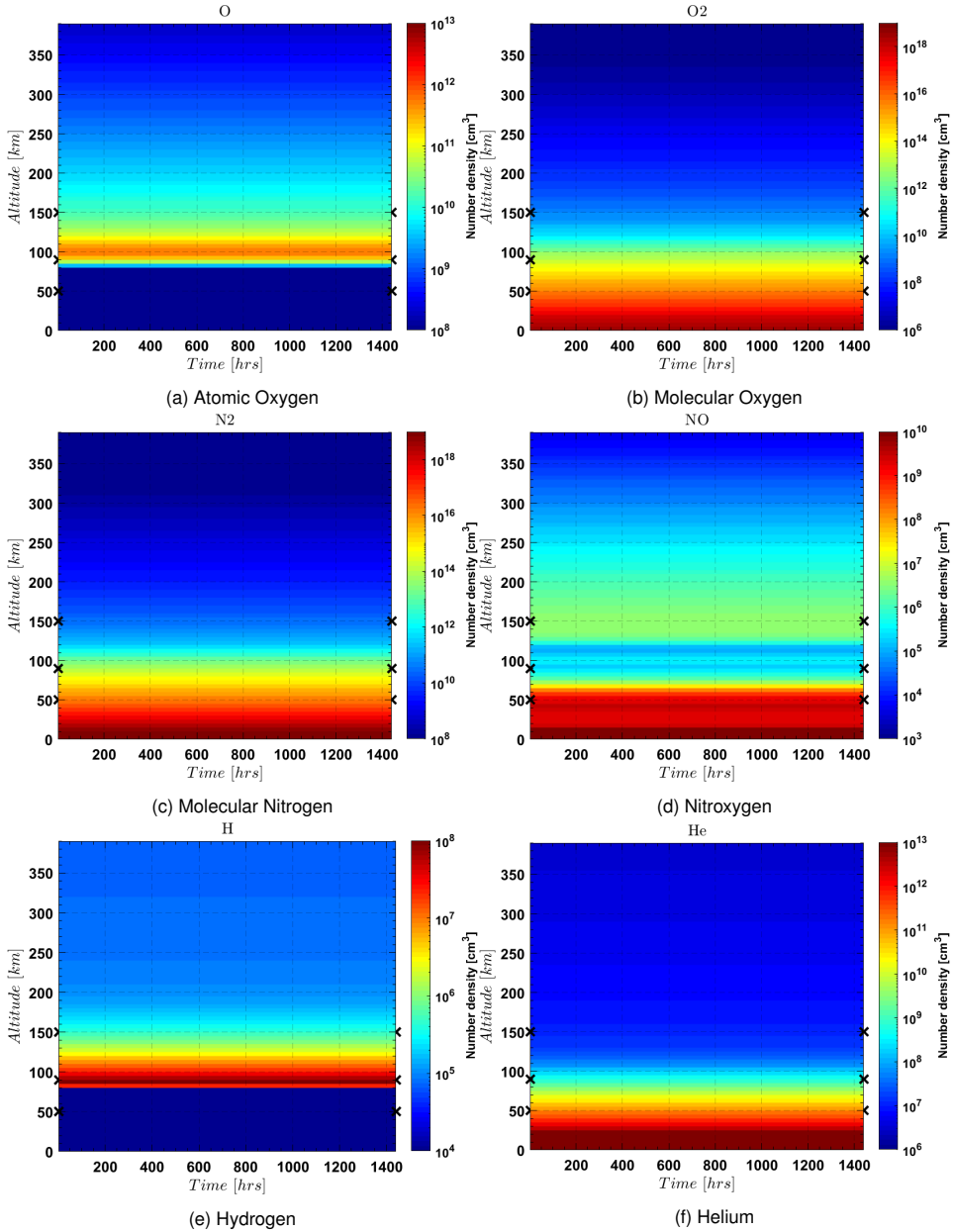


Figure 6.7: The figures show neutral atmospheric species. The arrows on the vertical axis indicate the start of the D-, E-, and F-layer.

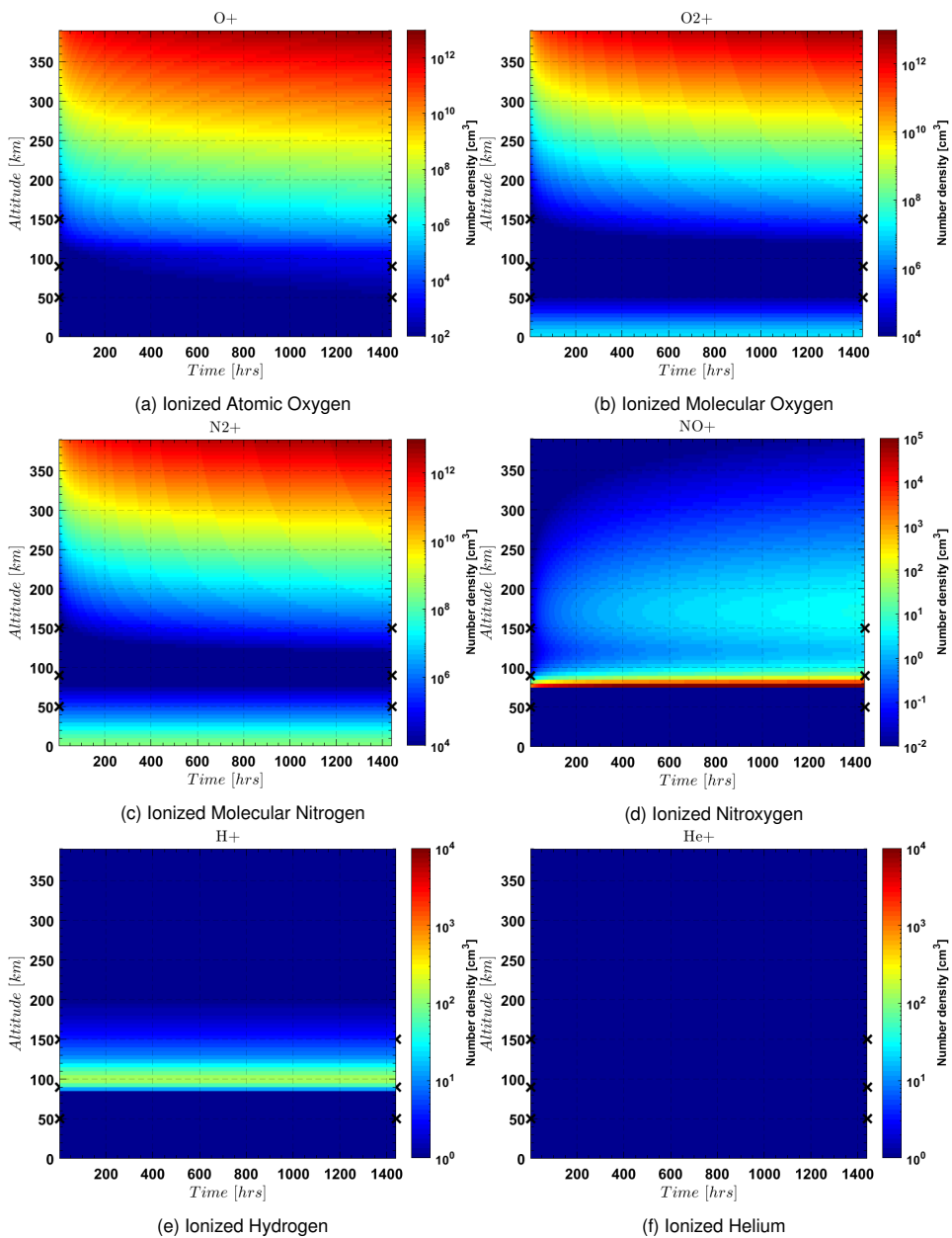


Figure 6.8: The figures show the ionized atmospheric species. The arrows on the vertical axis indicate the start of the D-, E-, and F-layer.

6.2 Measurement data in Mali

This section presents an analysis of scintillation measurements. These have been done by the Netherlands Armed Forces during their mission in Mali. In subsection 6.2 it is shown briefly how the scintillation measurements calculated. The expressions should be familiar, as these have been used before. How the data is logged and which details the data contains is shown in subsection 6.2. Section 6.2 presents results of scintillation, lock-time, Total Electron Content, and other figures.

Measurements

In Mali, measurements have been done with the Polarx5S Septentrio. This instrument is capable to measure Ionospheric scintillation on multiple frequencies for Global Navigation Satellite Systems (GNSS) (GNSS) satellites. The signal which it is able to derive from Global Positioning System (GPS) (GPS), GLONASS, GALILEAO, and COMPASS. With different frequency bands for the different satellites. The measurement instrument is able to measure *TEC* and scintillation (both phase and amplitude).

In the absence of scintillation, the signal is found to be expressed:

$$s(t) = Ad(t)c(t)\cos(f_1^2 t + \phi) + n(t) \quad (6.1)$$

Where the amplitude (A), signal data ($d(t)$), satellite code ($c(t)$), and the noise ($n(t)$) are used.[66] When scintillation is present, the fluctuations of amplitude (δA) and phase ($\delta\phi$) are used.

The scintillation index (S_4) of the amplitude is calculated as shown below and shown in [66].

$$S_4 = \sqrt{\frac{\langle I^2 \rangle - \langle I \rangle^2}{\langle I \rangle^2}} \quad (6.2)$$

Where $I = \delta A^2$ is the signal intensity. The brackets $\langle \rangle$ indicate an average over a specified time interval. In this case it is the average variation of the intensity of the signal.

Phase scintillation (σ_ϕ) is calculated with the standard deviation of ($\delta\phi$) over 60 s. The integral of Electron number density along satellite and receiver is *TEC*.

$$TEC = \int_{min}^{max} n_e ds_0 \quad (6.3)$$

$$\phi = \frac{q^2}{2C\epsilon m_e f (2\pi)^2} TEC \quad (6.4)$$

The equation for ϕ can be rewritten as $\phi = \frac{40.3}{Cf} TEC$. This expression has been used also in the Appleton-Hartree equation.

For dual frequency measurements it has been shown that *TEC* is calculated as.

$$TEC = \frac{1}{40.3} \left[\frac{f_2^2 f_1^2}{f_2^2 - f_1^2} \right] P_2 - P_1 \quad (6.5)$$

Where P_2 and P_1 are the group path length of the signals.[66]

Logging and data

The scintillation measurement data contains 62 columns. These columns represent the output of the Septentrio receiver. The output files are stored as Ionospheric Scintillation Monitoring Records (ISMR) (ISMR). An example of main measurements are, with their corresponding unit for each signal, the pseudorange (1 mm), carrier phase, Doppler 1×10^4 Hz, C/N0 (0.250 dB-Hz), and lock-time 1 s. The lock-time is the duration of the carrier phase. In table 6.1 blocks of output are shown. There are other blocks, as described in [76], but they are not of interest in this section.

Table 6.1: Table shows the most important format of the output blocks of the Sceptentrio receiver. Other blocks shows general information or are of less importance for this research.[76]

Block	Description
Measurement Blocks	Contains measurement and additional info such as observable variance, real and imaginary post-correlation values and measurement markers.
Navigation Pages	Contains navigation frame for the different satellites.
Decoded Messages	For each satellite used this block contains at least almanac data, Ionospheric data, and UTC data.
Position, Velocity and Time	This block contains the position, velocity and time in Cartesian and Geodetic coordinates.
INS/GNSS Integrated	This block contains integrated position and velocity in Cartesian and Geodetic coordinates.
GNSS Attitude	Contains details on the GNSS attitude.
Receiver Time	Contains the current receiver and UTC time.
L-band demodulator Status	Status of L-band signal tracking and service. Overall status of the receiver

In table 6.3 the satellite carrier frequencies are shown.

Table 6.3: Table shows the Carrier frequencies in *Mhz* of known satellites signals.[45, 76]

Satellite signal	Carrier Frequency [<i>Mhz</i>]
GPS L1	1575.42
GPS L2	1227.60
GPS L5	1176.45
GLO L1	deviates
GLO L2	1246.00
GAL L1	1575.42
GAL E5a (encoded)	1176.45
GAL E5b (encoded)	1207.14
GAL E5 (encoded)	1191.795
GEO L1CA	1575.42
Compass L1	1561.098
Compass E5b (encoded)	1207.14

Analysis of Mali measurements

The measurement data is saved in files of an hour. These hourly files contain 60 measurements of 24 satellite signals. Not all satellites are usable. The figures below contain GPS satellite signals and have a continuous lock-time. This makes the data usable for interpretation.

Figure 6.9 shows the amplitude scintillation (S4), lock-time, azimuth angle, elevation angle on the signal of GPS satellites. Figure 6.10 shows the code phase divergence and spectral slope of the GPS satellite signals. The code phase divergence is the difference (in meters) between the average pseudorange and carrier phase. Figure 6.12 shows the derived *TEC* from the GPS satellite signals.

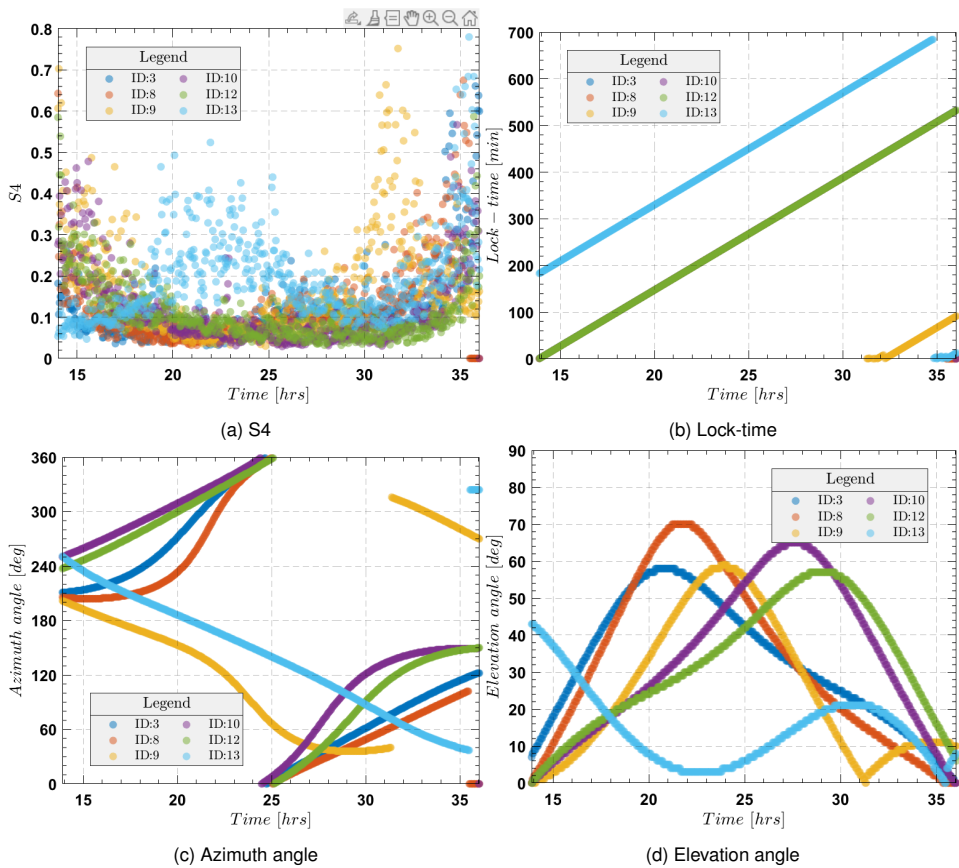


Figure 6.9: This figure shows data of GPS satellite signals. It contains the S4, lock-time, azimuth angle, and elevation angle. Measurements were done at week number 1877 and time of week 345660 seconds.

In Figure 6.9 the lock-time shows no loss of signal during the measurement. The elevation angle is shown for its relation to scintillation and time rate of change of *TEC*. The elevation angle is constant for the yellow and blue line, descending for green and orange, and ascending for cyan and purple. Lower elevation angles are related to higher S4 values, as can be seen for the orange, purple and blue lines, in

figure 1 and 4 of Figure 6.9. The same goes for higher elevation angles and a lower S4 value (green, yellow, and cyan lines in figure 1 and 4 of Figure 6.9). An added argument for concluding that low elevation angles account for high scintillation values can be seen in the orange line. The orange line reaches elevation angles below 15 to 20 degrees when scintillation values are going up at 2000 s. This effect is expected to be caused by multipath effect, where the satellite signal is reflected before it reaches the receiver.

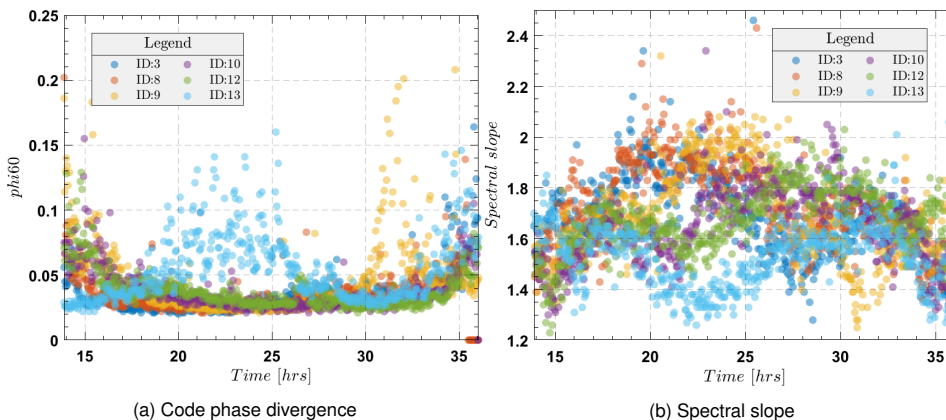


Figure 6.10: This figure shows data of GPS satellite signals. Measurements were done at week number 1877 and time of week 345660 seconds.

In Figure 6.10 also the low elevation angle lines are seen to cause a high phase divergence. The high elevation angles and constant elevation angles are found to have relative constant phase divergence. The reason the blue line has low phase divergence with a low elevation angle might be because the elevation angle is neither ascending or descending, but constant. The same goes for the yellow line.

In Figure 6.11 a Polar plot is shown of the azimuth angle and the elevation angle. The outer values are the azimuth angle, which has values between 0 and 360 deg. The elevation angle has a maximum of 90 deg.

The purple line can immediately be seen to have high *TEC* values in Figure 6.12. This is definitely because of the low elevation angle, as the satellite signal is expected to have travelled a longer pathway. The cyan line looks like to go downward in *TEC* values. This makes our argument on the purple line stronger, because the cyan has an ascending elevation angle.

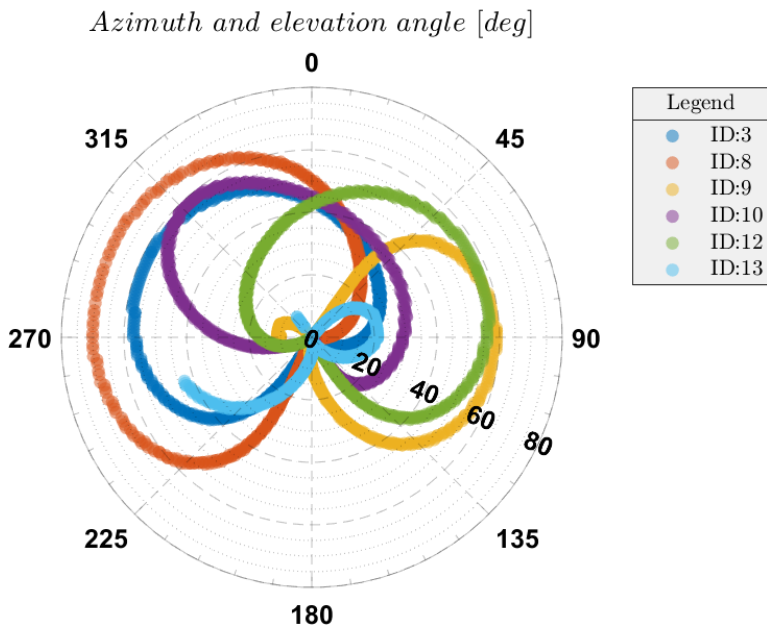


Figure 6.11: This figure shows a Polar plot of the azimuth and elevation angles of the GPS satellite signals. Measurements were done at week number 1877 and time of week 345660 seconds.

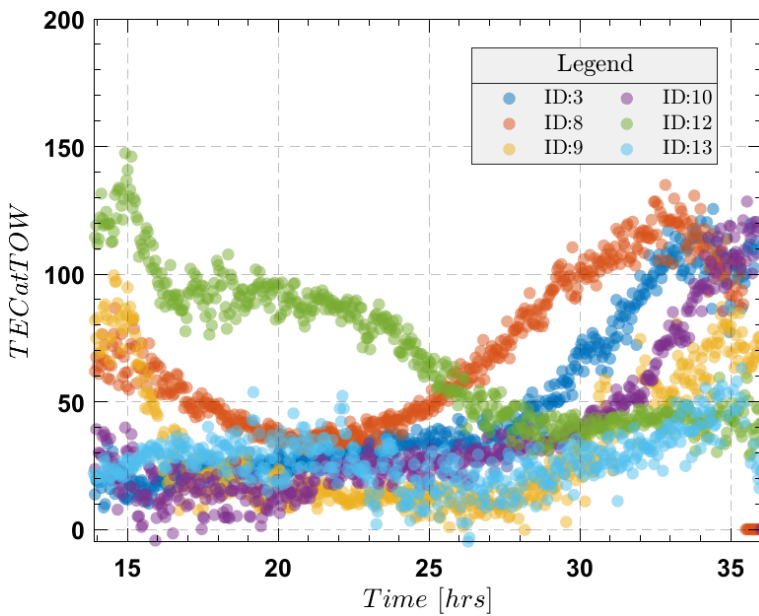


Figure 6.12: This figure shows TEC measurements of GPS satellite signals. Measurements were done at week number 1877 and time of week 345660 seconds.

6.3 Atmospheric effects on radio waves

The effect on radio waves by the atmosphere are covered in this section.

Troposphere

The main effects of the atmosphere on the propagating radio waves, as has been described in chapter 3, contains an lower atmospheric part, and an Ionospheric part. The path delay depends on atmospheric pressure and water vapour. The lower atmospheric absorption of radio waves can be calculated with the number density. shows the calculated absorption of radio waves, when assuming a receiver at a height of 300 km and the number density of O_2 and H. The absorption is found by calculating the effective path length of the radio wave, taking into account the scale height and atmospheric thickness.

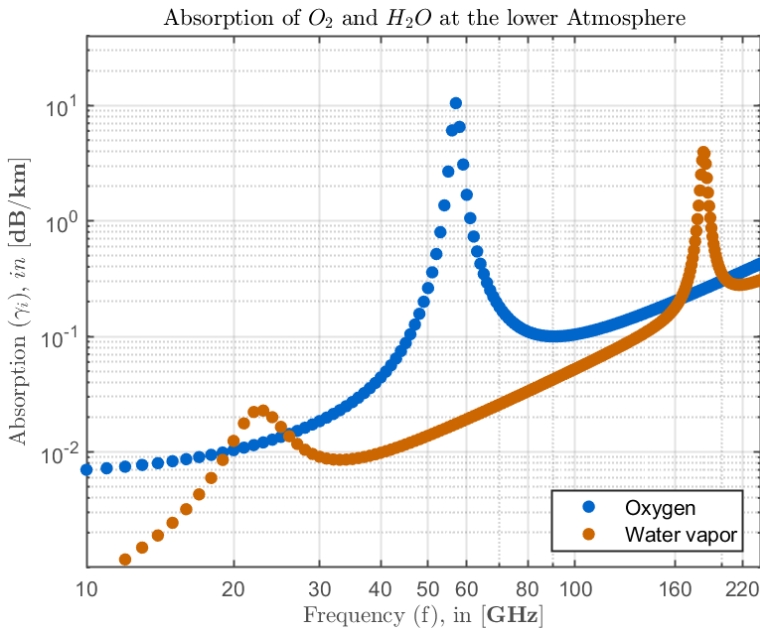


Figure 6.13: Figure showing the absorption of radio waves in the lower Thermosphere, as calculated from the Effective path length, and when only Oxygen and Water Vapor are taken into account.

A clear peak is shown at 60 GHz for O_2 , and second peaks at 20 and 200 GHz for Water vapor. Although the peaks are specific, the scale on which these occur is of minor importance, being at a absorption value on the order of 0.100 to almost 10.

Ionosphere

For the ionospheric part, the ionospheric D-, E-, and F-layer need to be found. Figure 6.14 shows modelled ionosphere, where it has been assumed that it consists of e^- and also of H^+ (for the D-layer), H^+ and O^+ (for the E-layer), and by H^+ , O^+ , O_2^+ , and N_2^+ (for the F1- and F2-layer). For this figure, the total Elec-

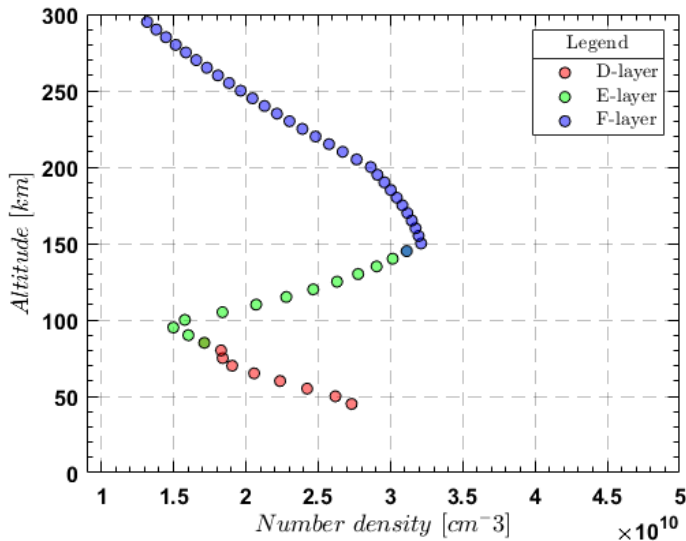


Figure 6.14: This figure shows the modelled ionospheric layers.

tron number density was found to be 1.2371 in *TEC* -units. This value is used to calculate the effect for that moment.

Figure 6.15 shows the modelled ionospheric layer. The D-layer covers the H^+ , NO^+ , and O_2^+ . The E-layer covers the same species as the D-layer, with an addition of N_2^+ and O^+ . The F-layer covers only the H^+ and O^+ .

In Figure 6.16 has been made with both modelled and measured data. The critical frequency is derived from the maximum modelled Electron number density of the E- and F-layer. The azimuth angle and elevation angle of a chosen satellite signal of the measurement data of Mali used to calculate a distance factor. This distance factor corrects for the height and angle the satellite signal is with respect to an observed location. To give a quick recap, the highest and lowest usable frequency which can be used, were introduced in chapter 3. The MUF is due to reflection of the radio wave in the E- and F-layer. The LUF is because a low Frequency in Hz might be absorbed by the lower Thermosphere. The ideal region is $> \text{Operational frequency} < .$ The MUF has two clear peaks with 12 hr between them, this must be diurnal behaviour. The sharp increase and decrease of the Frequency in Hz occurs within two hours.

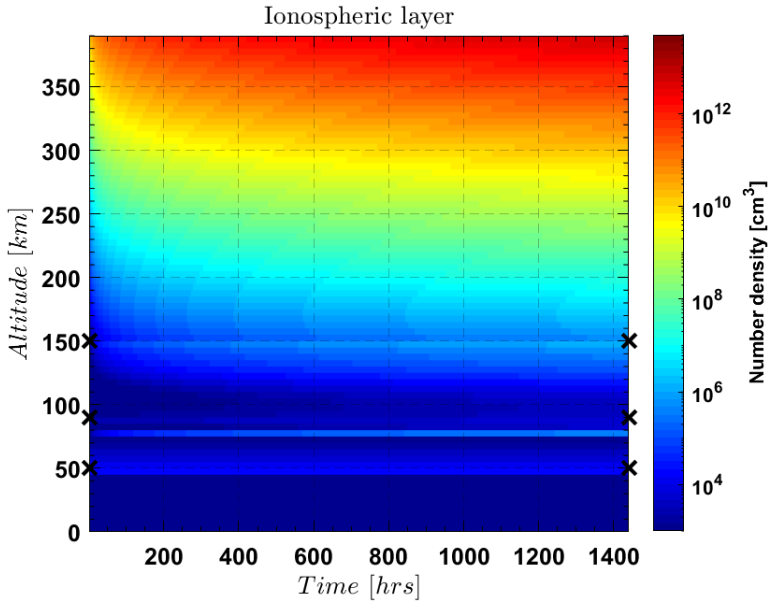


Figure 6.15: This figure shows the ionospheric layer. The arrows on the vertical axis indicate the start of the D-, E-, and F-layer.

Summary of this chapter

This chapter 6 has presented the results of the electron density model. In the next chapter, chapter 7 an outlook, recommendations, and conclusions are given.

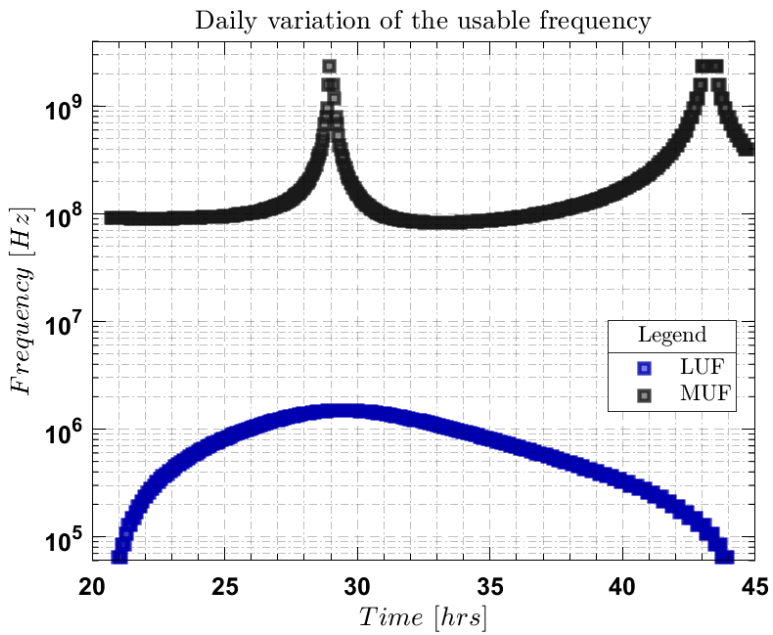


Figure 6.16: This figure shows the daily variation of the usable Frequency in Hz. The MUF and Lowest Usable Frequency (LUF) are shown in the figure. This figure has used the measured elevation and azimuth angle in Mali with the modelled absorption and Electron number density.

This page intentionally left blank.

7 Conclusions and recommendations

“In this chapter conclusions are shown from the work done and the results that have been found. Furthermore, a number of recommendations are mentioned for further research on this topic.”

Chapter objectives:

- Provide a reflection on the objectives
 - Provide an interpretation of the most important findings
 - Highlight the strengths and limitations of the model
 - Discuss unanswered questions and provide recommendations for future research
-

In this thesis we have introduced the neutral atmosphere in 2. This neutral atmosphere was the medium where radio waves were propagated through. Chapter 3 has shown how the propagated radio waves are being disturbed by mainly atmospheric Electron number density. The Space weather phenomena of chapter 4 are shown to be related to the change of Electron number density. We have modelled the electron density variations of the atmosphere in chapter 5. The main components needed to model were used. Real-time scintillation measurements were presented in chapter 6. These measurements have shown good accuracy and are usable in an electron density model. The main conclusions cover multiple research areas. A summary of findings is given in section 7.2 to cover these areas. Before this is shown a reflection on the objectives is given in section 7.1. Recommendations for future research will be given in section 7.3.

7.1 Reflecting on the objectives

The focus of this thesis is to investigate the atmospheric effect of Space Weather on Satellite communication. To properly investigate the effects, we first gained knowledge about the phenomena's of Space Weather and the underlying physics. Secondly, the effect of electron density on radio waves was investigated, and the variation of electron density on vertical and global scale. Third, an electron density model has been developed to investigate the possibility of using local measurements with this model.

7.2 Summary of findings

This section discusses and summarizes the highlights of this study.

Radio waves

The radio waves propagating through the atmosphere are effected by several components. An Tropospheric and Ionospheric component.

1. Absorption of the radio waves are found to be mainly due to Molecular Oxygen and water vapor in the Troposphere. This is a dry component and a wet component, depending on the water vapor density.
2. Molecular Oxygen results in the larger component of the disturbance. Water vapor however is more fluctuating.
3. The total delay due to the Troposphere was found to be in the order of centimetres.
4. The Ionospheric layers effecting radio waves are expressed by the Appleton-Hartree formula. This expression separates the components of the Ionosphere.

Space Weather

Space Weather was in early in our scope during this research. A literature study has covered space weather events and their effect. It was found that the Solar wind interacts with the Geomagnetic Field (\vec{B}), resulting in the phenomena described in section 4.1 and n_e variations. A summary of phenomena are shown below. It will be clear that these phenomena are resulting in a disturbance of the Ionosphere. And also on Ionospheric n_e .

1. During the literature study the main Space Weather phenomena that occur were thought to be Ionospheric storms, Solar radiation, Solar Flares, and Coronal Mass Ejections.
2. The Solar wind and Geomagnetic Field (\vec{B}) are found to interact more often in certain regions. These regions are the bow shock, magnetopause, and the magnetotail.
3. The magnetotail is contained by reconnection of the magnetopause. It contains two plasma sheets. These are characterized by an ion plasma sheet and an electron plasma sheet. A global instability is capable to result in Earthward convection. This convection directed towards the Earth then results in a downward ejected magnetized plasma.
4. So, in other words the previous item indicates that the IMF is capable of pushing the Ionospheric Geomagnetic Field (\vec{B}) downward and moving the electrojet towards the poles. This poleward transport of the auroral arcs and electrojet results in an accumulation at the poles. The explosive release of this accumulated matter is what we call a Magnetospheric or Ionospheric storm.
5. The ejection of plasma towards Earth is capable to emit a bright auroral display. This is the famous Polar light, also known as Aurora Polaris. Although the Aurora Borealis (North) might be more famous compared to its Southern component (Aurora Australis). This phenomena is actually an auroral substorm.
6. The interaction of IMF with the bow shock of the Magnetosphere of Earth is capable to generate fast and hot plasma. These are also known as HFA and high speed jets.
7. Since the travel time from the Sun to Earth is 8 minutes at light speed, solar flares are quite difficult to use in a forecast. However, the after effects of a solar flare, Ionospheric storms, can be taken into account. Especially since these storms are known to cause fadeouts.

Electron density model

The electron density model is capable showing an atmosphere, with number density of atmospheric species and temperature of the neutral atmospheric species, ions, and electrons. The Solar EUV component, where up-to-date Solar radio flux

index is used with general used cross sections, shows good results. The analysis of the atmospheric effect by dividing the atmosphere in a lower thermosphere and multiple ionospheric layers, seems like a good approach in finding the effects step-by-step. The results of the model agree with those found in literature, especially the initial setup and Solar EUV component. More research on the components used in the model are needed to fully investigate the effects.

The ionospheric effect has a first-order component, and a higher order term, and another term for bending. Fortunately, not all effects found in literature needed to be taken into account, for example a double receiver could compensate due to combination of signals, as described in chapter 3. Although this correction method is only applicable for GPS signals.

Each component of the model that has been realized, has the possibility for their own research. The Solar Radiation Spectrum, which we defined with the EUVAC model, has been compared with other Solar EU models. Similar material is available for the Chemical reactions, interactions terms, electrodynamics etc. The solution of a Single Ionospheric layer, on which the Slanted, or Vertical *TEC* is used to quantify ionospheric effects is an important outcome. This could be extended into an Ionospheric Multilayer Approximation.

Mali data

The analysis of scintillation measurements show that they are usable. The scintillation measurements show good accuracy to calculate scintillation. Although there are parameters which might disturb a satellite signal, a good start has been made. A recommendation of potential parameters is shown in below in section 7.3.

7.3 Recommendations for further research

This section lists potential for future research.

1. Improvement in Mathematical modelling The model, which was made in this research, was made for a relatively simple geometric model to quantify disturbed radio waves.
2. To improve the model, it might take a look at the variations in Ionospheric Electron Density.
3. There could be a way of categorizing and quantifying Space Weather to model the effect it has on Electron Density variation.
4. Validation of the model against others, for example [61]

Space weather phenomena can be described how they would assume to behave. When a stable electron density model is available, a certain phenomena should be possible to model as disturbance. This would lead to better understanding of the underlying physics of the space weather phenomena.

The phenomena are found in literature to have certain characterized frequencies. It is not clear to me yet if these frequencies are the result of a phenomena

that have taken place, or that this will cause a phenomena. It might be possible that a certain disturbance has the right frequency to accumulate and result in a growing instability like the KHI. Nevertheless, it should answer questions and will give new questions.

Appendices

A Chemical reactions

Appendix 5

Chemical ionic reactions in the thermosphere

Exothermic chemical and ionic reactions are grouped into sources and losses for individual ions and minor neutral species. Thus, each reaction is listed at least twice: for every source there are one or more sinks, and there may be more than one source for some species. (There are a few exceptions involving minor species.) The major neutral species, N_2 , O_2 and O , are end products, following the scheme of Figure 5.4.1. The chemical equations are listed with the excess kinetic energy of the reaction and the rate coefficient that is currently most widely accepted. Reaction rate coefficients are obtained, primarily, from laboratory measurements but a few are derived from atmospheric data and modelling and from theoretical work. Some are still controversial. The numerical values listed in Table A5.1 are derived from numerous references in the research literature and are applicable in the temperature range encountered in the thermosphere.

Table A5.1 *Chemical/ionic reactions in the thermosphere*

Reaction	Rate Coefficient ^a
Chemical production of N_2^+	
$O_2^+(^4\Pi) + N_2 \rightarrow N_2^+ + O_2 + 0.523 \text{ eV}$	$\gamma_6 = 2.5 \times 10^{-10}$
$O^+(^2D) + N_2 \rightarrow N_2^+ + O + 1.33 \text{ eV}$	$\gamma_3 = 8 \times 10^{-10}$
$O^+(^2P) + N_2 \rightarrow N_2^+ + O + 3.02 \text{ eV}$	$\gamma_9 = 4.8 \times 10^{-10}$
Chemical loss of N_2^+	
$N_2^+ + O_2 \rightarrow O_2^+ + N_2 + 3.53 \text{ eV}$	$\gamma_5 = 5 \times 10^{-11} (T_R/300)^{-0.8}$
$N_2^+ + O \rightarrow NO^+ + N(^2D) + 0.70 \text{ eV}$ $\quad \quad \quad \rightarrow NO^+ + N(^4S) + 3.08 \text{ eV}$	$\gamma_4 = 1.4 \times 10^{-10} (T_R/300)^{-0.44}$ $\alpha_2 = 1.8 \times 10^{-7} (T_e/300)^{-0.39}$
$N_2^+ + e \rightarrow N(^2D) + N(^2D) + 1.04 \text{ eV}$	$\gamma_{19} = 1.4 \times 10^{-10} (T_R/300)^{-0.44}$
$N_2^+ + O \rightarrow O^+(^4S) + N_2 + 1.96 \text{ eV}$	$\gamma_{18} = 3.3 \times 10^{-10}$
$N_2^+ + NO \rightarrow NO^+ + N_2 + 6.33 \text{ eV}$	
Chemical production of O_2^+	
$O^+(^4S) + O_2 \rightarrow O_2^+ + O + 1.55 \text{ eV}$	$\gamma_2 = 2 \times 10^{-11} (T_R/300)^{-0.4}$
$O^+(^2D) + O_2 \rightarrow O_2^+ + O + 4.865 \text{ eV}$	$\gamma_{22} = 7 \times 10^{-10}$
$N^+ + O_2 \rightarrow O_2^+ + N(^4S) + 2.486 \text{ eV}$	$\gamma_{11} = 1.1 \times 10^{-10}$
$N^+ + O_2 \rightarrow O_2^+ + N(^2D) + 0.1 \text{ eV}$	$\gamma_{33} = 2 \times 10^{-10}$
$N_2^+ + O_2 \rightarrow O_2^+ + N_2 + 3.53 \text{ eV}$	$\gamma_5 = 5 \times 10^{-11} (T_R/300)^{-0.8}$
$O_2^+(^4\Pi) + O \rightarrow O_2^+ + O + 4.05 \text{ eV}$	$\gamma_7 = 1 \times 10^{-10}$

B Photo ionization Cross sections

	Å	⁴ S	² D	² P	⁴ P	² P*	O ²⁺	Total	N ⁺	N ²⁺	Total
1	50-100	0.190	0.206	0.134	0.062	0.049	0.088	0.730	0.286	0.045	0.331
2	100-150	0.486	0.529	0.345	0.163	0.130	0.186	1.839	0.878	0.118	0.996
3	150-200	0.952	1.171	0.768	0.348	0.278	0.215	3.732	2.300	0.190	2.490
4	200-250	1.311	1.762	1.144	0.508	0.366	0.110	5.202	3.778	0.167	3.946
5	256.30	1.539	2.138	1.363	0.598	0.412	0.000	6.050	4.787	0.085	4.874
6	284.15	1.770	2.620	1.630	0.710	0.350	0.000	7.080	5.725	0.000	5.725
7	250-300	1.628	2.325	1.488	0.637	0.383	0.000	6.461	5.192	0.051	5.244
8	303.31	1.920	2.842	1.920	0.691	0.307	0.000	7.680	6.399	0.000	6.399
9	303.78	1.925	2.849	1.925	0.693	0.308	0.000	7.700	6.413	0.000	6.413
10	300-350	2.259	3.446	2.173	0.815	0.000	0.000	8.693	7.298	0.000	7.298
11	368.07	2.559	3.936	2.558	0.787	0.000	0.000	9.840	8.302	0.000	8.302
12	350-400	2.523	3.883	2.422	0.859	0.000	0.000	9.687	8.150	0.000	8.150
13	400-450	3.073	4.896	2.986	0.541	0.000	0.000	11.496	9.556	0.000	9.556
14	465.22	3.340	5.370	3.220	0.000	0.000	0.000	11.930	10.578	0.000	10.578
15	450-500	3.394	5.459	3.274	0.000	0.000	0.000	12.127	11.016	0.000	11.016
16	500-550	3.421	5.427	3.211	0.000	0.000	0.000	12.059	11.503	0.000	11.503
17	554.37	3.650	5.670	3.270	0.000	0.000	0.000	12.590	11.772	0.000	11.772
18	584.33	3.920	6.020	3.150	0.000	0.000	0.000	13.090	11.778	0.000	11.778
19	550-600	3.620	5.910	3.494	0.000	0.000	0.000	13.024	11.758	0.000	11.758
20	609.760	3.610	6.170	3.620	0.000	0.000	0.000	13.400	11.798	0.000	11.798
21	629.73	3.880	6.290	3.230	0.000	0.000	0.000	13.400	11.212	0.000	11.212
22	600-650	4.250	6.159	2.956	0.000	0.000	0.000	13.365	11.951	0.000	11.951
23	650-700	5.128	11.453	0.664	0.000	0.000	0.000	17.245	12.423	0.000	12.423
24	703.36	4.890	6.570	0.000	0.000	0.000	0.000	11.460	13.265	0.000	13.265
25	700-750	6.739	3.997	0.000	0.000	0.000	0.000	10.736	12.098	0.000	12.098
26	765.15	4.000	0.000	0.000	0.000	0.000	0.000	4.000	11.323	0.000	11.323
27	770.41	3.890	0.000	0.000	0.000	0.000	0.000	3.890	11.244	0.000	11.244
28	789.36	3.749	0.000	0.000	0.000	0.000	0.000	3.749	10.961	0.000	10.961
29	750-800	5.091	0.000	0.000	0.000	0.000	0.000	5.091	11.171	0.000	11.171
30	800-850	3.498	0.000	0.000	0.000	0.000	0.000	3.498	10.294	0.000	10.294
31	850-900	4.554	0.000	0.000	0.000	0.000	0.000	4.554	0.211	0.000	0.211
32	900-950	1.315	0.000	0.000	0.000	0.000	0.000	1.315	0.000	0.000	0.000

The modified F74113 EUV flux spectrum was used to weight the cross sections in the 50 Å bins. All the cross sections are zero for wavelengths above 950 Å. Photoionization cross sections are $\times 10^{18} \text{ cm}^2$

Figure B.1: Photo ionization Cross sections for Atomic Oxygen O_2 and Atomic Nitrogen N_2 . [12]

	Å	N _{2abs}	N ₂ ⁺	N ⁺	N _{2ion}	O _{2abs}	O ₂ ⁺	O ⁺	O _{2ion}
1	50-100	0.720	0.443	0.277	0.720	1.316	1.316	0.000	1.316
2	100-150	2.261	1.479	0.782	2.261	3.806	2.346	1.460	3.806
3	150-200	4.958	3.153	1.805	4.958	7.509	4.139	3.368	7.509
4	200-250	8.392	5.226	3.166	8.392	10.900	6.619	4.281	10.900
5	256.30	10.210	6.781	3.420	10.210	13.370	8.460	4.910	13.370
6	284.15	10.900	8.100	2.800	10.900	15.790	9.890	5.900	15.790
7	250-300	10.493	7.347	3.145	10.493	14.387	9.056	5.332	14.387
8	303.31	11.670	9.180	2.490	11.670	16.800	10.860	5.940	16.800
9	303.78	11.700	9.210	2.490	11.700	16.810	10.880	5.930	16.810
10	300-350	13.857	11.600	2.257	13.857	17.438	12.229	5.212	17.438
11	368.07	16.910	15.350	1.560	16.910	18.320	13.760	4.560	18.320
12	350-400	16.395	14.669	1.726	16.395	18.118	13.418	4.703	18.118
13	400-450	21.675	20.692	0.982	21.675	20.310	15.490	4.818	20.310
14	465.22	23.160	22.100	1.060	23.160	21.910	16.970	4.940	21.910
15	450-500	23.471	22.772	0.699	23.471	23.101	17.754	5.347	23.101
16	500-550	24.501	24.468	0.033	24.501	24.606	19.469	5.139	24.606
17	554.37	24.130	24.130	0.000	24.130	26.040	21.600	4.440	26.040
18	584.33	22.400	22.400	0.000	22.400	22.720	18.840	3.880	22.720
19	550-600	22.787	22.787	0.000	22.787	26.610	22.789	3.824	26.610
20	609.76	22.790	22.790	0.000	22.790	28.070	24.540	1.850	26.390
21	629.73	23.370	23.370	0.000	23.370	32.060	30.070	1.030	31.100
22	600-650	23.339	23.339	0.000	23.339	26.017	23.974	0.962	24.937
23	650-700	31.755	29.235	0.000	29.235	21.919	21.116	0.190	21.306
24	703.36	26.540	25.480	0.000	25.480	27.440	23.750	0.000	23.750
25	700-750	24.662	15.060	0.000	15.060	28.535	23.805	0.000	23.805
26	765.15	120.490	65.800	0.000	65.800	20.800	11.720	0.000	11.720
27	770.41	14.180	8.500	0.000	8.500	18.910	8.470	0.000	8.470
28	789.36	16.487	8.860	0.000	8.860	26.668	10.191	0.000	10.191
29	750-800	33.578	14.274	0.000	14.274	22.145	10.597	0.000	10.597
30	800-850	16.992	0.000	0.000	0.000	16.631	6.413	0.000	6.413
31	850-900	20.249	0.000	0.000	0.000	8.562	5.494	0.000	5.494
32	900-950	9.680	0.000	0.000	0.000	12.817	9.374	0.000	9.374
33	977.02	2.240	0.000	0.000	0.000	18.730	15.540	0.000	15.540
34	950-1000	50.988	0.000	0.000	0.000	21.108	13.940	0.000	13.940
35	1025.72	0.000	0.000	0.000	0.000	1.630	0.000	0.000	0.000
36	1031.91	0.000	0.000	0.000	0.000	0.000	0.000	0.000	0.000
37	1000-1050	0.000	0.000	0.000	0.000	1.346	0.259	0.000	0.259

The modified F74113 EUV flux spectrum was used to weight the cross sections in the 50 Å bins. Cross sections are $\times 10^{16} \text{ cm}^2$

Figure B.2: Photo ionization and absorption Cross sections for Oxygen O_2 and Nitrogen N_2 . [12]

B.1 Matlab output figures

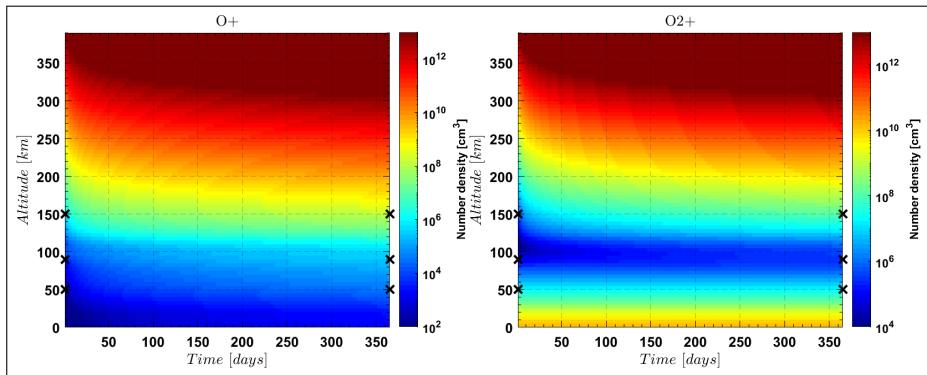


Figure B.3: This figure shows modelled atmospheric ionized Molecular Oxygen and Ionized Atomic Oxygen for 365 days. The time step taken is 86 400 s, which is one day. The arrows on the vertical axis indicate the start of the D-, E-, and F-layer.

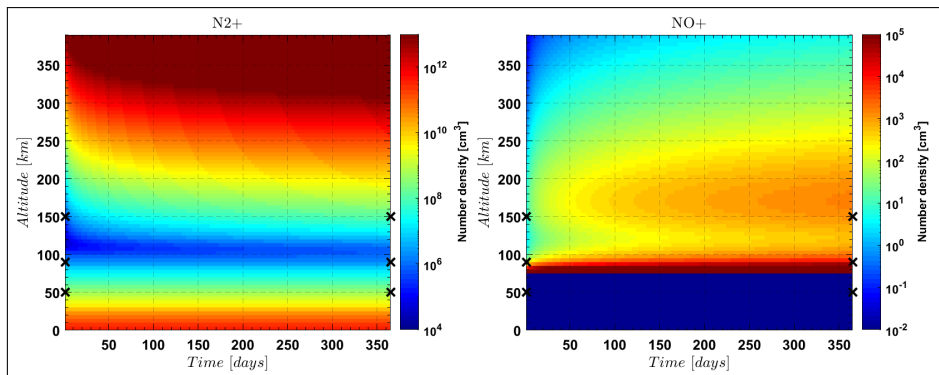


Figure B.4: This figure shows modelled atmospheric ionized Molecular Nitrogen and Ionized Nitroxygen for 365 days. The time step taken is 86 400 s which is one day. The arrows on the vertical axis indicate the start of the D-, E-, and F-layer.

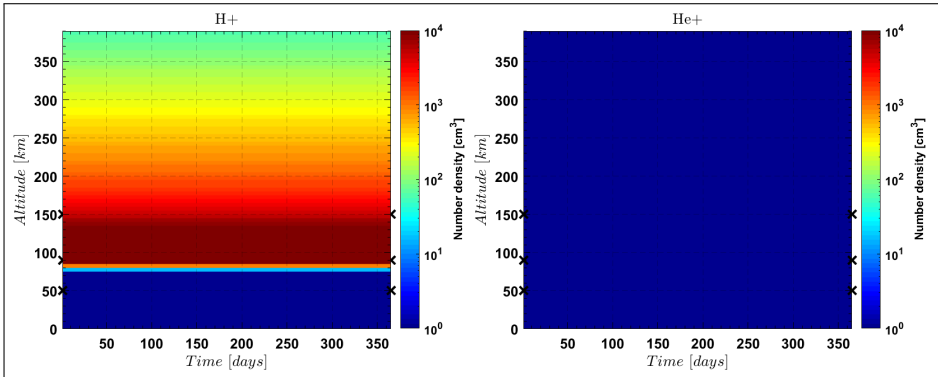


Figure B.5: This figure shows modelled atmospheric Ionized Hydrogen and Ionized Helium for 365 days. The time step taken is 86400 seconds, which is one day. The arrows on the vertical axis indicate the start of the D-, E-, and F-layer.

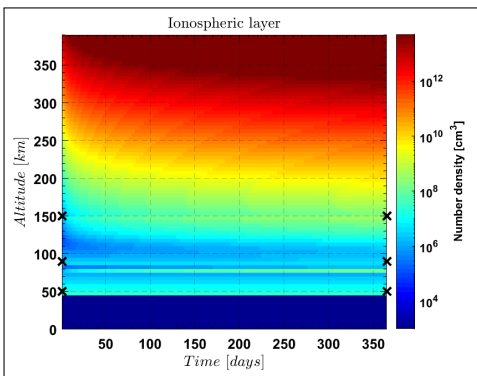


Figure B.6: This figure shows the Ionospheric layer for 365 days. The time step taken is 86400 seconds, which is one day. The arrows on the vertical axis indicate the start of the D-, E-, and F-layer.

C NOAA Scales



NOAA Space Weather Scales



Category		Effect	Physical measure	Average Frequency (1 cycle = 11 years)
Scale	Descriptor	Duration of event will influence severity of effects		
Geomagnetic Storms				
G 5	Extreme	Power systems: widespread voltage control problems and protective system problems can occur, some grid systems may experience complete collapse or blackouts. Transformers may experience damage. Spacecraft operations: may experience extensive surface charging, problems with orientation, uplink/downlink and tracking satellites. Other systems: pipeline currents can reach hundreds of amps, HF (high frequency) radio propagation may be impossible in many areas for one to two days, satellite navigation may be degraded for days, low-frequency radio navigation can be out for hours, and aurora has been seen as low as Florida and southern Texas (typically 40° geomagnetic lat.).**	Kp=9	Number of storm events when Kp level was met; (number of storm days) 4 per cycle (4 days per cycle)
		Power systems: possible widespread voltage control problems and some protective systems will mistakenly trip out key assets from the grid. Spacecraft operations: may experience surface charging and tracking problems, corrections may be needed for orientation problems. Other systems: induced pipeline currents affect preventive measures, HF radio propagation sporadic, satellite navigation degraded for hours, low-frequency radio navigation disrupted, and aurora has been seen as low as Alabama and northern California (typically 45° geomagnetic lat.).**	Kp=8	100 per cycle (60 days per cycle)
G 4	Severe	Power systems: voltage corrections may be required, false alarms triggered on some protection devices. Spacecraft operations: surface charging may occur on satellite components, drag may increase on low-Earth-orbit satellites, and corrections may be needed for orientation problems. Other systems: intermittent satellite navigation and low-frequency radio navigation problems may occur, HF radio may be intermittent, and aurora has been seen as low as Illinois and Oregon (typically 50° geomagnetic lat.).**	Kp=7	200 per cycle (130 days per cycle)
G 3	Strong	Power systems: high-latitude power systems may experience voltage alarms, long-duration storms may cause transformer damage. Spacecraft operations: corrective actions to orientation may be required by ground control; possible changes in drag affect orbit predictions. Other systems: HF radio propagation can fade at higher latitudes, and aurora has been seen as low as New York and Idaho (typically 55° geomagnetic lat.).**	Kp=6	600 per cycle (360 days per cycle)
G 2	Moderate	Power systems: weak power grid fluctuations can occur. Spacecraft operations: minor impact on satellite operations possible. Other systems: migratory animals are affected at this and higher levels; aurora is commonly visible at high latitudes (northern Michigan and Maine).**	Kp=5	1700 per cycle (900 days per cycle)
G 1	Minor			

* Based on this measure, but other physical measures are also considered.
 ** For specific locations around the globe, use geomagnetic latitude to determine likely sightings (see www.swpc.noaa.gov/Aurora)

Solar Radiation Storms		Flux level of ≥ 10 MeV particles (ions)*	Number of events when flux level was met**	
S 5	Extreme	Biological: unavoidable high radiation hazard to astronauts on EVA (extra-vehicular activity); passengers and crew in high-flying aircraft at high latitudes may be exposed to radiation risk.*** Satellite operations: satellites may be rendered useless, memory impacts can cause loss of control, may cause serious noise in image data, star-trackers may be unable to locate sources; permanent damage to solar panels possible. Other systems: complete blackout of HF (high frequency) communications possible through the polar regions, and position errors make navigation operations extremely difficult.	10 ⁷	Fewer than 1 per cycle
		Biological: unavoidable radiation hazard to astronauts on EVA; passengers and crew in high-flying aircraft at high latitudes may be exposed to radiation risk.*** Satellite operations: may experience memory device problems and noise on imaging systems; star-tracker problems may cause orientation problems, and solar panel efficiency can be degraded. Other systems: blackout of HF radio communications through the polar regions and increased navigation errors over several days are likely.	10 ⁶	3 per cycle
S 4	Severe	Biological: radiation hazard avoidance recommended for astronauts on EVA; passengers and crew in high-flying aircraft at high latitudes may be exposed to radiation risk.*** Satellite operations: single-event upsets, noise in imaging systems, and slight reduction of efficiency in solar panel are likely. Other systems: degraded HF radio propagation through the polar regions and navigation position errors likely.	10 ⁵	10 per cycle
S 3	Strong	Biological: passengers and crew in high-flying aircraft at high latitudes may be exposed to elevated radiation risk.*** Satellite operations: infrequent single-event upsets possible. Other systems: effects on HF propagation through the polar regions, and navigation at polar cap locations possibly affected.	10 ⁴	25 per cycle
S 2	Moderate	Biological: none. Satellite operations: none. Other systems: minor impacts on HF radio in the polar regions.	10	50 per cycle
S 1	Minor			

* Flux levels are 5 minute averages. Flux in particles·s⁻¹·ster⁻¹·cm⁻² Based on this measure, but other physical measures are also considered.
 ** These events can last more than one day.
 *** High energy particle (>100 MeV) are a better indicator of radiation risk to passenger and crews. Pregnant women are particularly susceptible.

Radio Blackouts		GOES X-ray peak brightness by class and by flux*	Number of events when flux level was met; (number of storm days)	
R 5	Extreme	HF Radio: Complete HF (high frequency**) radio blackout on the entire sunlit side of the Earth lasting for a number of hours. This results in no HF radio contact with mariners and en route aviators in this sector. Navigation: Low-frequency navigation signals used by maritime and general aviation systems experience outages on the sunlit side of the Earth for many hours, causing loss in positioning. Increased satellite navigation errors in positioning for several hours on the sunlit side of Earth, which may spread into the night side.	X20 (2x10 ⁻⁵)	Fewer than 1 per cycle
		HF Radio: HF radio communication blackout on most of the sunlit side of Earth for one to two hours. HF radio contact lost during this time. Navigation: Outages of low-frequency navigation signals cause increased error in positioning for one to two hours. Minor disruptions of satellite navigation possible on the sunlit side of Earth.	X10 (10 ⁻⁵)	8 per cycle (8 days per cycle)
R 4	Severe	HF Radio: Wide area blackout of HF radio communication, loss of radio contact for about an hour on sunlit side of Earth. Navigation: Low-frequency navigation signals degraded for about an hour.	X1 (10 ⁻⁴)	175 per cycle (140 days per cycle)
R 3	Strong	HF Radio: Limited blackout of HF radio communication on sunlit side of the Earth, loss of radio contact for tens of minutes. Navigation: Degradation of low-frequency navigation signals for tens of minutes.	M5 (5x10 ⁻⁵)	350 per cycle (300 days per cycle)
R 2	Moderate	HF Radio: Weak or minor degradation of HF radio communication on sunlit side of the Earth, occasional loss of radio contact. Navigation: Low-frequency navigation signals degraded for brief intervals.	M1 (10 ⁻⁵)	2000 per cycle (950 days per cycle)
R 1	Minor			

* Flux, measured in the 0.1-0.8 nm range, in W m⁻². Based on this measure, but other physical measures are also considered.
 ** Other frequencies may also be affected by these conditions.
 URL: www.swpc.noaa.gov/NOAA_scales

April 7, 2011

Figure C.1: The NOAA Space Weather Scales for Geomagnetic Storms, Solar Radiation Storms and Radio Blackouts.

Bibliography

G. Pieper. "Space Physics". In: *Physics Today* (1971), p. 50. ISSN: 19450699. DOI: 10.1063/1.3022931 (cit. on pp. 8–9, 30, 33, 35).

M. R. Torr and D. G. Torr. "Associative ionization of N(2D) and O". In: *Planet. Space Sci.* (1979), pp. 1233–1237. ISSN: 00320633. DOI: 10.1016/0032-0633(79)90102-8 (cit. on pp. 42, 44).

J. Aarons. "Global Morphology of Ionospheric Scintillations". In: *Proc. IEEE* (1982), pp. 360–378. ISSN: 15582256. DOI: 10.1109/PROC.1982.12314 (cit. on p. 32).

K. Budden. *The Propagation of Radio Waves: The Theory of Radio Waves of Low Power in the Ionosphere and Magnetosphere*. Cambridge University Press, 1985, p. 688. ISBN: 978-0521369527. DOI: 10.1017/CBO9780511564321. URL: www.cambridge.org/core/books/propagation-of-radio-waves/BD8F03DDFEC9E2D3AB (cit. on pp. 16, 18, 23).

K. Davies. *Wave Propagation: The Propagation of Radio Waves*. 1st ed. Melbourne, Sydney: Cambridge University Press, 1986, pp. 1448–1448. ISBN: 987-0-521-25461-2. DOI: 10.1126/science.232.4756.1448. URL: nvhrbiblio.nl/biblio/boek/Budden%20-%20The%20propagation%20of%20radio%20waves.pdf (cit. on pp. 7, 17–19, 23–24).

H. Aoki and H. Kamimura. "Jahn-Teller-effect mediated superconductivity in oxides". In: *Solid State Communications* (1987), pp. 665–669. ISSN: 00381098. DOI: 10.1016/0038-1098(87)90876-3 (cit. on p. 24).

J. A. Klobuchar. "Ionospheric Time-Delay Algorithm for Single-Frequency GPS Users". In: *IEEE* (1987), pp. 325–331. ISSN: 00189251. DOI: 10.1109/TAES.1987.310829 (cit. on pp. 5, 19, 22, 24).

C. E. Rasmussen, R. W. Schunk, and V. B. Wickwar. "A photochemical equilibrium model for ionospheric conductivity". In: *J. Geophys. Res.* (1988), p. 9831. ISSN: 0148-0227. DOI: 10.1029/ja093ia09p09831 (cit. on p. 11).

M. H. Rees. "Physics and chemistry of the upper atmosphere". In: *Phys. Chem. Up. Atmos.* (1989). Ed. by D. J. T. Houghton, D. M. J. Rycroft, and D. A. J. Dessler. ISSN: 00320633. DOI: 10.1016/0032-0633(90)90079-6. URL: www.cambridge.org/core/product/identifier/9780511573118/type/book (cit. on pp. 11–12, 14, 45, 76).

D. Bilitza. "International reference ionosphere (1990)". In: *Planet. Space Sci.* (1990), p. 72 (cit. on p. 48).

D. Bilitza. "International reference ionosphere (1990)". In: *Planet. Space Sci.* (1992), p. 544. ISSN: 00320633. DOI: 10.1016/0032-0633(92)90174-M (cit. on p. 48).

P. G. Richards, J. a. Fennelly, and D. G. Torr. "Atmosphere Explorer E satellite . This new model produces Its relative simplicity coupled with its ability to reproduce the 50-575 solar EUV". In: *J. Geophys. Res.* (1994), pp. 8981–8992 (cit. on pp. 44, 49, 77–78).

G. J. Bailey, N. Balan, and Y. Z. Su. "The Sheffield University plasmasphere ionosphere model - A review". In: *J. Atmos. Solar-Terrestrial Phys.* (1997), pp. 1541–1552. ISSN: 13646826. DOI: 10.1016/S1364-6826(96)00155-1 (cit. on pp. 45, 51).

Huba, J. D. and Joyce, G. and Fedder, J. A. "Sami2 is Another Model of the Ionosphere (SAM2): A new low-latitude ionosphere model". In: *J. Geophys. Res. Sp. Phys.* (2000), pp. 23035–23053. ISSN: 2156-2202. DOI: 10.1029/2000ja000035 (cit. on pp. 45, 48).

Huba, J. D. and Joyce, G. and Fedder, J. A. "The Formation of an Electron Hole in the Topside Equatorial Ionosphere". In: *Geophys. Res. Lett.* (2000), pp. 181–184. ISSN: 00948276. DOI: 10.1029/1999GL010735 (cit. on pp. 42, 48).

Y. Kim, K. Irikura, and M. Ali. "Electron-Impact Total Ionization Cross Sections of Molecular Ions". In: *Journal of Research of the National Institute of Standards and Technology* 105 (2000), p. 285. DOI: 10.6028/jres.105.032 (cit. on p. 44).

S. C. Solomon, S. M. Bailey, and T. N. Woods. "Effect of solar soft X-rays on the lower ionosphere". In: *Geophys. Res. Lett.* (2001), pp. 2149–2152. ISSN: 00948276. DOI: 10.1029/2001GL012866 (cit. on p. 46).

H. P. Warren, J. T. Mariska, and J. Lean. "A new model of solar EUV irradiance variability 1. Model formulation". In: *J. Geophys. Res. Sp. Phys.* (2001), pp. 15745–15757. ISSN: 21699402. DOI: 10.1029/2000ja000282 (cit. on p. 49).

H. Lundstedt, H. Gleisner, and P. Wintoft. *Operational forecasts of the geomagnetic Dst index*. 2002. DOI: 10.1029/2002gl016151. URL: www.esa-spaceweather.net/spweather/esa/initiatives/spweatherstudies/ALC/wp32203210.pdf (cit. on pp. 34–35).

D. Odijk. *Fast precise GPS positioning in the presence of ionospheric delays*. Universiteit Delft, 2002, p. 242. ISBN: 9061322782 (cit. on p. 22).

J. M. Picone, A. E. Hedin, D. P. Drob, and A. C. Aikin. "NRLMSISE-00 empirical model of the atmosphere: Statistical comparisons and scientific issues". In: *J. Geophys. Res. Sp. Phys.* (2002). ISSN: 21699402. DOI: 10.1029/2002JA009430 (cit. on p. 46).

S. Kedar, G. A. Hajj, B. D. Wilson, and M. B. Heflin. "The effect of the second order GPS ionospheric correction on receiver positions". In: *Geophys. Res. Lett.* (2003), pp. 1–4. ISSN: 00948276. DOI: 10.1029/2003GL017639 (cit. on p. 19).

- J. L. Lean, H. P. Warren, J. T. Mariska, and J. Bishop. "A new model of solar EUV irradiance variability 2. Comparisons with empirical models and observations and implications for space weather". In: *J. Geophys. Res. Sp. Phys.* (2003), pp. 1–19. ISSN: 21699402. DOI: 10.1029/2001JA009238 (cit. on p. 49).
- S. M. Stankov et al. "A new method for reconstruction of the vertical electron density distribution in the upper ionosphere and plasmasphere". In: *J. Geophys. Res. Sp. Phys.* (2003). ISSN: 21699402. DOI: 10.1029/2002JA009570 (cit. on p. 46).
- P. Wielgosz, D. Grejner-Brzezinska, and I. Kashani. "Regional Ionosphere Mapping with Kriging and Multiquadric Methods". In: *J. Glob. Position. Syst.* (2003), pp. 48–55. ISSN: 14463156. DOI: 10.5081/jgps.2.1.48 (cit. on pp. 22–23).
- P. Song. "Space weather". In: *Geophys. Monograph Series* (2004), pp. 157–185. DOI: 10.1142/9781860944574_0005 (cit. on pp. 4, 27–28).
- J. V. Eccles, R. D. Hunsucker, D. Rice, and J. J. Sojka. "Space weather effects on midlatitude HF propagation paths: Observations and a data-driven D region model". In: *Sp. Weather* (2005), n/a–n/a. DOI: 10.1029/2004sw000094 (cit. on p. 8).
- S. C. Solomon and L. Qian. "Solar extreme-ultraviolet irradiance for general circulation models". In: *J. Geophys. Res. Sp. Phys.* (2005), pp. 1–14. ISSN: 21699402. DOI: 10.1029/2005JA011160 (cit. on p. 46).
- G. Pelletier. *Introduction to magnetohydrodynamics*. Springer, 2007, pp. 77–101. ISBN: 3540680330. DOI: 10.1007/978-3-540-68035-2_4 (cit. on pp. 13–14).
- B. R. Bowman et al. "A new empirical thermospheric density model JB2008 using new solar and geomagnetic indices". In: *Astronomy. Spec. Conf. Exhibition AIAA/AAS*. February 2015 (2008) (cit. on pp. 43, 46).
- E.L. Afraimovich, E.I. Astafyeva, A.V. Oinats, Y.V. Yasukevich. "Global electron content: A new conception to track solar activity". In: *Ann. Geophys.* (2008), pp. 335–344. ISSN: 14320576. DOI: 10.5194/angeo-26-335-2008. URL: doi.org/10.5194/angeo-26-335-2008 (cit. on p. 20).
- E.L. Afraimovich, V.V. Demyanov, A.B. Ishin. "Powerful solar radio bursts as a global and free tool for testing satellite broadband radio systems, including GPS-GLONASS-GALILEO". In: *J. Atmos. Solar-Terrestrial Phys.* (2008), pp. 1985–1994. ISSN: 13646826. DOI: 10.1016/j.jastp.2008.09.008. URL: doi.org/10.1016/j.jastp.2008.09.008 (cit. on p. 20).
- E.L. Afraimovich, Y.V. Yasukevich. "Using GPS-GLONASS-GALILEO data and IRI modeling for ionospheric calibration of radio telescopes and radio interferometers". In: *J. Atmos. Solar-Terrestrial Phys.* (2008), pp. 1949–1962. ISSN: 13646826. DOI: 10.1016/j.jastp.2008.05.006. URL: doi.org/10.1016/j.jastp.2008.05.006 (cit. on p. 20).
- J. D. Huba. *Nrl Ionosphere Model Sami3 : Euv and Flare Results*. 2008 (cit. on p. 48).

- Huba, J. D. and Joyce, G. and Krall, J. "Three-dimensional equatorial spread F modeling". In: *Geophys. Res. Lett.* (2008), pp. 1–5. ISSN: 00948276. DOI: 10.1029/2008GL033509 (cit. on p. 48).
- A. Belehaki, I. Stanislawski, and J. Liliensten. "An overview of ionosphere-thermosphere models available for space weather purposes". In: *Sp. Sci.* (2009), pp. 271–313. ISSN: 00386308. DOI: 10.1007/s11214-009-9510-0 (cit. on pp. 8, 19, 26, 28, 30, 48–49).
- E.L. Afraimovich, Y.V. Yasukevich. "New field of application of the IRI modeling - Determination of ionosphere transfer characteristic for radio astronomical signals". In: *Adv. Sp. Res.* (2009), pp. 1652–1659. ISSN: 02731177. DOI: 10.1016/j.asr.2008.02.003. URL: dx.doi.org/10.1016/j.asr.2008.02.003 (cit. on p. 20).
- M. C. Kelley. *The Earth's Ionosphere Second Edition*. Springer, 2009, p. 576. ISBN: 9780120884254 (cit. on pp. 7–10, 12, 26).
- A. Martellucci and A. R. P. Cerdeira. "Review of tropospheric, ionospheric and multipath data and models for global navigation satellite systems". In: *Eur. Conf. Antennas Propagation, EuCAP 2009, Proc.* (2009), pp. 3697–3702 (cit. on pp. 18, 20, 32).
- P. G. Richards et al. "Measured and modeled ionospheric densities, temperatures, and winds during the international polar year". In: *J. Geophys. Res. Sp. Phys.* (2009), pp. 1–10. ISSN: 21699402. DOI: 10.1029/2009JA014625 (cit. on p. 45).
- S. M. Stankov and R. Warnant. "Ionospheric slab thickness - Analysis, modelling and monitoring". In: *Adv. Sp. Res.* (2009), pp. 1295–1303. ISSN: 02731177. DOI: 10.1016/j.asr.2009.07.010 (cit. on p. 46).
- J. R. Fernandez et al. "Feasibility of developing an ionospheric E-region electron density storm model using TIMED/SABER measurements". In: *Adv. Sp. Res.* (2010), pp. 1070–1077. ISSN: 02731177. DOI: 10.1016/j.asr.2010.06.008 (cit. on p. 35).
- M. A. Abdu. "Aeronomy of the Earth's Atmosphere and Ionosphere". In: *Springer* (2011). DOI: 10.1007/978-94-007-0326-1 (cit. on pp. 26, 45).
- E. J. Petrie, M. Hernandez-Pajares, P. Spalla, P. Moore, and M. A. King. "A Review of Higher Order Ionospheric Refraction Effects on Dual Frequency GPS". In: *Surv. Geophys.* (2011), pp. 197–253. ISSN: 01693298. DOI: 10.1007/s10712-010-9105-z (cit. on pp. 24, 48).
- Septentrio. *SBF Reference Guide, V1.15.1*. 2012 (cit. on p. 60).
- J. E. Borovsky, M. H. Denton, R. E. Denton, V. K. Jordanova, and J. Krall. "Estimating the effects of ionospheric plasma on solar wind/magnetosphere coupling via mass loading of dayside reconnection: Ion-plasma-sheet oxygen, plasmaspheric drainage plumes, and the plasma cloak". In: *J. Geophys. Res. Sp. Phys.* (2013), pp. 5695–5719. ISSN: 21699402. DOI: 10.1002/jgra.50527 (cit. on p. 37).
- B. Foster. *TIEGCM Documentation*. 2013 (cit. on p. 49).

- F. Sermi. "Digital processing of the echo received by an Over The Horizon (OTHR) Sky-Wave (SW) Radar System for Geo-referencing of radar footprint through the identification of Sea/Land transition". University of Florence, 2013, pp. 33–52 (cit. on p. 25).
- E. Vigren and M. Galand. "Predictions of ion production rates and ion number densities within the diamagnetic cavity of comet 67P/churyumov-gerasimenko at perihelion". In: *Astrophys. J.* (2013). ISSN: 15384357. DOI: 10.1088/0004-637X/772/1/33 (cit. on pp. 11–12).
- Huba, J. D. and Schunk, R. W. and Khazanov, G. V. "Modeling the Ionosphere-Thermosphere System". In: *Geophysical Monograph Series 201* (2014). Ed. by Kenneth R. Minschwaner, Chair; Gray E. Bebout, Kenneth H. Brink, Jiasong Fang, Ralf R. Haese, Yonggang Liu, W. Berry Lyons, Laurent Montes, Nancy N. Rabalais, Todd C. Rasmussen, A. Surjalal Sharma, David E. Siskind, Rigobert Tibi, and Peter E. van Keken, Members, pp. 1–340. DOI: 10.1002/9781118704417. URL: agupubs.onlinelibrary.wiley.com/doi/book/10.1002/9781118704417 (cit. on pp. 42, 44, 48).
- M. C. Kelley. *The earth's electric field: sources from sun to mud*. Elsevier, 2014. ISBN: 9780123978868 (cit. on p. 26).
- X. Yang, J. Li, and S. Zhang. "Ionospheric correction for spaceborne single-frequency GPS based on single layer model". In: *J. Earth Syst. Sci.* (2014), pp. 767–778. ISSN: 0973774X. DOI: 10.1007/s12040-014-0442-z (cit. on p. 5).
- D. P. Drob et al. "An update to the Horizontal Wind Model (HWM): The quiet time thermosphere". In: *Earth Sp. Sci.* (2015), pp. 301–319. ISSN: 23335084. DOI: 10.1002/2014EA000089 (cit. on p. 45).
- J. P. Eastwood, H. Hietala, G. Toth, T. D. Phan, and M. Fujimoto. "What Controls the Structure and Dynamics of Earth's Magnetosphere?" In: *Sp. Sci.* (2015), pp. 251–286. ISSN: 15729672. DOI: 10.1007/s11214-014-0050-x. URL: dx.doi.org/10.1007/s11214-014-0050-x (cit. on pp. 36–38).
- S. Priyadarshi. "A Review of Ionospheric Scintillation Models". In: *Surv. Geophys.* (2015), pp. 295–324. ISSN: 01693298. DOI: 10.1007/s10712-015-9319-1 (cit. on p. 32).
- F. Xiao et al. "Wave-driven butterfly distribution of Van Allen belt relativistic electrons". In: *Nat. Commun.* (2015), pp. 1–9. ISSN: 20411723. DOI: 10.1038/ncomms9590. URL: dx.doi.org/10.1038/ncomms9590 (cit. on p. 35).
- M. Q. Khairuzzaman. *Radio wave propagation*. Vol. 4. 1. 2016, pp. 64–75. ISBN: 3540407588 (cit. on p. 18).
- M. Hapgood. "Satellite navigation—Amazing technology but insidious risk: Why everyone needs to understand space weather". In: *Sp. Weather* (2017), pp. 545–548. ISSN: 15427390. DOI: 10.1002/2017SW001638 (cit. on p. 5).
- G. Navigation and S. Systems. "andbook of Global Navigation Satellite Systems". In: *Springer Handbooks* (2017). DOI: 10.1007/978-3-319-42928-1 (cit. on pp. 14, 17).

- S. C. Solomon. "Global modeling of thermospheric airglow in the far ultraviolet". In: *J. Geophys. Res. Sp. Phys.* (2017), pp. 7834–7848. ISSN: 21699402. DOI: 10.1002/2017JA024314 (cit. on p. 46).
- Y. C. Y.C. Lin. "Model simulations of ion and electron density profiles in ionospheric E and F regions". In: *J. Geophys. Res. Sp. Phys.* (2017), pp. 2505–2529. ISSN: 21699402. DOI: 10.1002/2016JA022855 (cit. on p. 71).
- J. E. Borovsky and J. A. Valdivia. *The Earth's Magnetosphere: A Systems Science Overview and Assessment*. 2018. DOI: 10.1007/s10712-018-9487-x. URL: doi.org/10.1007/s10712-018-9487-x (cit. on pp. 33–34).
- European Space Agency. *Abstract book - 52nd ESLAB Symposium*. 2018 (cit. on p. 1).
- Huba, J D and Maute, A and Crowley, G and Observatory, High Altitude and Crowley, G. "SAMI3 ICON: MODEL OF THE IONOSPHERE/PLASMA-SPHERE SYSTEM". In: *NASA* (2018), pp. 731–742. DOI: 10.1007/s11214-017-0415-z.SAMI3 (cit. on p. 48).
- H. A. Observatory. "TIEGCM V1.94 Model Description". In: *High Altitude Observatory National Center for Atmospheric Research, Boulder, CO TIEGCM* (2018) (cit. on p. 49).
- H. Magsi, A. Ahmed, and A. Hussain. "Real-Time monitoring and logging of ionospheric scintillation and total electron content". In: *6th Int. Conf. Aerosp. Sci. Eng. ICASE 2019* November (2019). DOI: 10.1109/ICASE48783.2019.9059198 (cit. on pp. 58–59).
- N. Nishitani, J. M. Ruohoniemi, M. Lester, and J. B. H. e. a. Baker. *Correction to: Review of the accomplishments of mid-latitude Super Dual Auroral Radar Network (SuperDARN) HF radars*. 2019. DOI: 10.1186/s40645-019-0300-3 (cit. on p. 28).
- A.E. Hedin. *Standard Atmosphere Model*. Ed. by C. C. M. C. (NASA Goddard Space Flight Center. NASA Goddard Space Flight Center, Community Coordinated Modeling Center (CCMC), 2020. URL: nssdc.gsfc.nasa.gov/space/model/models/msis.html (cit. on pp. 46, 51).
- Australian Bureau of Meteorology. *Australian Government, Bureau of Meteorology*. Ed. by Australian Government. 2020. URL: www.sws.bom.gov.au (visited on 2020) (cit. on pp. 24, 32).
- N. C. for Environmental Information. *International Geomagnetic Reference Fieldmodel*. 2020. URL: www.ngdc.noaa.gov/geomag/calculators/magcalc.shtml (cit. on p. 46).
- I. A. of Geomagnetism and Aeronomy. *13th International Geomagnetic Reference Field model*. 2020. URL: ngdc.noaa.gov/IAGA/vmod/igrf.html (cit. on p. 46).
- NASA. *Images of NASA Goddard Earth Observatory*. Ed. by N. G. S. F. Center. NASA Goddard Space Flight Center, Community Coordinated Modeling Center (CCMC), 2020. URL: earthobservatory.nasa.gov/ (cit. on p. 29).

NIST. *Database*. Ed. by P. M. L. NIST. 2020. URL: [https://physics.nist.gov/cgi-bin/ionization/ion_data.php?id=NI&ision=I&initial=\\$&total=Y](https://physics.nist.gov/cgi-bin/ionization/ion_data.php?id=NI&ision=I&initial=$&total=Y) (cit. on p. 44).

NIST. *Electron-Impact Cross Sections for Ionization and Excitation Database*. Ed. by P. M. L. NIST. 2020. DOI: 10.18434/T4KK5C. URL: dx.doi.org/10.18434/T4KK5C (cit. on p. 44).

NIST. *Physical MEasurement Laboratory of NITS*. 2020. URL: www.nist.gov/pml/electron-impact-cross-sections-ionization-and-excitation-database (cit. on p. 44).

S. Nv. *PolaRx5S*. 2020 (cit. on pp. 59–60).

M. Pietrella and M. Pezzopane. “Maximum usable frequency and skip distance maps over Italy”. In: *Adv. Sp. Res.* 66.2 (2020), pp. 243–258. ISSN: 18791948. DOI: 10.1016/j.asr.2020.03.040. URL: <https://doi.org/10.1016/j.asr.2020.03.040> (cit. on p. 19).

Sir Edward Victor Appleton. *Biograph*. 2020. URL: www.nobelprize.org/prizes/physics/1947/appleton/biographical/ (cit. on p. 19).

